DISSERTATION

THE PHYSIOLOGICAL FUNCTION AND PATHOLOGICAL SIGNIFICANCE OF TRANSIENT RECEPTOR POTENTIAL ANKYRIN 1 CHANNELS IN THE CEREBRAL ARTERY ENDOTHELIUM

Submitted by

Michelle Nicole Sullivan

Department of Biomedical Sciences

In partial fulfillment of the requirements

For the Degree of Doctor of Philosophy

Colorado State University

Fort Collins, Colorado

Spring 2015

Doctoral Committee:

Advisor: Scott Earley
Co-Advisor: Yumei Feng

Frank Dinenno
Ronald Tjalkens
Gregory Amberg

ABSTRACT

THE PHYSIOLOGICAL FUNCTION AND PATHOLOGICAL SIGNIFICANCE OF THE TRANSIENT RECEPTOR POTENTIAL ANKYRIN 1 CHANNELS IN THE CEREBRAL ARTERY ENDOTHELIUM

Endothelial cell Ca^{2+} dynamics have a significant influence on cerebrovascular tone. Several transient receptor potential (TRP) channels have been shown to mediate Ca^{2+} influx in the endothelium, including TRP vanilloid 4 (TRPV4), TRPV3, and TRP ankyrin 1 (TRPA1), which activates endothelium-dependent vasodilatory pathways. High resolution Ca^{2+} imaging techniques have allowed for the recording of unitary TRP channel Ca^{2+} influx events, called TRP sparklets, in endothelial cells where they have been found to underlie vascular function. The following studies first characterize the biophysical properties of TRPV4 and TRPA1 sparklets in endothelial cells. TRPA1 channels are present in the endothelium of cerebral arteries and absent from other vascular beds, suggesting a critical, yet previously unknown function for the channel in this tissue. Research here describes the physiological function of TRPA1 channels as sensors of oxidative membrane degradation in cerebral artery endothelial cells. Further, the involvement of TRPA1 channels in delaying the onset of hypertension-associated spontaneous hemorrhagic stroke is examined.

TABLE OF CONTENTS

CHAPTER 1

Introduction

The vascular endothelium is a thin monolayer of endothelial cells lining the lumen of all blood vessels that is critically important for angiogenesis, prevention of thrombogensis, regulation of permeability, and arterial tone control. Endothelial dysfunction is tightly associated with common cardiovascular diseases such as atherosclerosis, stroke, and hypertension, demonstrating the critical importance of this tissue for maintaining vascular health. Due to their unique anatomical location, endothelial cells are able to directly detect blood-borne molecules and luminal shear stress. Endothelial cells convey these hemodynamic signals to underlying smooth muscle cells, thereby eliciting vasomotor responses. For example, increases in arterial shear stress stimulate production of nitric oxide (NO) by the endothelium, which diffuses to underlying smooth muscle cells to evoke vasodilation (*2, 3*). Endothelial cell-mediated vasoregulatory pathways are highly dependent on changes in intracellular [Ca^{2+}], establishing an essential function for endothelial cell Ca^{2+} entry in the regulation of vascular tone. However, little is known about the molecular identities and regulation of the specific Ca^{2+} influx channels involved. Electrophysiological methods are frequently used to record Ca^{2+}-permeable ion channel activity, but small, flat, native endothelial cells are difficult to study using this technique. Recently, alternative approaches utilizing fluorescence microscopy to record Ca^{2+} channel activity have been described (*4*). Cells containing sensitive, rapid Ca^{2+} indicators are imaged using total internal reflection fluorescence (TIRF) or high-speed confocal microscopy. Using these

methods, Ca^{2+} channel activity can be optically recorded as transient increases in fluorescence at the cell surface, and signal amplitude, spatial spread, and duration are determined.

Exciting studies have recently used these optical techniques to record transient receptor potential (TRP) channel activity in endothelial cells. 26 of the 28 members of the TRP superfamily of ion channels are permeable to Ca^{2+}, and many are present in the vascular endothelium (Table 1.1). Several TRP channels are known to be involved in endothelial cell Ca^{2+} influx and regulation of vascular tone (Table 1.1) (*5-8*). Using optical recording methods, Ca^{2+} influx events through unitary TRPV4 channels, termed "TRPV4 sparklets," were recently described in vascular endothelial cells (*1, 9*). More interestingly, analysis of TRPV4 sparklets in the intact endothelium indicated that a small number of sparklets can evoke a near-maximal endothelium-dependent vasodilation in pressurized arteries (*9*). These pioneering studies indicate the essential role of unitary TRP channel Ca^{2+} microdomains in vascular function. This review discusses the role of TRP channels in endothelium-dependent dilation, methods for recording TRP channel sparklets in endothelial cells, and the significance of TRPV4 sparklets in the regulation of vascular tone.

CHANGES IN INTRACELLULAR [CA^{2+}] REGULATE VASCULAR TONE

Intracellular [Ca^{2+}] is a critical determinate of vascular tone. Ca^{2+} signals can be global (i.e., continuous throughout the cytosol) and long lasting or can be spatially restricted to specific subcellular domains for brief periods of time. In arterial smooth

muscle cells, membrane depolarization causes Ca^{2+} influx through voltage-dependent Ca^{2+} channels, resulting in elevated global cytosolic [Ca^{2+}] and subsequent contraction. Endothelium-dependent relaxation of smooth muscle is also regulated by elevations in endothelial cell [Ca^{2+}]. Three major pathways for endothelium-dependent vasodilation are widely recognized: 1) Production of NO by endothelial nitric oxide synthase (eNOS), 2) production of prostacyclin (PGI2) by cyclooxygenase (COX), and 3) Endothelium-Derived Hyperpolarizing Factor (EDHF) (*10*) or Endothelium-Dependent Hyperpolarization (EDH) (*11, 12*) which are defined as endothelium-dependent vasodilatory mechanisms that persist when NO and PGI_2 synthesis are inhibited. The EDHF hypothesis follows the convention of the NO and PGI_2 pathways and proposes that of one or more additional endothelium-derived diffusible factor(s), such as epoxyeicosatrienoic acids (EETs),(*13*) potassium ions (K^+) (*14*), C-type natriuretic peptide (CNP) (*15, 16*), hydrogen sulfide (H_2S) (*17, 18*), and/or hydrogen peroxide (H_2O_2) (*19*), are responsible for smooth muscle cell hyperpolarization and subsequent vasodilation. In contrast, EDH is a “factor-less” form of EDHF that is the result of endothelial cell plasma membrane hyperpolarization due to the efflux of K^+ from small- and intermediate-conductance Ca^{2+}-activated K^+ channels ($K_{Ca}2.3$ and $K_{Ca}3.1$, respectively) (*20, 21*). Endothelial cell membrane hyperpolarization rapidly spreads to underlying smooth muscle cells via myoendothelial gap junctions, directly hyperpolarizing and relaxing arterial myocytes (*10, 22*). EDH responses may be augmented by inwardly rectifying K^+ (K_{IR}) channels, which conduct greater outward K^+ currents at hyperpolarized membrane potential and amplify the original hyperpolarizing stimulus (*6, 23*). These seemingly divergent pathways can all be activated by increases

in endothelial cell [Ca^{2+}]: Production of NO by eNOS is elevated by binding to Ca^{2+}-calmodulin (*24*), whereas liberation of arachidonic acid by Ca^{2+}-sensitive phospholipase A2 (PLA2) (*25*) provides substrate for the biosynthesis of PGI_2(*25, 26*) and EETs (*13*). Increases in endothelial cell [Ca^{2+}] directly activate K_{Ca} channels to initiate EDH (*11, 12*).

Recent studies highlight the importance of myoendothelial junctions (MEJs) in EDH (*6, 8, 9, 27, 28*). MEJs are extensions of the endothelial cell plasma membrane that project through holes in the internal elastic lamina (IEL) and terminate proximal to the smooth muscle cell sarcolemma (*29, 30*). MEJs terminate in myoendothelial gap junctions allowing for acute endothelial cell-smooth muscle cell communication (*30*). Not all membrane projections within IEL holes contain myoendothelial gap junctions (*31*), but the significance of these structures (called myoendothelial close contacts) is not currently known. Expression of components of the EDH pathway, including K_{Ca} channels, inositol 1,4,5-trisphophate receptors (IP_3R), gap junctions, and TRP channels, is enriched in authentic MEJs (*5, 6, 27, 30, 32, 33*). Further, MEJs appear to be sites of dynamic localized Ca^{2+} signaling events that mediate EDH (*27, 28*).

Although the endothelium-dependent vasorelaxant pathways discussed above are functionally distinct, all can be initiated by an increase in endothelial cell intracellular [Ca^{2+}]. Such increases can be accomplished by Ca^{2+} entry from the extracellular space, but our understanding of the Ca^{2+}-permeable channels directly involved in endothelium-dependent vasodilation remains incomplete. Several classes of Ca^{2+} influx channels are reportedly present in the vascular endothelium including the cyclic nucleotide-gated channel A1 (CNGA1) (*34, 35*), the purinergic ligand-gated channel P2X4 (*36*), and TRP

channels (*5, 6, 37-39*). Ca^{2+} and Na^{+} influx through CNG channels present in endothelial cells occurs in response to store-operated Ca^{2+} entry (*34, 35*). P2X4 channels are activated by extracellular ATP and conduct Ca^{2+} into endothelial cells to cause vasodilation through increased NO synthesis (*34, 35, 40*). Although CNG and P2X4 may be involved in endothelium-dependent regulation under certain conditions, there is no apparent mechanism for these channels to respond to the multitude of stimuli presented to the intact endothelium. In contrast, Ca^{2+}-permeable members of the TRP superfamily are sensitive to physical factors (mechanical force (*41*), changes in osmolality (*42*)), temperature (*43-47*), hypoxia/hyperoxia (*48-50*), and chemical substances (*43, 51, 52*). A number of recent studies demonstrate the importance of particular TRP channels in endothelium-dependent vasodilatory responses.

TRP CHANNELS IN ENDOTHELIUM-DEPENDENT VASODILATION

All members of the TRP superfamily, with the exception TRPM4 and TRPM5, are permeable to Ca^{2+} (Table 1.1). Expression of at least 20 Ca^{2+}-permeable TRP channels has been detected in cultured and native endothelial cells, including TRPA1 (*6*), TRPC1 (*37, 53*), TRPC3 (*37, 53*), TRPC4 (*38, 53*), TRPC5 (*53*), TRPC6 (*53*), TRPV3 (*5*), and TRPV4 (*54*) (Table 1.1). Freichel et al., who investigated the role of TRPC4 in store-operated Ca^{2+} entry in endothelial cells, reported the first functional evidence of the involvement of a TRP channel in endothelium-dependent vasodilation (*38*). This study demonstrates that endothelial cells isolated from TRPC4 knockout ($TRPC4^{-/-}$) mice did not display a store-operated Ca^{2+} entry current. More interestingly, endothelial cells

isolated from TRPC4$^{-/-}$ mice exhibited reduced agonist-induced endothelial cell Ca^{2+} entry, and aortic ring sections displayed diminished endothelium-dependent vasorelaxation in response to acetylcholine, suggesting that TRPC4 channels are vitally important for endothelial cell function (*38*). Subsequent studies indicate that TRPV4, TRPC3, TRPV3, and TRPA1 channels are also critically involved in endothelium-dependent vasodilation (Table 1.1) (*5-8*).

The contribution of TRPV4 channels to endothelium-dependent vasodilation is well described. In heterologous expression systems and endothelial cells, TRPV4 channels are activated by EETs (*55*), potent vasodilators produced by endothelial cells synthesized from arachidonic acid by cytochrome P450 (CYP) epoxygenase enzymes (*56, 57*). EETs-induced vasodilation of isolated mesenteric arteries was absent from TRPV4$^{-/-}$ mice, suggesting that the channel is involved in this response (*6*). The physiological significance of this pathway was reported by Zhang and colleagues, who showed that TRPV4-mediated Ca^{2+} influx is critically important for flow-mediated dilation of human coronary arteries (*58*). Later studies demonstrate a similar role for TRPV4 in other vascular beds (*59, 60*). These studies imply that endothelial cell TRPV4 channels are activated by shear stress (*42*). However, although TRPV4 channels are activated by cell swelling, the channel is reportedly not inherently mechanosensitive (*61*). Further studies by Fleming and colleagues suggest that TRPV4 is indirectly activated by shear stress through flow-mediated production of arachidonic acid metabolites (*60*). Inhibition of CYP epoxygenase with MS-PPOH or block of TRPV4 with ruthenium red attenuated flow-induced dilation in mouse carotid arteries (*60*). However, TRPV4 blockade had no effect on flow-induced dilatory responses when CYP epoxygenase was downregulated

(*60*). These results are supported by another study showing that flow-induced dilation was impaired by PLA2 inhibition, TRPV4 inhibition by ruthenium red, and by TRPV4 knockout (*59*), suggesting that flow-induced dilation involves both TRPV4 and CYP epoxygenase activity. Further work by Gutterman and colleagues indicates that Ca^{2+} influx and vasodilation following stimulation with cholinergic agonists in some, but not all vessels, is markedly reduced in TRPV4$^{-/-}$ mice, clearly indicating a role for the channel in this response (*62-64*). Oddly, although the studies cited above and others suggest a critical role for TRPV4 in vascular regulation, global TRPV4$^{-/-}$ mice have no obvious cardiovascular phenotype, other than slightly enhanced sensitivity to hypertensive stimuli (*41*). Further studies using tissue-specific and/or inducible knockout mice are warranted to resolve this apparent paradox.

Reports from several laboratories suggest involvement of TRPC3 in endothelium-mediated vascular responses. Gao, et al. provided evidence for expression of TRPC3 in the endothelial and smooth muscle layers of human internal mammary artery (IMA) and show that the TRPC3 blocker Pyr3 modestly diminished relaxation of pre-contracted IMA rings (*65*). Using knockout models, Kochukov, et al. demonstrated that TRPC1 and TRPC3 channels are involved in Ca^{2+} influx and vasorelaxation of aortic ring segments (*66*). The Sandow laboratory recently reported participation of TRPC3 channels in EDH of rat and mouse mesenteric arteries (*8*). This study demonstrates that TRPC3 channels are present in the mesenteric endothelium and that ~70% of endothelial TRPC3 channels are localized within holes in the IEL. In the presence of the NOS inhibitor L-NAME, the guanylyl cyclase inhibitor ODQ, and the cyclooxygenase (COX) inhibitor indomethacin, Pyr3 blunted acetylcholine-induced vasorelaxation and

endothelial cell hyperpolarization. Vasodilatory responses were further attenuated by blocking K_{Ca} channels with TRAM34 and apamin. Together, these data suggest that TRPC3 channel activity can stimulate EDH in mesenteric arteries. In support of these findings, Kirby et al. reported the presence of TRPC3 as well as $K_{Ca}3.1$ and $K_{Ca}2.3$ within IEL fenestrations of rat popliteal and 1st order skeletal muscle arteries from the gastrocnemius muscle, suggesting that TRPC3 may contribute to EDH in this arterial bed as well (*33*), although this has not yet been directly demonstrated.

Our laboratory reported that TRPA1- and TRPV3-mediated Ca^{2+} influx provokes endothelium-dependent dilation of cerebral arteries (*5, 6*). TRPV3 channels are activated by the dietary molecule carvacrol, a substance derived from oregano (*5*). We found that carvacrol activates ruthenium red-sensitive cation currents and elevates intracellular Ca^{2+} levels in native cerebral artery endothelial cells (*5*). Carvacrol administration evoked endothelium-dependent vasodilation of cerebral arteries that was not altered by NOS and COX inhibition but was sensitive to block of K_{Ca} and K_{IR} channels (*5*). TRPA1 channels are activated by a variety of electrophilic substances, including allicin, found in garlic, and allyl isothiocyanate (AITC), derived from mustard oil (*51*). Allicin can dilate mesenteric arteries by activating TRPA1 channels in perivascular nerves and causing the release of calcitonin gene-related peptide (CGRP) (*67*). We found that TRPA1 channels were also present in the cerebral artery endothelium (*6*). AITC caused robust endothelium-dependent dilation and smooth muscle cell membrane hyperpolarization that was blocked by the selective TRPA1 inhibitor HC-030031. These responses were insensitive to NOS and COX blockade but were diminished by inhibition of K_{Ca} channels with TRAM34 and apamin, as well as block of K_{IR} channels with $BaCl_2$

(*6*). We also found that that TRPA1 channels are highly concentrated within IEL fenestrations in cerebral arteries and co-localize with $K_{Ca}3.1$ channels in this tissue (*6*). In contrast, TRPV3 channels are uniformly distributed (*5*), suggesting that TRPA1 and TRPV3 channels may elicit vasodilation by distinct molecular pathways. Insight into TRPA1-mediated endothelium-dependent vasodilation was provided by a recent study by Qian et al. demonstrating that activation of TRPA1 channels provokes dilation by recruiting large dynamic Ca^{2+} signals in the cerebral artery endothelium (*28*). Because food-borne molecules found in garlic and mustard can activate TRPV3 and TRPA1 channels, it is tempting to speculate that increased TRPV3 and/or TRPA1 activity in the endothelium could contribute to the putative cardioprotective benefits of certain dietary choices, but there is little direct evidence to support this idea. Further investigation into endogenous regulators of these channels is warranted.

OPTICAL METHODS FOR THE STUDY OF CA^{2+} INFLUX CHANNELS

Evidence cited above indicates that TRP channel activity can influence endothelium-dependent dilation, stimulating interest in the properties and regulation of TRP channels in the endothelium. Ion channels are traditionally studied using patch clamp electrophysiology. However, small, flat cells, such as native endothelial cells, are difficult to patch successfully, and throughput using conventional methods can be painfully slow. Moreover, inherent limitations of the voltage-clamp technique can impede investigation of ion channel regulation in a physiological setting. For example, when the conventional whole-cell patch clamp configuration is employed, intracellular

signaling pathways are disrupted when cells are dialyzed with the patch pipette solution. More serious disturbances in metabotropic regulatory mechanisms result from the application of inside-out or outside-out patch clamp methods. Although the intracellular environment is not disturbed when the on-cell patch clamp configuration is employed, channel activity can only be recorded from the small area of membrane beneath the recording pipette, and voltage clamp cannot be maintained. These technical issues hamper electrophysiological investigation of Ca^{2+} influx pathways in native endothelial cells.

Fortunately, sophisticated imaging techniques have recently been developed to surmount the limitations of both patch clamp electrophysiology and global Ca^{2+} imaging techniques. This methodology, pioneered by Parker and colleagues, uses high speed, high-resolution confocal microscopy or total internal reflection fluorescence (TIRF) microscopy to record single channel Ca^{2+} signals in a variety of cell types (*68, 69*). Confocal and TIRF microscopy use different approaches to achieve fluorescent excitation of a thin, isolated plane along the z-axis of a specimen (axial sectioning). High-resolution confocal microscopy employs an adjustable plane of illumination along the z-axis of a cell or tissue. This is achieved by scanning the specimen with a column of light so that only a small spot in the plane of focus is illuminated at a time. Due to light scattering, areas in out-of-focus planes are also illuminated with this setup alone. Therefore, the addition of a pinhole aperture proximal to the detector and conjugate to the in-focus plane prevents detection of light from out-of-focus planes, thus achieving a thin optical section of illumination. TIRF microscopy utilizes the total internal reflection of light that occurs when light travels through media of decreasing refractive indices,

e.g. when light travels through glass into an aqueous specimen, at an angle greater than a defined critical angle (relative to normal) (Figure 1.1 A). Total internal reflection of light creates a low energy evanescent field of illumination along the surface of the aqueous specimen, generating a thin fluorescent plane of excitation that only penetrates approximately 100 nm into the specimen (Figure 1.1 B). TIRF microscopy develops a thinner optical section compared with high-resolution confocal microscopy (100 nm for TIRF vs. 1 μm for confocal), advantageous for the study of unitary Ca^{2+} channel activity at the plasma membrane. However, this can also be a disadvantage for recording intracellular Ca^{2+} releases events. Confocal microscopy is more useful for this purpose as the plane of excitation can be focused within the cytosol. Both TIRF and confocal Ca^{2+} imaging rely on high affinity fluorescent Ca^{2+} reporter molecules with rapid binding kinetics to resolve Ca^{2+} signals. The cell permeable, non-ratiometric Ca^{2+} indicators Fluo-3 AM (*70*) and Fluo-4 AM (*71*) are most commonly used to record transient Ca^{2+} signals. More recently, genetically encoded Ca^{2+} indicator proteins have been utilized in Ca^{2+} imaging experiments. Most of these molecules are green fluorescent protein-calmodulin (CaM) fusion proteins like Pericams (*72*), GCaMP2 (*73, 74*), and Cameleon (*75*). Targeted expression, allowing Ca^{2+} signals to be recorded from specific tissues without contamination from other cell types, constitutes a major advantage of genetically encoded vs. chemical Ca^{2+} indicators. In addition, genetic expression reduces loading variability associated with chemical indicators. Thus, advances in Ca^{2+} imaging techniques and Ca^{2+} indicators have greatly improved the ability to optically resolve unitary Ca^{2+} channel activity and have expanded the type of information that can be obtained from such experiments.

Optical recording of Ca^{2+} channel activity presents distinct advantages over conventional electrophysiological methods. Spatial information regarding channel location on the plasma membrane is gained and simultaneous channel activity can be recorded from the entire bottom surface of the plasma membrane. Moreover, optical methods are less invasive compared to patch-clamp techniques, allowing intracellular signaling pathways to remain intact. The main disadvantage of optical vs. patch clamp recording is lack of membrane voltage clamp. To overcome this problem, the two techniques can be applied simultaneously. Ultimately, both methods will continue to be used to study Ca^{2+} influx pathways.

The most complete example of the power of these new optical approaches was reported in a sophisticated series of studies by the Santana laboratory, which exploited TIRF microscopy to investigate unitary Ca^{2+} influx events through L-type ($Ca_V1.2$) Ca^{2+} channels in vascular smooth muscle cells (for review see ref. 78). These events, called "L-type Ca^{2+} channel sparklets," (*76*) and are recorded by imaging membrane Ca^{2+} signals in Ca^{2+} indicator-loaded cells with TIRF microscopy under voltage-clamp conditions while background cytosolic Ca^{2+} is buffered with the slow chelator EGTA. L-type Ca^{2+} channel sparklets are low amplitude Ca^{2+} signals (Table 1.2), therefore, the thin fluorescent excitation plane generated by TIRF coupled with intracellular Ca^{2+} buffering is critical for resolution. Sparklets are distinct from Ca^{2+} sparks, another well-described Ca^{2+} signal present in smooth muscle cells (*77*). Sparklets are recordings of Ca^{2+} influx occurring through individual Ca^{2+}-permeable ion channels present on the plasma membrane and are abolished by removal of extracellular Ca^{2+} but unaffected by intracellular Ca^{2+} store depletion. Ca^{2+} sparks are Ca^{2+} release events from intracellular

stores via ryanodine receptors located on the sarcoplasmic reticulum and are abolished by store depletion. Recordings of Ca^{2+} sparks and sparklets (and other localized Ca^{2+} signaling events) are easily distinguishable by their biophysical properties, such as amplitude and spatial spread (Table 1.2).

Application of the TIRFM approach led to the discovery of several important aspects of L-type Ca^{2+} channel regulation in arterial myocytes. For example, although L-type Ca^{2+} channels are broadly distributed throughout the surface of smooth muscle cells, L-type Ca^{2+} channel sparklet activity is non-random, i.e. almost all channel activity occurs at a few persistently active sites on the sarcolemma (*78*). High activity L-type Ca^{2+} channels were found to be modulated by protein kinase A (PKA), protein kinase Cα (PKCα), and calcineurin (*79-81*). PKA- and PKCα-dependent changes in L-type Ca^{2+} channel activity is partly due to their interaction with protein A kinase-anchoring proteins (AKAPs), which are required for PKA-dependent modification of L-type Ca^{2+} channels (*82, 83*) and for intracellular targeting of PKCα (*79*). Taken together, the actions of PKA, PKCα, AKAPs, and calcineurin account for the variation in L-type Ca^{2+} channel activity. This body of work highlights the potential of optical recoding methods to reveal fundamental aspects of Ca^{2+} influx mechanisms not detected by other means.

TRP CHANNEL SPARKLETS

Optical techniques have recently been employed to record unitary Ca^{2+} influx events through TRP channels in vascular endothelial cells. Like L-type Ca^{2+} channel sparklets, unitary Ca^{2+} influx events through TRP channels are called “TRP channel

sparklets," and the molecular identity of the responsible TRP channel is specified (*1, 9*). For example, single channel Ca^{2+} influx events through TRPV4 are called "TRPV4 sparklets." TRPV4 sparklets were recently characterized in primary human microvascular endothelial cells (*1*). In this study, endothelial cells were loaded with the fast Ca^{2+} indicator dye Fluo-4 AM, and sparklets at the plasma membrane, indicated by transient fluorescent signals, were recorded using TIRF microscopy (Figure 1.2). Sparklet frequency was increased by the TRPV4 agonists 4α-phorbol 12,13-didecanoate (4α-PDD), GSK1016790A, and 11,12-EET, inhibited by the TRPV4-selective antagonist HC-067047, and nearly abolished in the absence of extracellular Ca^{2+}, demonstrating that these signals represent TRPV4-mediated Ca^{2+} influx (*1*). TRPV4 channel sparklets in endothelial cells are larger in amplitude compared with L-type Ca^{2+} channel sparklets in smooth muscle cells and can be recorded in the absence of exogenous cytosolic Ca^{2+} buffers and without voltage clamp. Custom software (LC_Pro) implemented as a plugin for ImageJ (*84*) was used to autodetect fluorescent signals and calculate the amplitude, duration, and spatial spread for each TRPV4 sparklet recorded. Using this method, the biophysical properties of TRPV4 sparklets were characterized (Table 1.2). TRPV4 sparklets were rare under basal conditions, but readily recruited upon stimulation of TRPV4 with an agonist (*1*). Additionally, even during maximal stimulation only a few TRPV4 sparklet sites per cell (i.e. active TRPV4 channels) were detected, even though immunolabeling experiments revealed that TRPV4 protein was widely distributed (*1*). This is the first evidence demonstrating that most TRPV4 channels in primary endothelial cells are "silent", suggesting a potential non-conducting role for TRPV4 protein.

The characteristics of endothelial cell TRPV4 sparklets are distinct from other Ca^{2+} signals recorded from vascular endothelial and smooth muscle cells (Table 1.2). It is noteworthy that TRPV4 sparklets recorded from endothelial cells of different vascular beds (dermal vs. mesenteric) and species (human vs. mouse) using different recording conditions (TIRF and Fluo-4 vs. confocal and GCamP2) and analysis methods displayed remarkable similarity in GSK1016790A-stimulated frequency, amplitude, and spatial spread (Table 1.2). The duration of TRPV4 sparklets differed between the two studies. This discrepancy is due to differences in analysis method (manual vs. automated) or could be due to differences in the preparation (primary endothelial cells vs. intact endothelium). However, it is clear that TRPV4 sparklets are a novel Ca^{2+} microdomain in endothelial cells with definable biophysical properties that are distinct from Ca^{2+} microdomains that have been previously described.

TRPV4 SPARKLETS CAUSE VASODILATION

An elegant study by Sonkusare et al. examined the functional significance of TRPV4 sparklets in the intact endothelium of mouse mesenteric arteries (*9*). A novel feature of this study was the use of $Cx40^{BAC}$-GCaMP2 mice, a strain genetically modified to express a Ca^{2+}-binding biosensor protein, GCaMP2, preferentially in the vascular endothelium. GCaMP2 mice allow for Ca^{2+} imaging of endothelial cell Ca^{2+} signals without background from other cell types, such as perivascular nerves or vascular smooth muscle cells (*73, 74*). Mesenteric arteries from $Cx40^{BAC}$-GCaMP2 mice were isolated and pinned *en face*, and TRPV4 sparklets were recorded from the

intact endothelial layer using high speed, high resolution confocal microscopy (*9*). Mesenteric artery endothelial TRPV4 sparklets were evoked by activators of TRPV4 (GSK1016790A, 4α-PDD, and 11,12-EET), were blocked by the TRPV4-specific inhibitor HC-067047, and were absent from $TRPV4^{-/-}$ mice, providing the first evidence that unitary TRPV4 activity can be optically recorded from intact mesenteric arteries (*9*).

Interestingly, mesenteric artery TRPV4 sparklet recordings demonstrate cooperativity in terms of channel gating. The amplitudes of a majority of the recorded signals were consistent with four simultaneous channel openings i.e., a "four-channel meta-structure" (*9*). In addition, similar to responses recorded from primary human endothelial cells (*1*), only 4-8 TRPV4 channels per cell were active during near-maximal stimulation with the potent TRPV4-selective agonist GSK1016790A (10 nM) (*9*), Surprisingly, the activity of these few TRPV4 channels is sufficient to hyperpolarize the endothelial cell plasma membrane and evoke maximal endothelium-dependent dilation of isolated, pressurized mesenteric arteries (*9*) by an EDH mechanism involving SK_{Ca} and IK_{Ca} channels (Figure 1.3) (*9*). High concentrations of GSK1016790A (100 nM) resulted in excessive increases in global Ca^{2+} and severe vasomotion of the isolated arteries (*9*), suggesting that over-stimulation of TRPV4 in the endothelium may have a pathophysiological role. Together, these findings indicate the significance of TRPV4 sparklets in EDH and vascular regulation in mouse mesenteric arteries.

SIGNIFICANCE OF TRP CHANNEL SPARKLETS

Endothelial dysfunction is a hallmark of common cardiovascular diseases such as atherosclerosis, stroke, and hypertension, establishing the critical nature of this fragile tissue for the maintenance of vascular health. Important functions of the endothelium are regulated by changes in intracellular Ca^{2+}, emphasizing the significance of Ca^{2+} influx pathways. Recent improvements in confocal and TIRF microscopy used in conjunction with sensitive Ca^{2+} indicator molecules allow for the direct visualization of unitary TRP channel Ca^{2+} influx events, or "TRP channel sparklets," in endothelial cells. Significant advantages of optical vs. traditional electrophysiological techniques of studying Ca^{2+} influx channels include higher throughput, preservation of intracellular Ca^{2+} signaling pathways, and acquisition of the number and subcellular distribution of active Ca^{2+} influx sites. Use of this new methodology has uncovered unexpected aspects of TRPV4, TRPV3, and TRPA1 physiology in the endothelium, including evidence that the activity of only a few channels per cell can yield maximal endothelium-dependent vasodilation. Application of this technology to the study of other Ca^{2+}-permeable TRP channels involved in endothelium-dependent dilation is likely to yield further novel and surprising findings. Further, optical recording may prove to be particularly useful for the assessment of changes in Ca^{2+} influx pathways associated with endothelial dysfunction and the evaluation of interventions designed to resolve this pathology. In this dissertation, the biophysical properties of TRPV4, TRPV3, and TRPA1 sparklets are characterized, and the main focus of the work is determining the physiological function and pathological significance of TRPA1 channels in the cerebral artery endothelium.

Table 1.1: TRP Channels in Vascular Endothelial Cells. Relative Ca^{2+} to Na^{+} ion permeability (P_{Ca}:P_{Na}) and presence in vascular endothelial cells detected by RT-PCR, Western blot, or immunohistochemistry (updated from Wong and Yao 2011) noted for each TRP channel. The last column indicates the channels that have been reported to contribute to endothelium-dependent hyperpolarization (EDH). *ND* = Not determined. **Updated from Wong CO, and Yao X. TRP channels in vascular endothelial cells. Adv Exp Med Biol 704: 759-780, 2011.*

Channel	Selectivity P_{Ca}:P_{Na}	Present in Endothelium?(*85*)	Involved in EDH
TRPA1	0.8-7.9 (*46*)	Yes	Yes (*6*)
TRPC1	Non-selective (*86*)	Yes	
TRPC2	1-3 (*87*)	Yes	
TRPC3	1.6 (*88, 89*)	Yes	Yes (*8*)
TRPC4	1.1 (*90*)	Yes	
TRPC5	9 (*90*)	Yes	
TRPC6	5 (*89*)	Yes	
TRPC7	0.5-5.4 (*91*)	Yes	
TRPM1	<1 (*92*)	Yes	
TRPM2	0.5-1.6 (*93*)	Yes	
TRPM3	0.1-10 (*94*)	Yes	
TRPM4	Not Ca^{2+} permeable (*95*)	Yes	
TRPM5	Not Ca^{2+} permeable (*96*)	No	
TRPM6	P_{Mg}:P_{Na} ~ 6 (*97*)	Yes	
TRPM7	0.3-3 (*98*)	Yes	
TRPM8	1-3 (*44*)	Yes	
TRPML1	Non-selective (*99*)	*ND*	
TRPML2	*ND*	*ND*	
TRPML3	*ND*	*ND*	
TRPP1	1-5 (*100*)	Yes	
TRPP2	4 (*101*)	*ND*	
TRPP3	1-5 (*102*)	Yes	
TRPV1	10 (*43*)	Yes	
TRPV2	1-3 (*103*)	Yes	
TRPV3	12 (*104*)	Yes (*5, 105*)	Yes (*5*)
TRPV4	6 (*106*)	Yes	Yes (*7*)
TRPV5	100 (*54*)	No	
TRPV6	100 (*107*)	No	

Table 1.2: TRPV4 Sparklets are Distinct Ca^{2+} Microdomains. Properties of smooth muscle cell Ca^{2+} sparks, L-type Ca^{2+} channel (LTCC) sparklets, Ca^{2+} puffs, Ca^{2+} pulsars recorded using Fluo-4 AM, TRPV4 sparklets recorded using GCaMP2 indicator, and TRPV4 sparklets recorded using Fluo-4 AM. Frequency (Hz) refers to the number of Ca^{2+} events per second per cell. N/A = Not applicable.

Ca^{2+} Microdomain	**Amplitude (F/F_o or nM)**	**Duration (ms)**	**Spatial Spread (μm^2)**	**Frequency (Hz)**
Ca^{2+} Sparks (77, 108)	2 ± 0.1	30	13.6 ± 1.2	0.5 - 1
LTCC Sparklets (78)	18-280 (nM)	30, 80	0.81 ± 0.01	N/A
Ca^{2+} Puffs (109)	50-500 (nM)	1000	2 - 4	N/A
Ca^{2+} Pulsars (27)	1.77 ± 0.10	257 ± 12	15.9 ± 0.6	0.10 ± 0.02
TRPV4 Sparklets (Fluo-4) (1)	0.22 ± 0.01	520 ± 40	4.8 ± 0.8	0.48 ± 0.05
TRPV4 Sparklets (GCaMP2) (9)	0.19	37.0 ± 0.7	11.2 ± 0.4	0.7 ± 0.2

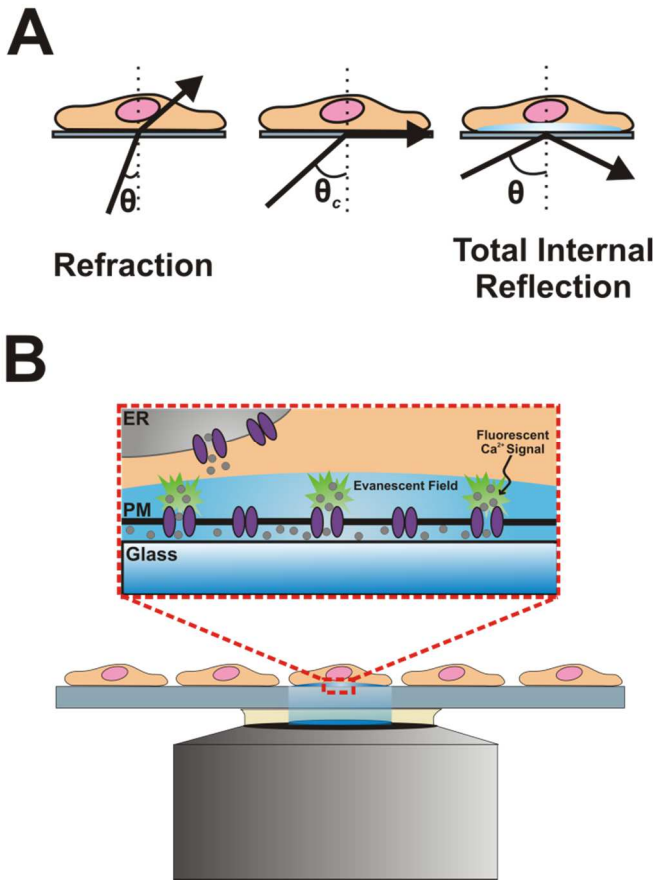

Figure 1.1: Visualization of Membrane Ca^{2+} Channels Activity Using TIRF Microscopy. (A) When light is directed toward a glass-cell interface at an angle (θ) greater than a critical angle (θ_c), light becomes totally, internally reflected away from the interface surface. The total internal reflection creates a low energy plane of illumination (evanescent field) penetrating only ~100 nm into a cell. (B) This allows for the visualization of plasma membrane (PM) Ca^{2+} channel activity without background cytosolic Ca^{2+} sources. Ca^{2+} (gray circles) that enters the cell will be bound by fluorescent Ca^{2+} indicators and produce a fluorescent signal at the site of entry. This technique allows for visualization of Ca^{2+} channel activity on the entire bottom surface of the cell.

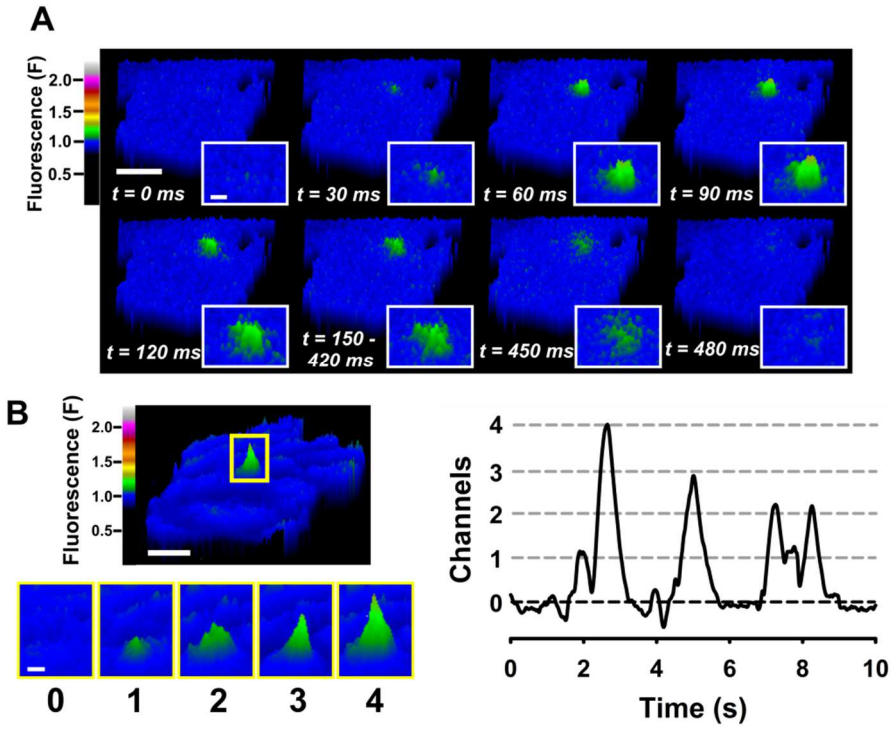

Figure 1.2: TRPV4 Sparklets in Endothelial Cells. (A) Pseudocolor timelapse of TIRF microscopy images of a primary human microvascular endothelial cell loaded with the Ca^{2+} indicator Fluo-4 AM. Unitary TRPV4 Ca^{2+} influx events (i.e. TRPV4 sparklets) are observed as transient increases in fluorescence (green); scale bar = 10 μm. Inset: Magnification of TRPV4 sparklet; scale bar = 2 μm. (B) (Left) Pseudocolored image of a rat airway smooth muscle cell TRPV4 sparklet; scale bar = 10 μm. Fluorescent signals produced from 1, 2, 3, or 4 TRPV4 channels opening are represented; scale bar = 2 μm. (Right) Recording of fluorescence (F) vs. time (s) for the noted region of interest indicating the opening of 1 to 4 TRPV4 channels.

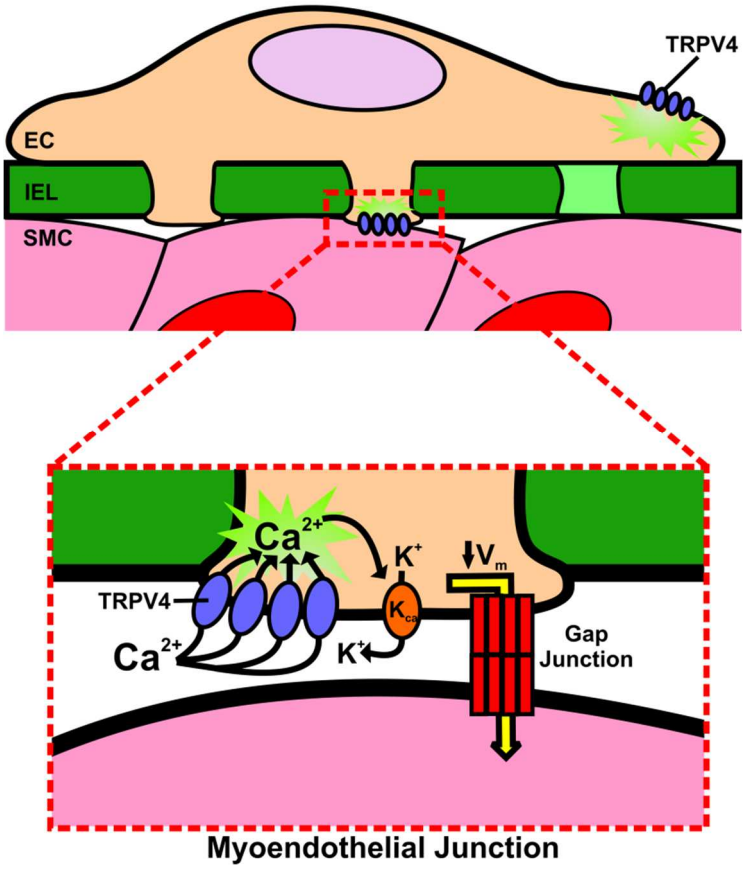

Figure 1.3: TRPV4 Sparklets in Endothelial Cells Initiate Vasodilation. TRPV4 Ca^{2+} influx from the extracellular space through as few as 3-4 channels activates K_{Ca} channels, resulting in K^+ efflux from the cell. This hyperpolarizes the endothelial cell membrane, which directly hyperpolarizes smooth muscle cells via gap junctions located within myoendothelial junctions.

CHAPTER 2

Optical Recording Reveals Novel Properties of GSK1016790A-Induced TRPV4 Channel Activity in Primary Human Endothelial Cells

INTRODUCTION

Mechanisms controlling endothelial cell Ca^{2+} entry, removal, as well as dynamic release from and reuptake to intracellular stores play a central role in the regulation of vascular tone. For example, a rise in endothelial cell intracellular [Ca^{2+}] generates nitric oxide (NO) by increasing the activity of endothelial nitric oxide synthase (eNOS) and elevates the activity of phospholipase A_2 (PLA_2), an enzyme that liberates arachidonic acid (AA) from the plasma membrane to provide substrate for the production of potent vasoactive factors (*110*). In addition, Ca^{2+}-activated K^+ (K_{Ca}) channels are directly stimulated by a rise in intracellular [Ca^{2+}], leading to hyperpolarization of the membranes of both endothelial cells and electrically coupled vascular smooth muscle cells to elicit vasodilation (*21, 111, 112*). As endothelial dysfunction is strongly correlated with common cardiovascular diseases, such as hypertension, stroke, and atherosclerosis, new technologies that advance our understanding of Ca^{2+} movement in these cells will have considerable clinical impact. Ca^{2+} influx via members of the transient receptor potential (TRP) superfamily of cation channels can cause endothelium-dependent vasodilation (*6, 38, 113-116*), but, because ion channel activity is difficult to study in native endothelial cells, significant questions regarding the molecular identities and regulation of these channels remain unresolved.

Patch clamp electrophysiology is routinely used to study ion channel activity. This methodology yields invaluable insight into channel biophysics and pharmacology but also presents significant limitations. In the on-cell and inside-out patch clamp configurations, channel activity can only be recorded from the small portion of the cell membrane present under the patch pipette. Furthermore, the on-cell configuration does not allow membrane voltage clamp. The traditional whole-cell configuration disrupts intracellular signaling pathways when the cell membrane is ruptured and cells are dialyzed with the patch pipette solution. In addition to these inherent limitations, further impediments are presented by the morphology of native endothelial cells. Obtaining and maintaining GΩ seals with these small, extremely flat cells is exceedingly difficult, and progress tends to be deliberate. Therefore, a goal of the current study was to develop a robust, efficient method that allows ion channel activity in endothelial cells to be studied under near-physiological conditions. Parker and colleagues described a method that can be adopted for this purpose using Total Internal Reflection Fluorescence Microscopy (TIRFM) to record the unitary activity of Ca^{2+}-permeable ion channels expressed in Xenopus oocytes (*4*). In TIRFM, a low energy evanescent field of illumination is created when incident light is angled such that all of the light is reflected away from the sample (*4*). The wavelength of the evanescent field is equal to that of the incident light but only penetrates the cell surface to a depth of ~100 nm to illuminate fluorophores at or near the cell surface (*4*). When cells are loaded with fluorescent Ca^{2+} indicator dyes, such as Fluo 4-AM, Ca^{2+} microdomains at the cell surface can be imaged (*4*). This technique has significant throughput advantages over conventional patch clamp methods because it allows for simultaneous recording of all

events that occur on the bottom surface of the cell (*117, 118*). In addition, the optical method is less invasive compared to conventional voltage clamp methods and leaves the intracellular environment undisturbed.

For the current study, we adapted the TIRFM technique to record Ca^{2+} influx channel activity in primary human microvascular endothelial cells. In addition, we developed novel software (LC_Pro, an ImageJ plugin) for unbiased, automated detection and analysis of endothelial cell Ca^{2+} signals. Findings presented here demonstrate that the combination of TIRFM and Ca^{2+} signal autodetection with LC_Pro software is ideal for recording the activity of Ca^{2+}-permeable ion channels in endothelial cells. We report novel insight into regulation of TRPV4 channels by the small molecule agonist GSK1016790A gained from this method. These findings demonstrate that this methodology represents a significant improvement over the techniques currently used to study ion channel activity in primary cells.

MATERIALS AND METHODS

Cell Culture

Primary human microvascular endothelial cells from neonate dermis (Cell Systems CSC-2M1), passages 3-4, were used in these experiments. Cells were cultured in CSC Complete Medium (Cell Systems) supplemented with 10 mL Culture Boost (Cell Systems 4CB-500) and 1 mL Bac-Off® (Cell Systems). Cells were incubated at 37°C, 6% CO_2, media was changed every 2-3 days, and cells were subcultured when confluent using 0.05% trypsin-EDTA (Invitrogen). Initial resurrection of cells from stocks frozen in liquid nitrogen required coating the culture flask with

Attachment Factor (Cell Systems) before addition of media and cells. Prior to experiments cells were trypsinized and plated (9 x 10^3 cells/mL) on 35 mm Mattek dishes (14 mm microwell, Fisher Scientific). Cells were incubated overnight at 37°C, 6% CO_2.

Total Internal Reflection Fluorescence Microscopy

TIRFM recordings (3 ms exposure time) were acquired using a through-the-lens TIRF system built around an inverted Olympus IX-70 microscope equipped with an Olympus PlanApo x60 oil-immersion lens (numeral aperature = 1.45) and an Andor iXON CCD camera. Cells were loaded with Fluo 4-AM (4 μM) for 20 minutes at 37°C, 6% CO_2 in the dark. Cells were washed with and imaged in a physiologic HEPES-buffered solution (in mM): 2.5 $CaCl_2$, 146 NaCl, 4.7 KCl, 0.6 $MgSO_4$, 0.15 $NaHPO_4$, 0.1 ascorbic acid, 8 glucose, 10 HEPES (pH 7.4). All experiments were performed at room temperature (22-25°C). Each recording was 1000 frames and ~20-40 seconds in length.

LC_Pro Data Analysis

All data used in analyses were derived directly from the original TIRFM recordings. Recordings were processed using a custom algorithm implemented as a plugin (LC_Pro) for ImageJ software specifically designed to: 1) detect statistically significant fluorescent signals within background noise, 2) automatically define circular regions of interest (ROIs, 15 pixel diameter) centered at active sites containing statistically significant fluorescent signals, and 3) calculate mean fluorescence

intensities within ROIs to determine specific event parameters. 8-bit gray scale TIFF image sequences are input into LC_Pro/ImageJ, initially specifying the ROI size (15 pixels) and the frame rate of the input video, and event statistics are generated as the final output, according to the program flow chart outlined in Francis et al., 2012 (*84*). Briefly, *Image Processing* was performed through a series of steps: normalization of 8-bit gray scale image stacks to 0.01% saturated pixels, generation of a background frame from a minimum intensity projection of the image sequence, subtraction of the background frame from the original image sequence, and subtraction of a mean intensity projection of the sequence from the background-subtracted image sequence. The resulting image sequence is then divided by the time-dependent standard deviation of the background-subtracted image sequence. The ImageJ Particle Analyzer java class was then used to assign best fit ellipses at the center of each event. During *Event Processing*, the mean intensity within each ROI (ellipse) was calculated using a modified version of the multimeasure plugin for ImageJ. Events are defined as fluorescent signals that meet several criteria: 1) a spatial restriction of ≥ 12.56 pixels per frame, 2) a temporal restriction of ≥ 2 frames, and 3) signal that falls within $P < 0.01$ for Gaussian variation. The statistical rigor underlying these stringent criteria for event classification allow for substantially high signal-to-noise discrimination of fluorescent signals. *ROI Processing* follows, where location (x,y), spatial spread, amplitude, duration, attack time, and decay time were then calculated for each event. LC_Pro was customized for our study by the addition of a step in the program flow prior to the calculation of event duration (during *ROI Processing*) in which the left and right side differences between peak and baseline fluorescence (F) were calculated and expressed

as ΔF. Duration is expressed as the time interval at 50% max peak fluorescence. Spatial spread is calculated as the area of the maximum best fit ellipse at 95% of the peak fluorescence of an event. The LC_Pro plugin for ImageJ can be downloaded from the ImageJ website: http://imagej.nih.gov/ij/plugins/lc-pro/index.html.

RNA Isolation and RT-PCR

Total RNA was extracted from endothelial cells (RNeasy Protect Mini Kit) and first-strand cDNA was synthesized using an Omniscript Reverse Transcriptase kit (both from QIAGEN, Valencia, CA). PCR was performed using primer sets specific for TRPV4 (Qiagen QT00077217), yielding a product of 149 bp. PCR products were resolved on 2% agarose gels. PCR reactions always included a template-free negative control. The PCR product was sequenced to confirm its identity.

Immunocytochemistry

Immunocytochemistry was used to confirm expression of TRPV4 in primary human microvascular endothelial cells. Cells were fixed with 4% formaldehyde for 10 minutes, permeabilized with methanol (-80°C), blocked with 2% bovine serum albumin (in phosphate buffered saline), and incubated with a primary rabbit monoclonal antibody specific to TRPV4 (1:250, Alomone Labs ACC-034) overnight at 4°C. Cells were washed and incubated with a fluorescent secondary antibody (goat anti-rabbit) conjugated with a Texas Red fluorophore (1:1000, Santa Cruz Biotechnology sc2780) for 2 hours at room temperature in the dark. Fluorescence images for immunocytochemistry were obtained using a FluoView 1000 laser-scanning confocal

microscope (Olympus) and a ×60, 1.4 numerical aperture oil immersion objective with the pinhole diameter set for 1 Airy Unit. Excitation of Texas Red was by illumination with the 543 nm line set at 74% transmission, and emission was collected using a variable band-pass filter set to 555–655 nm. Excitation of DAPI was by illumination with the 405 nm line set at 0.1% transmission, and emission was collected using a variable band-pass filter set 475-575 nm. All images were acquired at 1024 × 1024 pixels at 4.0 µs/pixel and were analyzed in ImageJ version 1.44b.

Statistics

All data are means ± SE. Values of *n* refer to the number of cells for each experiment. Statistical tests used for each data set are as follows: One-way analysis of variance (ANOVA) was used to test for differences in whole-cell event frequency between treatments with Ca^{2+} free and CPA; where significant, individual groups were compared using a Student-Newman-Keuls post hoc test (Figure 2.1 b). Unpaired t-tests were used to determine whole-cell frequency differences with addition of 4α-PDD (Figure 2.4 e). Two-way ANOVA was used to test for differences in whole-cell frequency differences between treatments in both the ruthenium red and HC-067047 experiments as well as the detection method comparison experiments; where significant, individual groups were compared using a Student-Newman-Keuls post hoc test (Figure 2.4 f, 2.4 g, 2.7 a). Paired t-tests were used to test for differences in the quantity of events and event sites before and after treatment with GSK1016790A (Figure 2.7 b). For comparison of non-Gaussian distributed data, a Mann-Whitney rank sum test was used to determine significant differences (Table 2.1). A level of $P \leq 0.05$

was accepted as statistically significant for all experiments. Histograms were constructed and fit using OriginPro v8.5, and SigmaPlot v11.0 was used to make the figures. The concentration response curve (Figure 2d) was constructed by fitting data to a four parameter logistic equation (SigmaPlot v11.0).

RESULTS

Novel Subcellular Ca^{2+} Influx Events in Primary Human Microvascular Endothelial Cells

Localized, transient increases in fluorescence were observed at the surface of endothelial cells loaded with Fluo 4-AM and imaged using TIRFM (Figure 2.1a, Figure 2.2). Recordings were analyzed using LC_Pro to automatically identify subcellular regions with statistically significant changes in surface fluorescence, and the location, amplitude (ΔF = local current peak F – local current minimum F), spatial spread, duration, attack time (duration from 50% F to local peak F), and decay time (duration from local peak F to 50% F) of each event was determined. A noise threshold filter (ΔF ≤ 0.1) was established based on a common peak observed in event amplitude histograms under all recording conditions. Whole-cell event frequency (Hz) was calculated as total events per cell per second. Under basal conditions, events had a mean amplitude (ΔF) of 0.39 ± 0.01, attack time of 0.88 ± 0.06 s, decay time of 0.99 ± 0.07 s, duration of 2.67 ± 0.13 s, whole-cell event frequency of 0.11 ± 0.02 Hz, and a spatial spread of 6.26 ± 2.01 μm^2 (n = 125). These Ca^{2+} signals are longer in duration compared to previously described Ca^{2+} events, such as Ca^{2+} sparks (*119*), sparklets (*120*), and Ca^{2+} pulsars (*27*) (Table 2.2).

To determine if events recorded from endothelial cells using TIRFM result from Ca^{2+} influx from the extracellular solution or from Ca^{2+} release from intracellular stores, we disrupted Ca^{2+} release from the endoplasmic reticulum (ER) with the sarcoplasmic/endoplasmic reticulum Ca^{2+} ATPase (SERCA) pump inhibitor cyclopiazonic acid (CPA, 10 μM). To demonstrate the efficacy of CPA treatment, global Ca^{2+} levels were recorded during administration. As expected, global Ca^{2+} levels initially rose upon addition of CPA, and fluorescence returned to basal levels within 15 minutes (Figure 2.3). Recordings were obtained from cells pre-treated with CPA (15 min) to preclude the possibility of recording store-activated Ca^{2+} influx events. CPA had no effect on basal whole-cell event frequency (0.12 ± 0.04 Hz, n = 40 for control; 0.15 ± 0.05 Hz, n = 31 for CPA) (Figure 2.1b). In contrast, we observed that whole-cell event frequency was nearly abolished when Ca^{2+} was removed (no added Ca^{2+}, 3 mM ethylene glycol-bis(2-aminoethylether)-N,N,N',N'-tetraacetic acid (EGTA)) from the extracellular solution (0.12 ± 0.04 Hz, n = 40 for control; 0.01 ± 0.003 Hz, n = 39 for Ca^{2+} free) (Figure 2.1b). These findings indicate that the Ca^{2+} signals recorded using TIRFM represent Ca^{2+} influx from the extracellular solution.

Histograms for event amplitude, duration, attack time, decay time, and spatial spread were constructed (Figure 2.1c). Event amplitudes and durations were broadly distributed, suggesting that the recorded signals result from the activity of multiple types of Ca^{2+} influx channels that were active under these conditions.

Unitary TRPV4 Channel Activity Recorded using TIRFM

TRPV4 was identified as a specific molecular target to further evaluate the utility of TIRFM for recording Ca^{2+}-permeable channel activity in endothelial cells. TRPV4 was selected because of its biophysical properties, tissue distribution, physiological significance, and available selective pharmacology. TRPV4 channels are slightly selective for Ca^{2+} ions (P_{Ca2+}/P_{Na+} ~ 9:1), are present in the endothelium of cerebral, mesenteric, as well as other arterial beds, and are involved in endothelium-dependent vasodilation (*39, 115, 121, 122*). Furthermore, selective pharmacology, including a recently described TRPV4 inhibitor (HC-067047) (*123*) and TRPV4 activators (GSK1016790A and 4α-PDD) (*54, 124*), is available.

To establish the presence of TRPV4 in the cells used for this study, reverse transcriptase-polymerase chain reaction (RT-PCR) was performed using total RNA prepared from primary human microvascular endothelial cells. A band was detected at the expected amplicon length of 149 bp, indicating that TRPV4 mRNA is present (Figure 2.4a). TRPV4 protein was detected by immunolabeling (Figure 2.4b), whereas very little fluorescence was present when the primary antibody was omitted (Figure 2.4c), indicating specificity of labeling. TRPV4 protein appears to be uniformly distributed throughout the cell (Figure 2.4b).

The effects of the potent TRPV4 agonist GSK1016790A (0.1 nM to 1 μM) were recorded using TIRFM. GSK1016790A increased whole-cell event frequency in a concentration-dependent manner with a near maximal response at [GSK1016790A] ≥ 100 nM (*n* = 20-30 cells at each concentration) (Figure 2.4d). The EC_{50} value determined from these data (26.9 nM) is within an order of magnitude of the reported

EC_{50} value (3 nM) determined using patch clamp electrophysiology for TRPV4 activation with GSK1016790A in a HEK 293 expression system (*124*). GSK1016790A was used at a concentration of 100 nM in all subsequent experiments to achieve maximal stimulation. Cell death, indicated by an irreversible global increase in Ca^{2+}, was observed in ~10% of cells exposed to GSK1016790A at this concentration. Data from cells that died during recording were excluded from analyses. GSK1016790A-induced increases in whole-cell event frequency were abolished with removal of extracellular Ca^{2+} (0.07 ± 0.03 Hz (*n* = 10) for control, 0.01 ± 0.01 Hz (*n* = 20) for Ca^{2+} free + vehicle, and 0.002 ± 0.002 Hz (*n* = 16) for Ca^{2+} free + GSK1016790A (100 nM)), demonstrating that these events result from influx of extracellular Ca^{2+}. A second, structurally-distinct TRPV4 agonist, 4α-PDD (10 μM), also increased whole-cell Ca^{2+} event frequency in primary endothelial cells (0.05 ± 0.02 Hz, *n* = 13 for control; 0.36 ± 0.10 Hz, *n* = 21 for 4α-PDD) (Figure 2.4e). 11,12-epoxyeicosatrienoic acid (11,12-EET) is a potent vasodilator, activates TRPV4 channels (*55*) and is endogenously produced by vascular endothelial cells (*125*). 11,12-EET (3 μM) also increased the whole-cell frequency of Ca^{2+} events relative to vehicle (1% DMSO), (0.01 ± 0.01 Hz, *n* = 18 for vehicle; 0.05 ± 0.02 Hz, *n* = 19 for 11,12-EET) (Figure 2.5). These findings demonstrate activation of TRPV4-mediated Ca^{2+} influx events in endothelial cells by an endogenously produced vasodilator.

The effects of the non-specific TRPV blocker ruthenium red (10 μM) and the selective TRPV4 blocker HC-067047 (500 nM) on baseline and GSK1016790A-stimulated (100 nM) Ca^{2+} events were examined. Cells were pre-treated with physiologic solution containing blocker (ruthenium red or HC-067047) or vehicle

(distilled water for ruthenium red or DMSO for HC-067047) for 5 minutes at room temperature prior to experimentation. Neither blocker altered the basal Ca^{2+} influx event frequency (Figure 2.4 f and g). In the absence of ruthenium red, GSK1016790A (100 nM) stimulated an increase in the whole-cell frequency of Ca^{2+} events recorded with TIRFM (0.05 ± 0.01 Hz, *n* = 29 vs. 0.38 ± 0.10 Hz, *n* = 17) (Figure 2.4f). A similar response to GSK1016790A (100 nM) was observed in the absence of HC-067047 treatment, (0.09 ± 0.04 Hz, *n* = 26 vs. 0.59 ± 0.11 Hz, *n* = 19) (Figure 2.4g). In contrast, GSK1016790A (100 nM) failed to stimulate an increase in event frequency in the presence of ruthenium red (0.11 ± 0.04 Hz, *n* = 43 vs. 0.15 ± 0.03 Hz, *n* = 44) or HC-067047 (0.05 ± 0.02 Hz, *n* = 28 vs. 0.18 ± 0.09 Hz, *n* = 23) (Figure 2.4 f and g). Taken together, these findings indicate the presence of endogenous, functional TRPV4 channels in human microvascular endothelial cells and demonstrate that the activity of these channels can be recorded and analyzed using TIRFM and LC_Pro.

TRPV4-Mediated Ca^{2+} Influx Events are Distinct from Basal Events

Ca^{2+} influx events stimulated by GSK1016790A (100 nM) were further characterized by histogram analysis of event amplitude, spatial spread, duration, attack time, and decay time (Figure 2.6 b-d). Interestingly, a fit of event amplitudes displays quantal separation (i.e., ΔF = 0.12, 0.18, 0.23, 0.30, etc.), suggesting that these signals represent the activity of an integral number of TRPV4 channels with a unitary ΔF value of ~0.06 (*n* = 59) (Figure 2.6b). Single TRPV4 channel activity (ΔF = 0.06) is apparent in some tracings (Figure 2.6c) but could not be resolved from noise in most recordings. Spatial spread, duration, attack, and decay were all narrowly distributed around the

respective means (Figure 2.6d), consistent with the activation of a single type of ion channel. The mean amplitude of GSK1016790A-induced events was smaller than that of control events and the mean duration, attack, and decay times were significantly shorter (Figure 2.6a, Table 2.1). Spatial spread did not differ between groups but tended to be smaller for GSK1016790A-induced Ca^{2+} influx events (Table 2.1).

TRPV4-mediated increases in whole-cell event frequency following agonist stimulation could be due to an elevation of the frequency of Ca^{2+} influx through basally active channels or could result from the recruitment of new event sites. To distinguish between these possibilities, endothelial cell Ca^{2+} events were recorded before and after stimulation with GSK1016790A (100 nM). The total number of events (4.78 ± 1.71 vs. 12.78 ± 3.33) and the number of event sites (4.22 ± 1.40 vs. 8.89 ± 1.86) per cell was increased following treatment with GSK1016790A (100 nM) (n = 9) (Figure 2.7). Masks of event sites detected by LC_Pro before and after agonist stimulation were constructed, color coded, and merged (Figure 2.7a). The sites active before (green) vs. after (red) agonist administration did not overlap. Of the 9 cells that were studied in this experiment, only two had a single site that was active both before and after administration of GSK1016790A. These findings indicate that basal and GSK1016790A-induced Ca^{2+} influx events are mediated by distinct populations of ion channels, and that quiescent TRPV4 channels are recruited by the agonist. Interestingly, although TRPV4 channels appear to be uniformly distributed throughout the endothelial cell plasma membrane (Figure 2.4b), we detected only a few sites of activity using TIRFM when a near-maximal concentration of GSK1016790A was administered (Figure 2.7a). These data suggest that much of the channel protein

present in endothelial cells is either not present on the plasma membrane or is inactive under these conditions.

DISCUSSION

The goal of the current study was to develop an efficient method for investigating the activity of Ca^{2+}-permeable ion channels in primary endothelial cells. We find that: 1) novel, transient, subcellular Ca^{2+} influx events can be recorded from primary human endothelial cells and characterized using a combination of TIRFM and LC_Pro autodetection analysis, 2) the selective TRPV4 agonist GSK1016790A elicits concentration-dependent increases in the whole-cell frequency of Ca^{2+} influx events that are attenuated by TRPV4 antagonists and abolished in the absence of extracellular Ca^{2+}, 3) the peak amplitude distribution of GSK1016790A-induced Ca^{2+} influx events displays quantal separation, suggesting that single channel activity can be recorded, 4) GSK1016790A-induced Ca^{2+} influx events represent newly-recruited TRPV4 channels, rather than increased activity of previously established sites, and 5) much of the TRPV4 channels present in endothelial cells remain silent during maximal agonist stimulation. Together, these data demonstrate that basal and TRPV4 Ca^{2+} influx events can be distinguished and characterized using our combined TIRFM/LC_Pro approach. Moreover, our findings are consistent with the conclusion that GSK1016790A-activated Ca^{2+} influx events represent recruitable TRPV4 channel activity in primary endothelial cells. Importantly, these results establish that using TIRFM with selective pharmacology and LC_Pro autodetection to record Ca^{2+}-permeable ion channel activity in the

endothelial cells improves experimental efficiency as well as sensitivity and provides spatial information not provided by conventional patch clamp techniques.

Changes in intracellular [Ca^{2+}] mediate critical functions of the endothelium, including capillary permeability, changes in membrane potential, and production of vasoactive substances. Because voltage clamp electrophysiology is difficult to efficiently apply to native endothelial cells due to their small size and flat morphology, much remains unknown about the Ca^{2+} influx pathways contributing to the regulation of these processes. The current findings demonstrate that TIRFM is a significant improvement over conventional patch clamp electrophysiology for studying Ca^{2+} influx channels in primary endothelial cells. Benefits of TIRFM compared to voltage clamp include higher throughput, the ability to record from cells in an unperturbed state, and the capability to simultaneously record the location and biophysical properties of multiple Ca^{2+} signals from each cell. In addition, the TIRFM approach provides spatial information that cannot be obtained using traditional patch clamp electrophysiology. The principle disadvantage of the TIRFM method is the lack of voltage clamp, but this can be compensated for by manipulating the ionic content of the extracellular solution. Additionally, the TIRFM technique detects only Ca^{2+} influx and does not measure outward currents or currents resulting from the movement of other ions, such as Na^+ or K^+, that contribute to the total activity of nonselective cation channels. Despite these minor limitations, our findings clearly demonstrate the advantages of TIRFM for recording the activity of Ca^{2+}-permeable ion channel activity in endothelial cells. Confocal microscopy could also be used to study unitary Ca^{2+} influx events in endothelial cells. We selected TIRFM over confocal microscopy for the current study in

order to be consistent with the method used in prior work studying Ca^{2+} influx channels (*126*).

The findings of this study demonstrate that distinct types of Ca^{2+} influx events can be recorded from primary endothelial cells using a combination of TIRFM and selective pharmacology. Prior reports suggest that endothelial cells express multiple Ca^{2+} influx channels, including several TRP channels (TRPC1, TRPC3, TRPC4, TRPV3, TRPV4, and TRPA1) (*5, 6, 37-39*), the cyclic nucleotide-gated channel A1 (CNGA1) (*34, 35*), and the ATP-sensitive purinergic ligand-gated receptor channel P2X4 (*36*). Consistent with these observations, Ca^{2+} influx events recorded from unstimulated primary endothelial cells exhibit a broad distribution of event amplitude and duration, suggesting that these signals arise from more than one type of channel. This study provides the first evidence of spontaneous Ca^{2+} channel activity in primary human microvascular endothelial cells. The specific TIRFM properties of one channel, TRPV4, were characterized using selective pharmacological tools. Ca^{2+} signals stimulated by a TRPV4 agonist exhibited quantal separation in amplitude, were much shorter in duration (~8.5-fold), and tended to be larger in area compared with those recorded from unstimulated cells. These data establish a distinctive biophysical "TIRFM fingerprint" for TRPV4 channels in primary endothelial cells. Similar TRPV4 Ca^{2+} influx events were recently described in intact mouse mesenteric arteries (*9*). Using a similar approach, other channels can be characterized and identified by their unique properties, enabling rapid identification of Ca^{2+}-permeable ion channels in endothelial and other types of cells. Thus, in addition to being a powerful research tool, the TIRFM/LC_Pro technique can be used in a clinical setting to study native endothelial cells under normal

and pathophysiological conditions. For example, endothelial cells isolated from patients via peripheral artery biopsy (*127*) could be examined by TIRFM/LC_Pro for changes in endothelial cell Ca^{2+} channel activity associated with endothelial dysfunction and cardiovascular disease. The technique may be particularly useful for evaluating the mechanisms of action for drugs designed to improve endothelial function.

The selective agonist GSK1016790A has been extensively used to study the physiological role of TRPV4 channels (*124, 128-132*). However, little is currently known about how GSK1016790A stimulates TRPV4 channel activity. Application of the TIRFM technique revealed new insight into activation of TRPV4 activity by this agonist in primary endothelial cells. We show here for the first time that Ca^{2+} influx stimulated by GSK1016790A originates from newly-recruited, rather than from previously active, TRPV4 channels. These findings suggest that under the conditions used for this study, TRPV4 channels have a very low open probability. Consistent with this conclusion, neither ruthenium red nor the selective TRPV4 blocker HC-067047 diminished Ca^{2+} event frequency under basal conditions, suggesting that events recorded under basal conditions are very unlikely to be mediated by TRPV4 or any other TRPV channel. Interestingly, even maximal stimulation of TRPV4 channels with GSK1016790A produced only relatively modest increases in the whole cell frequency of Ca^{2+} influx events and event sites. These findings are consistent with those recently reported by Sonkusare et al. (*9*), demonstrating that activation of as few as 3 TRPV4 channels per endothelial cell is sufficient to induce maximal dilation of mouse mesenteric arteries. In addition, the current findings also show that much of the TRPV4 channel protein present in primary endothelial cells is inactive during maximal agonist stimulation. The role of

"silent" TRPV4 channels in endothelial cells is unclear. It is possible that most of the TRPV4 protein present in primary endothelial cells is not expressed on the plasma membrane, and is either non-functional or contributes to cellular signaling in a manner that does not involve transport of ions across the plasma membrane. Non-conducting roles for other TRP channels (TRPM1, TRPM6, TRPM7, TRPM2, TRPP1, and TRPP2), hyperpolarization-activated cyclic nucleotide-gated (HCN) channels, as well as several K^+ channels (Kv1.3, Kv10.1, and Kv11.1) have been reported (*93, 98, 133-138*). These studies demonstrate contributions of non-conducting channels to numerous cellular processes including proliferation, mitogen activating protein (MAP) kinase signaling, tumor suppression, synaptic facilitation and channel expression (*93, 98, 133-138*). It is also possible that conducting TRPV4 channels are present on intracellular membranes, such as the ER or Golgi bodies. Additional work is needed to determine the specific role of non-conducting TRPV4 channels in endothelial cells.

In summary, findings presented here demonstrate that TIRFM can be combined with selective pharmacological tools to establish characteristic properties of TRPV4 channels, suggesting that this approach can be used to study the activity of specific Ca^{2+}-permeable ion channels. Using this method, we identified new information regarding the activation of TRPV4 by the small molecule agonist GSK1016790A. Furthermore, the findings of this study demonstrate that the novel combination of TIRFM and custom automatic ROI detection software is a significantly improved method for recording and analyzing the activity of Ca^{2+}-permeable ion channels in primary endothelial cells. The approach described here may be effective for studying changes

in endothelial cell Ca^{2+} channel activity during endothelial dysfunction associated with cardiovascular disease.

Table 2.1: Comparison of Basal Ca^{2+} Influx Events vs. GSK1016790A-Induced Sparklets. Amplitude, duration, attack time, decay time, spatial spread, and whole-cell (WC) frequency (mean ± SE) of Ca^{2+} influx events recorded from primary endothelial cells under basal condition (control) or following treatment with the selective TRPV4 agonist GSK1016790A (100 nM). *P ≤ 0.05 vs. control (Mann-Whitney rank sum test); *n* = 125 for control; *n* = 59 for GSK1016790A.

Parameter	Control	GSK1016790A
Amplitude ($\Delta F/F_0$)	0.39 ± 0.01	0.22 ± 0.01*
Duration (s)	2.67 ± 0.13	0.52 ± 0.04*
Attack Time (s)	0.88 ± 0.06	0.32 ± 0.03*
Decay Time (s)	0.99 ± 0.07	0.37 ± 0.03*
Spatial Spread (μm^2)	6.26 ± 2.01	4.84 ± 0.82
WC Frequency (Hz)	0.11 ± 0.02	0.48 ± 0.05*

Table 2.2: Novel Transient Ca^{2+} Events in Endothelial Cells. Ca^{2+} events observed in primary endothelial cells using TIRFM have a much longer duration compared to previously described Ca^{2+} microdomains. This suggests that the events recorded using TIRFM in endothelial cells are novel.

Ca^{2+} Microdomains	**WC Frequency (Hz)**	**Duration (s)**
Sparks	0.24	0.03
Sparklets	N/A	0.03, 0.08
Pulsars	0.10 ± 0.02	0.26
Events in ECs	0.11 ± 0.02	2.67 ± 0.13

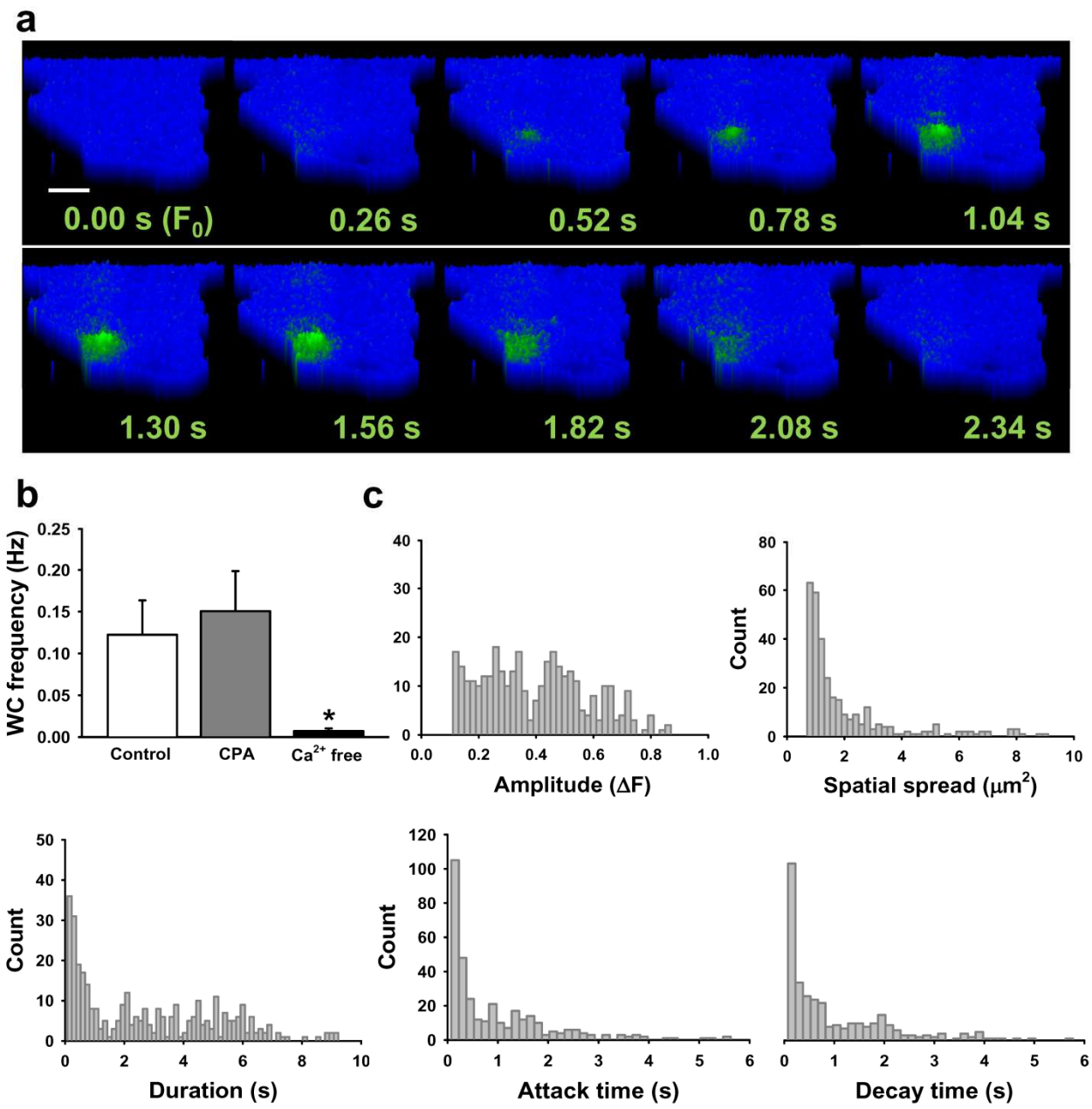

Figure 2.1: Novel Subcellular Ca^{2+} Influx Events in Primary Human Microvascular Endothelial Cells. (a) Pseudocolor time lapse of a typical Ca^{2+} event recorded under control conditions; scale bar = 8 μm. (b) Mean data showing that depleting intracellular Ca^{2+} stores by pretreating with the SERCA pump inhibitor cyclopiazonic acid (CPA, 10 μM) had no effect on whole-cell (WC) event frequency, whereas removing extracellular Ca^{2+} diminished event frequency; *n* = 40 for control, *n* = 31 for CPA, *n* = 39 for Ca^{2+} free; *P ≤ 0.05 vs. control. (c) Histograms of event amplitude, spatial spread, duration, attack time, and decay time. Event amplitudes and duration are randomly distributed, suggesting that multiple types of Ca^{2+} channels are active under basal conditions; *n* = 125 cells.

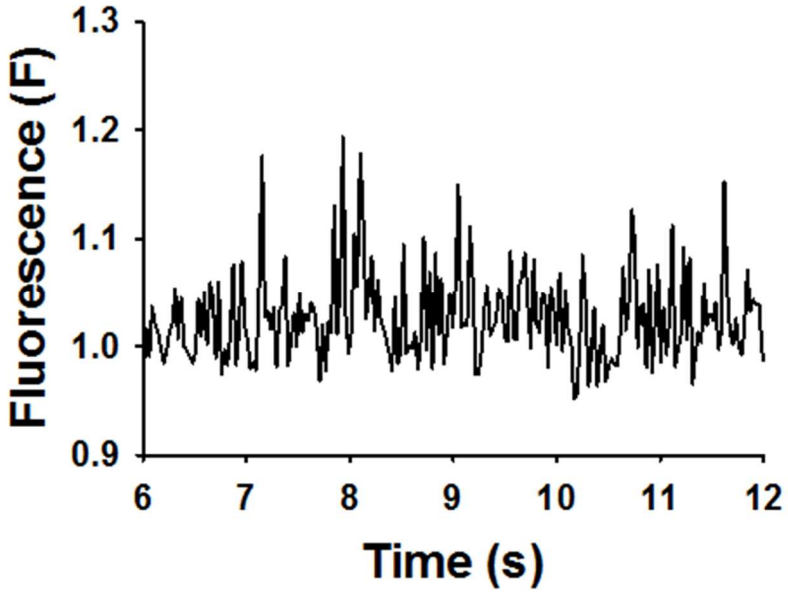

Figure 2.2: Basal Event Amplitudes are Broadly Distributed. Representative trace of fluorescence (F) over time within an active ROI on an unstimulated cell. Event amplitudes display a broad, random distribution, indicating the activity of multiple Ca2+ influx channels under basal conditions.

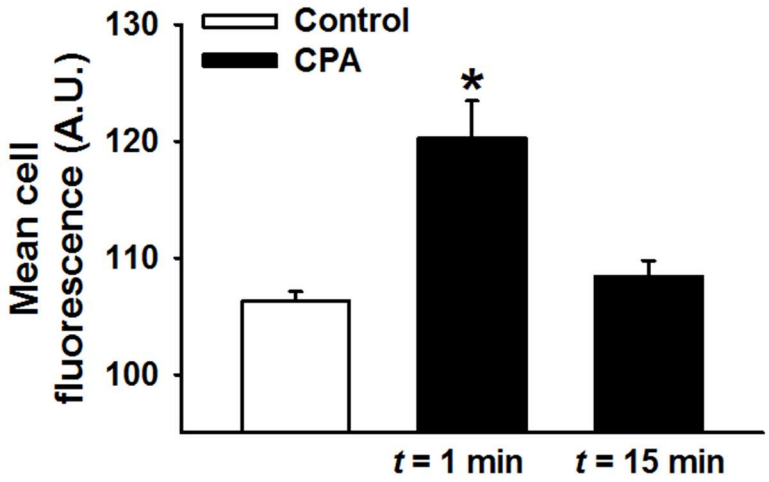

Figure 2.3: Endothelial Cell CPA Treatment. Mean cell fluorescence (A.U.) of cells before (control) and 1 or 15 minutes following addition of CPA (10 μM). n = 10 for all groups; *P ≤ 0.05 vs. Control.

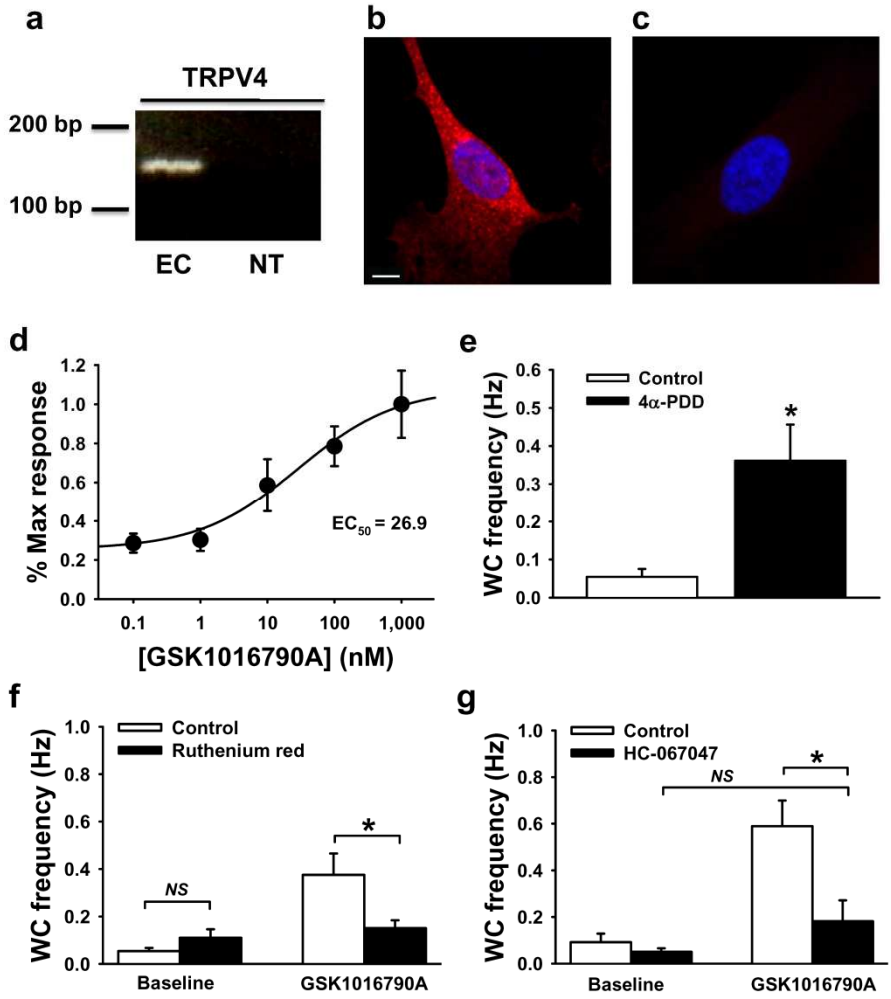

Figure 2.4: TRPV4 Sparklets Recorded using TIRFM. (a) RT-PCR for TRPV4 using total RNA from primary endothelial cells (EC) compared to a no DNA template control (NT); representative of 3 experiments. (b) Compressed z-stack images of immunolabeled TRPV4 (red) in primary endothelial cells vs. no primary antibody control (c). Nuclei are labeled with DAPI (blue); scale bar = 10 μm. Representative of 3 experiments. (d) Concentration response curve showing the effects of the selective TRPV4 agonist GSK1016790A on whole-cell (WC) Ca^{2+} event frequency. (e) Mean data showing that the TRPV4 agonist 4α-PDD (10 μM) also increases the whole-cell (WC) frequency of Ca^{2+} influx events; *n* = 13 for control, *n* = 21 for 4α-PDD; *P ≤ 0.05 vs. control. Pretreatment with the non-specific TRPV blocker ruthenium red (10 μM) (f) or the selective TRPV4 inhibitor HC-067047 (500 nM) (g) decreased the stimulation of Ca^{2+} event frequency in response to GSK1016790A (100 nM) but had no effect on baseline event frequency. For ruthenium red experiments, under baseline conditions *n* = 29 for control and *n* = 43 for ruthenium red, in the presence of GSK1016790A *n* = 17 for control and *n* = 44 for ruthenium red. For HC-067047 experiments, under baseline conditions *n* = 26 for control and *n* = 28 for HC-067047, in the presence of GSK1016790A- *n* = 19 for control and *n* = 23 for HC-067047; *NS* = No statistically significant differences detected; *P ≤ 0.05 vs. control.

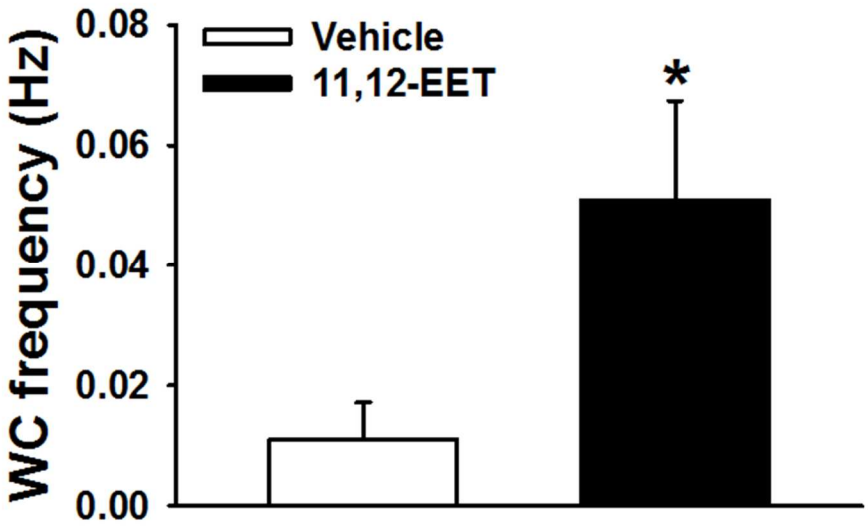

Figure 2.5: 11,12-EET Stimulates TRPV4 Sparklets in Endothelial Cells. Mean data showing an increase in the whole-cell (WC) frequency of Ca^{2+} events with addition of 11,12-EET (3 μM) to the bathing solution compared to vehicle addition (1% DMSO). n = 18-19 per group; *P ≤ 0.05 vs. vehicle.

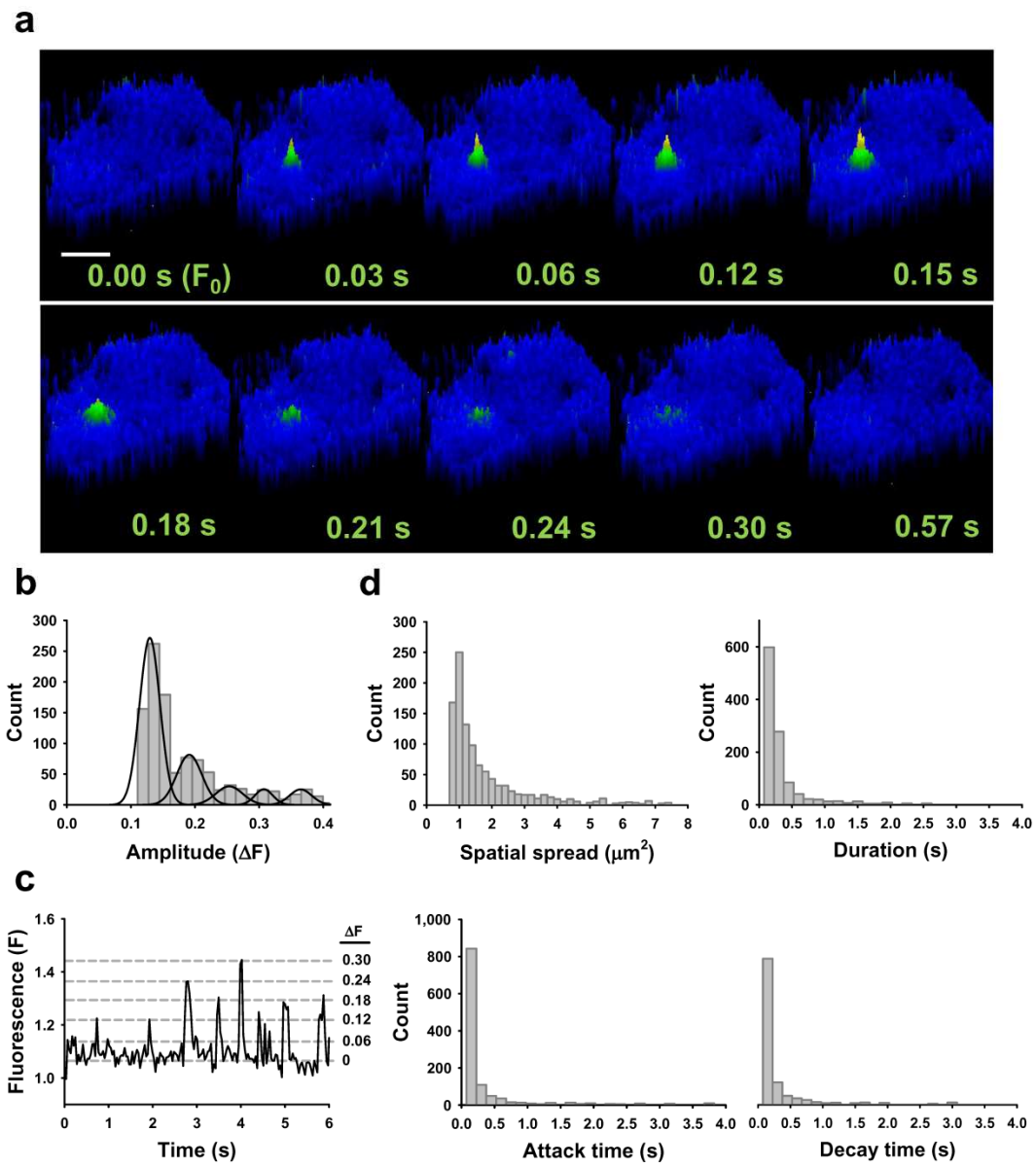

Figure 2.6: TRPV4 Sparklets are Distinct from Basal Events. (a) Pseudocolor time lapse of a typical Ca^{2+} event recoded from a cell treated with GSK1016790A (100 nM); scale bar = 8 μm. (b) Histogram analysis of Ca^{2+} event amplitude in cells treated with GSK1016790A indicating quantal separation. These event levels can also be observed in a representative plot of fluorescence vs. time (c). (d) Histograms of spatial spread, duration, attack, and decay in cells treated with GSK1016790A.

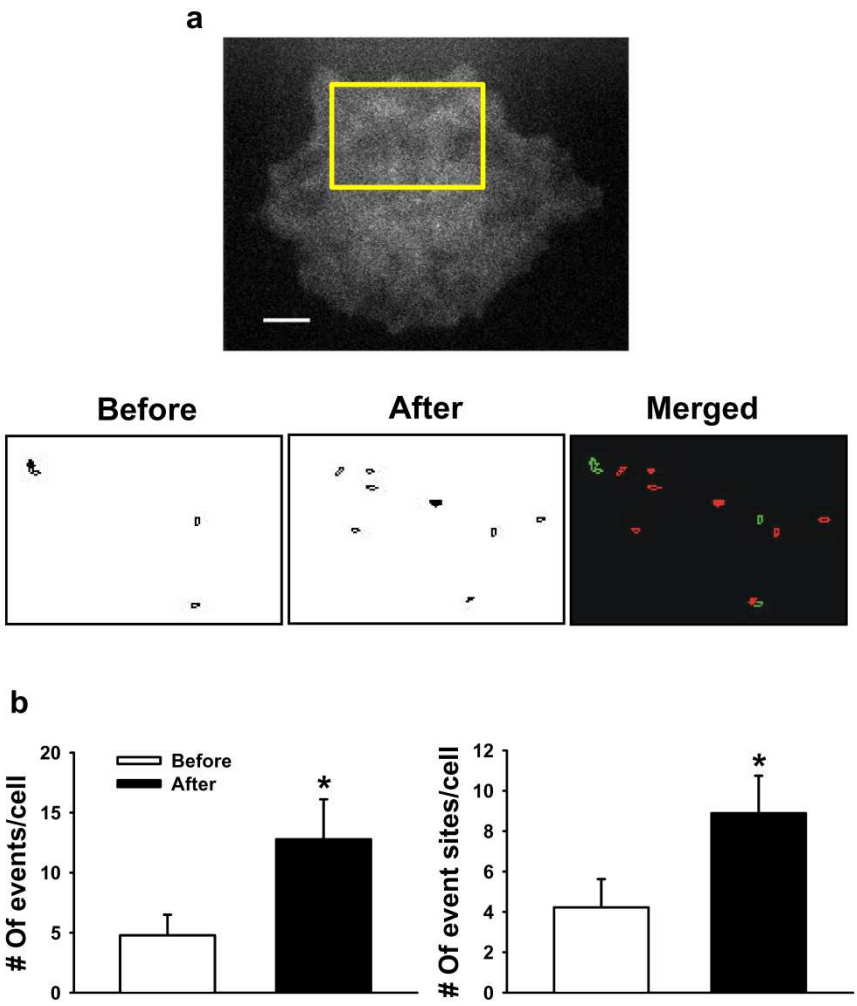

Figure 2.7: GSK1016790A Increases Whole-Cell Event Frequency by Recruiting New Ca^{2+} Event Sites. (a) (Top) TIRFM image of a typical primary endothelial cell. Ca^{2+} influx sites detected by LC_Pro for the indicated region are shown before (left) and after (middle) addition of GSK1016790A (100 nM). The merged pseudocolor image (right) shows events before addition of GSK1016790A in green and after in red. There is no overlap between the event sites. (b) Mean data showing the number of events (left) and the number of event sites (right) per cell before and after addition of GSK1016790A (4.78 ± 1.71 events/cell before vs. 12.78 ± 3.33 events/cell after and 4.22 ± 1.40 sites/cell before vs. 8.89 ± 1.86 sites/cell after, *n* = 9 for each group); *P ≤

CHAPTER 3

Localized TRPA1 Channel Ca^{2+} Signals Stimulated by Reactive Oxygen Species Regulate Cerebral Artery Dilation

INTRODUCTION

Regulation of the cerebral circulation differs from that of the rest of the body to meet the metabolic demands and specific anatomical constraints of the brain. One example of this disparity is the observation that reactive oxygen species (ROS) such as superoxide anions (O_2^-) and hydrogen peroxide (H_2O_2) primarily cause vasodilation in the cerebral circulation and vasoconstriction in peripheral arteries (*139*). The NADPH oxidase (NOX) family, consisting of five isoforms (NOX1-5), is a major source of ROS in the vasculature (*140, 141*). Although it is understood that generation of ROS by NOX is much greater in healthy cerebral arteries than in other vascular beds (*142*), the molecular mechanism responsible for translating these higher amounts of ROS into a qualitatively different vascular response is not known.

Potential candidate mediators of the vascular actions of ROS include Ca^{2+}-permeable members of the transient receptor potential (TRP) channel family, several of which are present in the vasculature and can be regulated by ROS and ROS-derived products (*143-146*). One such channel is the lone member of the ankyrin TRP (TRPA) subfamily, TRPA1. Initially characterized as a detector of noxious electrophilic substances in nociceptive and sensory neurons (*46, 51*), TRPA1 has since been shown to be present in mast cells, enterochromaffin cells, epithelial cells, and other tissues, suggesting a broader biological role for this channel. TRPA1 is present in the

endothelium and mediates vasodilation of cerebral arteries in response to allyl isothiocyanate (AITC) (*6*), a pungent compound found in mustard oil. Endogenous regulators of TRPA1 activity in the endothelium are currently unknown. However, in vagal and sensory nerves, hypoxic and hyperoxic conditions can increase TRPA1 activity (*48*). Additional evidence, also obtained in neurons, indicates that TRPA1 is activated by oxidative modification of cysteines in its cytoplasmic N-terminus by ROS, including H_2O_2 and O_2^- (*145, 147*). TRPA1 is also activated by compounds produced by peroxidation of ώ6 polyunsaturated fatty acids in the plasma membrane, such as 4-hydroxy-nonenal (4-HNE), 4-oxo-2-nonenal (4-ONE), and 4-hydroxy-hexenal (*145, 148*). 4-HNE and related substances are produced by hydroxyl radicals (OH•) formed during degradation of H_2O_2 (*149*), suggesting that the oxidant and redox signaling mechanisms acting on TRPA1 could be linked by the lipid peroxidation process. This proposed signaling cascade has not been studied in vascular endothelium and its effects on TRPA1 activity, endothelial function, and vasomotor responses have not been characterized.

Elementary Ca^{2+} influx events through single TRPV4 channels have been optically recorded from endothelial cells using total internal reflection fluorescent (TIRF) and confocal microscopy (*1, 9*). These events, termed “TRPV4 sparklets,” are fundamental signals underlying endothelium-dependent dilation of mesenteric arteries (*9*). In theory, all Ca^{2+}-permeable TRP channels with sufficient conductance are capable of being detected optically as sparklets, with amplitude, frequency, and spatial spread reflecting the unitary conductance, Ca^{2+} permeability, and gating kinetics of the channel.

Prior studies are consistent with the possibility that TRPA1 channels are critical sensors of cellular oxidant and redox status. However, little is currently known about the relationship between ROS generation and TRPA1 channel activity in the endothelium. Moreover, it is not clear how the potential of these channels to serve as ROS sensors in the vasculature could account for differences in the effects of ROS between the peripheral and cerebral circulations. Here, we investigated how NOX-generated ROS could provoke vasodilation through activation of TRPA1 channels and sought to determine how this response differed between cerebral and peripheral arteries. We showed that TRPA1 co-localizes with NOX isoform 2 (NOX2) in the endothelium of cerebral arteries but not in other vascular beds. We further developed a method for recording and characterizing TRPA1 sparklets, demonstrating the presence of large-amplitude TRPA1 sparklets with unique properties in cerebral artery endothelial cells. Finally, we demonstrated that ROS generated by NOX increased TRPA1 sparklet frequency and dilated cerebral arteries through a process that requires the peroxidation of membrane lipids. Taken together, these data indicate that Ca^{2+} influx through TRPA1 channels elicits endothelium-dependent vasodilation in response to the generation of lipid peroxidation products, and this response is specific to the cerebral vasculature.

MATERIALS AND METHODS

Animals

Male Sprague-Dawley rats (300–400 g; Harlan) were deeply anesthetized with pentobarbital sodium (50 mg, I.P.) and euthanized by exsanguination. Male and female

mice (10-12 weeks old) were deeply anesthetized by isofluorane inhalation (3%) and euthanized by decapitation. Brains were isolated and placed in ice-cold MOPS-buffered saline. Cerebral and cerebellar arteries were isolated from the brain, cleaned of connective tissue, and stored in MOPS-buffered saline. The University of Nevada School of Medicine and Colorado State University IACUCs approved all animal procedures.

Generation of eTRPA1$^{-/-}$ Mice

eTRPA1$^{-/-}$ mice were created by crossing mice homozygous for loxP-flanked TRPA1 S5/S6 transmembrane domain construct ("floxed TRPA1"; The Jackson Laboratory, 008650 *B.129-TRPA1$^{tm2KyKw>/J}$*) and mice hemizygous for *Cre* recombinase under the control of the receptor tyrosine kinase *Tek* (Tie2) promoter/enhancer (Jackson Lab *B6.Cg-Tg(Tek-cre)1$^{Ywa/J}$*). *Tek* imparts consistent *Cre* expression exclusively in the endothelium during development and adulthood. F1 progeny positive for *Cre* were mated with homozygous floxed TRPA1 mice. F2 progeny were genotyped by PCR using genomic DNA obtained from ear or tail biopsies, and those positive for *Cre* and homozygous for floxed TRPA1 were crossed with homozygous floxed TRPA1 mice. *eTRPA1$^{-/-}$* mice are viable and fertile. Control mice were homozygous for floxed TRPA1 but negative for *Cre*.

RNA Isolation and RT-PCR

For rat samples, total RNA was extracted and purified from left main and septal coronary, renal interlobar, cerebral, cerebellar and first to fourth-order mesenteric

arteries. For human samples, total RNA was isolated from human cerebral arteries or isolated smooth muscle cells, as well as primary human microvascular endothelial cells from neonate dermis and human brain microvascular endothelial cells; total RNA from human renal glomerular endothelial cells (4005) and human cardiac microvascular endothelial cells (6005) was obtained from ScienCell Research Laboratories. First-strand cDNA was synthesized, and PCR was performed using primer sets specific for rat *TRPA1*, rat *eNOS*, human *TRPA1*, or human *eNOS*. PCR reactions always included a template-free negative control. Approval to use the human tissues and cells was granted by the University of Calgary Institutional Review Board.

Immunohistochemistry

Immunohistochemistry was performed on arteries in the *en face* preparation as previously described (*6*). Briefly, arteries were isolated, cleaned of connective tissue, and cut open longitudinally. Tissue was fixed with 4% formaldehyde, then permeabilized and blocked with a phosphate-buffered saline (PBS) solution containing 1% Triton X-100 and 2% bovine serum albumen (BSA). Arteries were incubated with primary antibody overnight at 4°C, then washed and incubated with a Texas Red-conjugated secondary antibody for 2 hours at room temperature. Tissue was washed and mounted on a slide with UltraCruz Mounting Medium (Santa Cruz Biotechnology, sc-24941), which contains DAPI nuclear stain. Fluorescence images were obtained using a FluoView 1000 laser-scanning confocal microscope (Olympus).

Western Blotting

Human brain samples were obtained in accordance with the guidelines of the *Declaration of Helsinki* after obtaining approval from the University of Tennessee Health and Science Center review board and receiving written informed consent. A temporal lobe sample was obtained from an adolescent male who underwent a lobectomy and had no history of hypertension or stroke. The cerebral tissue was immediately placed in chilled Dulbecco's Modified Eagle Medium (DMEM) for transportation. Human cerebral arteries were dissected from the sample within 1–2 hours of surgery and placed in ice-cold physiologic saline solution (PSS). Arteries were then transferred to chilled RIPA buffer for lysis, after which sodium dodecyl sulfate (SDS) was added and samples were heated in a boiling water bath for 3 minutes. Following protein estimation, samples were run on an SDS-polyacrylamide gel, transferred onto a nitrocellulose membrane, blocked with 5% milk, and incubated overnight with anti-TRPA1 antibody. The lower part of the same blot was cut and probed independently for actin. Membranes were washed with TBS-Tween 20 buffer and incubated with secondary antibody for 1 hour. Proteins were visualized using SuperSignal West Pico Chemiluminescent Substrate (ThermoFisher Scientific).

Western Blotting for Mouse TRPA1

Cerebral and cerebellar arteries from each mouse were isolated and snap frozen in liquid nitrogen. 50 µL RIPA lysis buffer (Pierce) containing a protease inhibitor cocktail (Calbiochem) was added to each artery sample and homogenized by sonication (20 x 2 sec pulses) and mechanical disruption by a Fisher Scientific Tissuemiser (10

sec) on ice. Samples were then centrifuged at 13,000 rpm for 10 min, and the supernatant was transferred to a new tube. Protein concentration for each sample was determined using a BCA Protein assay (Pierce). 10 ng of each protein sample was added to SDS sample buffer and heated at 70°C for 10 min. Immediately following denaturation, proteins were separated by SDS-PAGE and then transferred to a nitrocellulose membrane. Membranes were blocked with 5% milk, 1% BSA in PBS containing 0.1% Tween and 0.02% sodium azide (PBS-TA) for 30 min at room temperature on a rocker and then exposed to a rabbit anti-TRPA1 antibody (1:500, Alomone Labs) in 5% milk, 1% BSA (PBS-TA) overnight at room temperature on a rocker. The membrane was then washed with PBS-T 3 x 5 min and exposed to a goat anti-rabbit HRP-conjugated secondary antibody (1:10,000, Invitrogen) in 5% milk, 1% BSA (PBS-T) for 2 hours at room temperature on a rocker. The membrane was then washed 5 x 5 min with PBS-T, incubated in Supersignal ECL substrate (Pierce) for 1-3 min, and imaged. Protein amount was quantified using ImageJ software.

Co-Immunoprecipitation

Cerebral and cerebellar arteries from each mouse were snap frozen in liquid nitrogen. 50 µL IP Lysis Buffer (Pierce) containint a protease inhibitor cocktail (Calbiochem) was added to each artery sample and homogenized using a Fisher ScientificTissuemiser (10 sec) on ice. Samples were then centrifuged at 13,000 rpm for 10 min, and the supernatant was transferred to a new tube. Protein concentration for each sample was determined using a BCA Protein assay (Pierce). Co-immunoprecipitation was performed using a Dynabeads Protein G Immunoprecipitation

kit (Invitrogen) according to protocol. 50 µL Dynabeads were added to a tube and placed on the DynaMag-2 magnet to separate the beads from the solution. The solution was removed and 200 µL Ab Binding and Washing Buffer containing 2 µg of rabbit anti-TRPA1 antibody (Alomone Labs) or goat anti-NOX2 antibody (Santa Cruz Biotechnologies) was added to the beads. Tubes were incubated at room temperature on a rocker to allow antibodies to bind the beads for 10 min. The tube was then placed on the magnet to separate the bead-Ab complexes from the solution and unbound antibodies. Bead-Ab complexes were then washed with 200 µL Ab Binding and Washing Buffer and again separated from the supernatant. 10 µg of protein was diluted in 100 µL IP buffer and added to the tube containing the bead-Ab complexes and incubated at room temperature for 10 min on a rocker. The tube was then placed on the magnet, and the supernatant was transferred to a clean tube for later use. The bead-Ab-Ag complexes were then washed 3x with 200 µL Washing Buffer, resuspended in 100 µL Washing Buffer, transferred to a new tube, and place on the magnet to remove the supernatant. The bead-Ab-Ag complexes were resuspended in 20 µL Elution Buffer, 7.5 µL 4x SDS sample buffer, and 2.5 µL ddH_2O. The supernatant and 10 µg input protein samples were diluted in 7.5 µL 4x SDS sample buffer and ddH_2O to a total volume of 30 µL. All three samples (pull-down, supernatant, and input) were heated at 70°C for 10 min. Samples were immediately used for SDS-PAGE and Western blotting using a similar method as described above using an anti-TRPA1 antibody (1:500, Alomone Labs) or an anti-4-HNE antibody (1:1000, Abcam).

Cerebral Artery Endothelial Cell Isolation

Basilar arteries were cut into three segments. Each was then pinned onto a Silgard block, cut open longitudinally, and placed intima-side down onto 35-mm microwell MatTek dishes coated with Matrigel containing 1 drop of supplemented medium. Tissue was incubated at 37°C, 6% CO_2 for 4–5 hours to allow adherence, then additional media was added. The medium was changed every 2–3 days. After 1 week, tissue was removed from culture, and migrated endothelial cells were allowed to proliferate. Endothelial cells were identified by their typical cobblestone-like appearance. RT-PCR and immunocytochemistry were used to confirm the presence of *eNOS* and *TRPA1* mRNA in the isolated cells.

TRPA1 Sparklet Recording and Analysis

TIRF microscopy was performed essentially as previously described (*1*). Briefly, TIRFM recordings (3 ms exposure time) were acquired using a through-the-lens TIRF system built around an inverted Olympus IX-70 microscope equipped with an Olympus PlanApo 60x oil-immersion lens (numeral aperture = 1.45) and an Andor iXON CCD camera. Cells in a physiological HEPES-buffered solution were loaded with Fluo-4 AM for 20 minutes at 37°C, 6% CO_2 in the dark and imaged. All experiments were performed at room temperature (22-25°C). Endothelial cells were superfused with HEPES-buffered solution containing experimental drugs: AITC (30 μM), NADPH (10 μM), HC-030031 (10 μM), apocynin (30 μM), gp91ds-tat (1 μM), scr. gp91ds-tat (1 μM), catalase (500 U/mL), deferoxamine (100 μM), 4-HNE (300 nM). Each recording was 1500 frames and ~30–60 s in length.

TIRF image data were processed using a custom algorithm implemented as a plugin (LC_Pro) for ImageJ software essentially as previously described (*1*). Location (x,y), amplitude, duration, attack time, decay time, and spatial spread were then calculated for each event. Fluorescence is expressed as ΔF, the difference between peak fluorescence (F) and the local minimum fluorescence within each region of interest (ROI). Duration is defined as the time interval at 50% maximum peak fluorescence. Attack and decay time are determined by the time interval from 50% peak-to-peak fluorescence (attack) or from peak fluorescence to 50% peak (decay). Spatial spread is calculated as the area of the maximum best-fit ellipse at 95% of the peak fluorescence of an event.

Isolated Vessel Experiments

Isolated vessel experiments were performed as previously described (*6*). Briefly, after transferring to a vessel chamber (Living Systems), arterial segments were cannulated on a glass micropipette, secured with monofilament thread, pressurized to 20 mmHg with physiological saline solution (PSS), and superfused with warmed (37°C), aerated PSS to equilibrate for 15 minutes. Inner diameter was continuously monitored using video microscopy and edge-detection software (Ionoptix). Viability of the tissue was assessed by exposing pressurized arteries (20 mmHg) to isotonic PSS containing 60 mM KCl. Arteries were allowed to equilibrate for an additional 15 minutes, then pressurized to 80 mmHg (rat) or 60 mmHg (mouse) and allowed to develop stable myogenic tone. A change in diameter in response to superfusion of experimental drugs (NADPH (10 μM), HC-030031 (10 μM), LNNA (300 μM), indomethacin (10 μM), TRAM-

34 (1 μM), apocynin (30 μM), gp91ds-tat (1 μM), scr. gp91ds-tat (1 μM), catalase (750 U/mL), deferoxamine (100 μM),or 4-HNE (10 μM)) was recorded. Passive diameter was determined by superfusing vessels with Ca^{2+}-free PSS (no added Ca^{2+}, 3 mM EGTA). Percent myogenic tone was calculated as the difference in active and passive diameter at 80 mmHg divided by the passive diameter and multiplied by 100. Percent dilation was calculated as the change in myogenic tone between baseline and treatment.

Proximity Ligation Assay

Co-localization of TRPA1 with either NOX2 or NOX4 in primary rat cerebral artery endothelial cells or intact, *en face* rat cerebral arteries was studied using an *in situ* proximity ligation assay (PLA) detection kit (Duolink, Olink Biosciences, Inc.) (*150*), essentially as previously described (*151*). Cells and vessels were fixed with 4% formaldehyde for 10 or 20 minutes, respectively, at room temperature followed by a 2-hour fixation at 4°C. After washing with PBS, cells or vessels were permeabilized with cold methanol (-80°C) or 1% triton X, respectively, and incubated overnight in a 2% BSA blocking solution containing primary antibodies. Following incubation in primary antibodies, cells or vessels were washed in blocking solution followed by three 10-minute washes with 5 mL of Duolink *In Situ* Wash Buffer A. Cells and vessels were incubated in a humidified chamber at 37°C for 1 hour in secondary anti-rabbit PLUS and anti-goat MINUS PLA probes and then washed three times (5 minutes each) in 5 mL of Wash Buffer A at room temperature. Samples were incubated in Ligation-Ligase solution for 30 minutes at 37°C in a humidified chamber and then washed three times (2 minutes each) in 5 mL of Wash Buffer A at room temperature. Lastly, samples were

incubated in Amplification-Polymerase solution for 100 minutes at 37°C in a humidified chamber and then washed twice (2 minutes each) in 5 mL of Doulink In Situ Wash Buffer B. Cells were further washed in a 1% Wash Buffer B for 1 minute and mounted using Doulink In Situ Mounting Medium containing DAPI nuclear stain. Fluorescent images were obtained using a spinning disk confocal microscope (Andor) and a 100× oil-immersion objective. Positive signals (bright red puncta) were only generated when the two PLA probes were in close proximity (<40 nm). Excitation of fluorescent puncta was achieved at 543 nm, and autofluorescence of the cytosol was illuminated at 488 nm. Images were analyzed with Volocity imaging software (v6.0; Perkin-Elmer, Inc.). Negative control experiments were performed by omitting primary antibodies or PLA probes;no positive signals were detected under these conditions. The density of positive puncta per cell was determined using an automated object-finding protocol in Volocity.

Smooth Muscle Cell Membrane Potential

Smooth muscle cell membrane potential recordings were performed in isolated, pressurized cerebral arteries as previously described (*6*). Briefly, cerebral arteries were isolated and pressurized to 80 mmHg. Smooth muscle cells were impaled through the adventitia with glass intracellular microelectrodes (tip resistance 100–200 MΩ). A WPI Intra 767 amplifier was used for recording membrane potential (E_m). Analog output from the amplifier was recorded using Ionwizard software (sample frequency 20 Hz). Criteria for acceptance of E_m recordings were *1*) an abrupt negative deflection of potential as the microelectrode was advanced into a cell, *2*) stable membrane potential for at least 1

minute, and *3*) an abrupt change in potential to ~0 mV after the electrode was retracted from the cell. Changes in smooth muscle membrane potential in response to NADPH (10 μM) and HC-030031 (10 μM) were assessed.

Data Analysis and Statistics

All data are means ± SE. Values of *n* refer to the number of cells or vessels used for each experiment. N refers to the number of animals used to generate cells or vessels. Statistical analyses were performed and graphs were constructed using SigmaPlot v11.0. Unpaired or paired *t*-tests were used to compare two groups. Multiple groups were compared using one-way or two-way analysis of variance (ANOVA) followed by a Student-Newman-Keuls post hoc test to ascertain statistical differences. A value of $P \leq 0.05$ was considered statistically significant for all experiments. Histograms were constructed and fit to multiple Gaussian functions using OriginPro v8.5, and SigmaPlot was used to create the figures. Concentration-response curves were made by fitting data to a four-parameter logistic equation using SigmaPlot.

RESULTS

TRPA1 colocalizes with NOX2 the in the endothelium of cerebral arteries but not in other vascular beds

TRPA1 mRNA was detected by RT-PCR in rat cerebral arteries but was not present in renal, coronary, or mesenteric arteries (Figure 3.1A). To confirm this unusual distribution pattern, we mounted arteries *en face* and immunolabeled the endothelium with an antibody against TRPA1. TRPA1 protein was detected in rat cerebral

endothelia, where it was abundant in perinuclear regions; it was also present within fenestrations of the internal elastic lamina (IEL), sites of close contact between the endothelial and smooth muscle cell plasma membranes known as myoendothelial projections (Figure 3.1B, arrows, inset). TRPA1 immunolabeling was not detected in coronary, mesenteric, or renal arterial endothelium (Figure 3.1B), suggesting that this channel is selectively present in the cerebral endothelia. Arteries from human subjects displayed the same TRPA1 distribution pattern. *TRPA1* mRNA was detected by RT-PCR in whole human cerebral arteries but not in isolated smooth muscle cells (Figure 3.1C) and TRPA1 protein was detected by Western blotting in tissue homogenates of human cerebral arteries (Figure 3.1D). *TRPA1* message was not detected by RT-PCR in RNA isolated from human coronary, renal glomerular, or neonatal dermal artery endothelial cells, but was found in endothelial cells from human cerebral arteries (Figure 3.1E). These findings demonstrate that the presence of TRPA1 in the endothelium is a distinctive feature of the cerebral circulation.

To test our proposal that ROS and/or ROS-derived products are endogenous agonists of TRPA1 in the endothelium, we first examined cerebral arteries for the presence of NOX isoforms. NOX5 is not present in rats or mice, and NOX3 is found only in the inner ear (*152*); however, the other three isoforms are present in the rodent vasculature (*153, 154*). We detected three NOX isoforms—NOX1, NOX2, and NOX4—in the endothelium of cerebral arteries by immunolabeling (Figures 3.1F and 3.2). All three isoforms were present in perinuclear regions and IEL fenestrations, but NOX2 and NOX4 were more abundant in myoendothelial projections compared with NOX1 (Figures 3.1F, insets, and Figure 3.2).

We used *in situ* proximity ligation assays (*150*) to investigate whether NOX2 and NOX4 colocalized with TRPA1 in the endothelium. Proximity ligation assays for TRPA1:NOX2 produced abundant red puncta indicating significant co-localization (≤40 nm) in cerebral artery endothelial cells (Figure 3.1G). Proximity ligation assays for TRPA1:NOX4 revealed few red puncta (Figure 3.1G), indicating that NOX4 and TRPA1 are separated by more than 40 nm. Few puncta (~1–2 per cell) were present when primary antibodies were omitted. We also used proximity ligation assays to assess TRPA1 and NOX co-localization in intact cerebral arteries (Figure 3.1H). These assays revealed the presence of puncta throughout the endothelium, including in IEL fenestrations, in arteries probed with antibodies against NOX2 and TRPA1 (Figure 3.1H, 3.4). Proximity ligation assays for NOX4 and TRPA1 produced significantly fewer puncta (Figure 3.1H). Our data indicate that TRPA1:NOX2 complexes are present in cerebral artery endothelial cells within myoendothelial junctions and in other regions. Co-immunoprecipitation for NOX2 and TRPA1 failed to detect direct interaction between the two proteins (Figure 3.6A). These data demonstrate that NOX2 and TRPA1 selectively co-localize but do not physically interact in the cerebral artery endothelium, suggesting that metabolites generated by NOX2 could regulate TRPA1 activity in this tissue.

ROS stimulate TRPA1 sparklet activity in cerebral artery endothelial cells

We studied changes in TRPA1 activity in cerebral artery endothelial cells in response to ROS by using TIRF microscopy to record subcellular Ca^{2+} signals representing Ca^{2+} influx through single TRPA1 channels, which we called TRPA1

sparklets. To initially characterize TRPA1 sparklets, we treated primary cerebral artery endothelial cells loaded with the Ca^{2+} indicator dye Fluo-4 AM with the TRPA1 agonist allyl isothiocyanate (AITC). Very few events were seen under basal conditions, but AITC induced a concentration-dependent increase in sparklet frequency (Figure 3.7 A and B). The half–maximal effective concentration (EC_{50}) for sparklet activation was 4.4 μM (Fig. 3.7B), similar to the previously reported EC_{50} for AITC-induced dilation of cerebral arteries (EC_{50} = 16.4 μM) (*6*). The increase in sparklet frequency stimulated by AITC was not affected by depletion of intracellular stores with cyclopiazonic acid (Figure 3.6B) but was absent when cells were bathed in Ca^{2+}-free solution (Figure 3.8B), indicating that these signals are generated by influx of Ca^{2+}. The selective TRPA1 antagonist HC-030031 (*155*) blocked AITC-induced increases in sparklet frequency (Figure 3.7C), confirming that the subcellular Ca^{2+} influx events activated by AITC were *bona fide* TRPA1 sparklets. Single-site analysis indicated that the total number of active TRPA1 sparklet sites increased from 1.4 ± 0.7 sites to 6.1 ± 1.8 sites after the addition of AITC (Figure 3.7D), suggesting that AITC recruited previously inactive TRPA1 channels and did not increase the frequency of basally active sites. Further, these data showed that only about ~4–8 TRPA1 sparklet sites per cell were active during maximal stimulation.

TRPA1 sparklets recorded from cerebral artery endothelial cells were compared to those recorded from HEK 293 cells transfected with a TRPA1-GFP fusion protein. AITC caused an increase in TRPA1 sparklet frequency in transfected HEK cells that was inhibited by HC-030031 and absent in untransfected HEK cells (Figure 3.9 A and B). Modal duration, attack time, decay time, and spatial spread of TRPA1 sparklets recorded from TRPA1-GFP–transfected HEK cells were essentially identical to those

recorded from cerebral artery endothelial cells (Table 3.1). Duration histograms indicated that most TRPA1 sparklets lasted less than 200 ms and fit single exponential functions in endothelial cells (τ = 408 ms; Figure 3.7E) and transfected HEK cells (τ = 210 ms; (Figure 3.9C). Spatial spread distribution was also similar between TRPA1 sparklets recorded from endothelial cells and HEK cells, with the majority of events having an area of less than 1 μm^2 (Figures 3.7E and 3.9C).

A multiple Gaussian fit of a histogram of TRPA1 sparklet amplitudes recorded from transfected HEK cells (Figure 3.9C) indicated three distinct peaks of F/F_0 = 1.13, 1.26, and 1.39. These data suggest that the unitary TRPA1 sparklet amplitude is $\Delta F/F_0$ = 0.13, and the peaks represent the opening of one, two, or three individual TRPA1 channels, with the most frequently occurring TRPA1 sparklets (F/F_0 = 1.13) signifying the opening of a single TRPA1 channel. Identical results were obtained in endothelial cells (F/F_0 = 1.13, 1.26, 1.39), consistent with a unitary TRPA1 sparklet amplitude of $\Delta F/F_0$ = 0.13 in these native cells (Figure 3.7E). This is also apparent from plots of fluorescence intensity over time for regions of interest with active TRPA1 sparklet sites, where three distinct amplitude levels are seen (Figures 3.7F and 3.8D). Unlike TRPA1 sparklets in HEK cells, the most commonly occurring TRPA1 sparklets recorded from endothelial cells had an amplitude of F/F_0 = 1.26 ($\Delta F/F_0$ = 0.26), indicating that simultaneous opening of two TRPA1 channels at the same active site occurred much more frequently than expected. These data suggest that native TRPA1 channels exhibit binary coupled gating more frequently in cerebral artery endothelial cells compared with cloned TRPA1 channels expressed in HEK cells.

Co-localization of NOX2 and TRPA1 (Figure 3.1 G and H) in the cerebral artery endothelium supports the concept that NOX-derived ROS could regulate TRPA1 channel activity in this tissue. To test this hypothesis, NOX activity was stimulated by administration of NADPH (*156*). We found that enhanced NOX activity increased cerebral artery TRPA1 sparklet frequency in a concentration-dependent manner (Figure 3.7 G and H) and that the TRPA1 blocker HC-030031 abolished this response (Figure 3.7I). These findings indicate that NOX-derived ROS stimulate TRPA1 sparklet activity in cerebral artery endothelial cells, identifying TRPA1 as a ROS sensor in this tissue.

ROS generated by NOX dilate cerebral arteries by activating TRPA1

The effects of ROS-induced increases in TRPA1 sparklet frequency on vessel diameter were studied using intact cerebral arteries that were pressurized to physiological values (80 mmHg) to allow spontaneous myogenic tone to develop. Our data show that addition of NADPH to increase generation of ROS by NOX caused concentration-dependent vasodilation (Figure 3.10 A and B). This response was abolished by the TRPA1 blocker HC-030031 (Figure 3.10 A and C), indicating that NOX-derived ROS evoke dilation of cerebral arteries by increasing the frequency of TRPA1 sparklets.

One mechanism by which the endothelium can promote arterial dilation is by releasing diffusible substances such as nitric oxide (NO) or prostacyclin (PGI_2). We found that NADPH-induced dilation of cerebral arteries was not altered by blocking NO and PGI_2 synthesis with L-N^G-Nitroarginine (L-NNA) and indomethacin, respectively

(Figure 3.10 D and E), indicating that these pathways are not involved in the response. The endothelium can also cause dilation by direct electrotonic spread of endothelial cell membrane hyperpolarization through myoendothelial gap junctions to underlying vascular smooth muscle cells. Small and intermediate conductance Ca^{2+}-activated K^+ channels (SK and IK) are implicated in this form of endothelium-dependent vasodilation, and functional IK channels are present in cerebral artery endothelial cells at myoendothelial junctions (*6, 157*). Our data showed that intraluminal administration of the selective IK channel blocker TRAM34 nearly abolished NADPH-induced vasodilation (Figure 3.10 F and G), suggesting that TRPA1 sparklets act through IK channels in the endothelium to dilate cerebral arteries.

To determine if increases in TRPA1 sparklet activity were associated with smooth muscle cell hyperpolarization, we recorded the membrane potential of arterial myocytes from intact, pressurized (80 mmHg) cerebral arteries using intracellular microelectrodes. We found that administration of NADPH to stimulate ROS generation hyperpolarized the membranes of smooth muscle cells by approximately -8 mV (Figure 3.10 H and I). Blocking TRPA1 channels with HC-030031 abolished NADPH-induced membrane potential hyperpolarization (Figure 3.10 H and I), demonstrating that NOX-derived ROS hyperpolarize smooth muscle cells in pressurized cerebral arteries by activating TRPA1. TRPA1 channels are not present in cerebral artery smooth muscle cells (Figure 3.1C) (*5, 6*), suggesting that this response is mediated by the endothelium. Together, our findings suggest that Ca^{2+} influx through TRPA1 channels in the endothelium activates nearby IK channels to initiate K^+ efflux. The ensuing

hyperpolarization of the endothelial cell plasma membrane is conducted to underlying smooth muscle to hyperpolarize and relax that tissue, resulting in arterial dilation.

ROS-derived lipid peroxidation metabolites stimulate TRPA1 sparklets and dilate cerebral arteries

NOX-derived ROS could stimulate endothelial cell TRPA1 activity directly or through generation of lipid peroxidation products (Figure 3.11A). We found that the NOX inhibitor apocynin attenuated NADPH-induced increases in TRPA1 sparklet frequency (Figure 3.11B) and inhibited vasodilation in response to NADPH (Figure 3.11C). These findings were supported by experiments showing that NADPH-induced increases in TRPA1 sparklet frequency and NADPH-induced dilation were attenuated by the NOX2 inhibitory peptide gp91ds-tat (*158*), but not a scrambled control peptide (scr. gp91ds-tat) (Figure 3.11 B and D). These data confirm that NADPH increases the generation of ROS by a NOX isoform (probably NOX2) resulting in increased TRPA1 sparklet frequency and vasodilation.

When present on the plasma membrane, NOX produces O_2^- in the extracellular space that is rapidly dismutated to H_2O_2 by spontaneous or superoxide dismutase-catalyzed reactions (Figure 3.11A). We investigated whether H_2O_2 downstream of NOX was involved in the activation of TRPA1 by using catalase, a membrane-impermeable enzyme that rapidly degrades H_2O_2. Catalase prevented NADPH-induced increases in TRPA1 sparklet frequency (Figure 3.11B), indicating that extracellular generation of H_2O_2 is required for NOX-dependent TRPA1 activation. Administration of NADPH in the

presence of catalase constricted intact cerebral arteries (Figure 3.11E), indicating that H_2O_2 is required for NOX-dependent vasodilation. Our data indicate that increased endothelial cell TRPA1 sparklet activity and cerebral artery dilation in response to ROS generated by NOX requires the generation of extracellular H_2O_2.

In the presence of iron (Fe^{2+}), H_2O_2 is degraded to OH• through the Fenton reaction. OH• radicals are highly unstable and rapidly react with polyunsaturated fatty acids in the plasma membrane to generate lipid peroxidation products such as 4-HNE. To distinguish between the direct effects of H_2O_2 on TRPA1 activity and byproducts generated by OH•, we chelated iron with deferoxamine to inhibit the Fenton reaction and diminish the formation of OH• and lipid peroxidation (*149*). Deferoxamine blocked NADPH-induced increases in TRPA1 sparklet frequency (Figure 3.11B) and blunted NADPH-induced dilation of intact cerebral arteries (Figure 3.11F), suggesting that generation of OH• and lipid peroxidation is necessary for NOX-induced increases in TRPA1 sparklet activity and cerebral artery dilation.

These findings are consistent with the possibility that compounds generated by ROS-dependent peroxidation of polyunsaturated fatty acids such as 4-HNE and related compounds could serve as endogenous agonists of TRPA1 channels in cerebral arteries. These substances react with cysteine, histidine, and lysine residues to form stable protein adducts that are recognized by specific antibodies (*159*). To determine if lipid peroxidation metabolites are present, we probed intact cerebral arteries, mounted *en face*, with an antibody that binds to 4-HNE-modified proteins. These experiments revealed that 4-HNE-modified proteins were abundant in the cerebral artery endothelium (Figure 3.12A), with immunolabeling present in perinuclear regions and

within IEL fenestrations (Figure 3.12A, arrows, inset) where NOX2, NOX4, and TRPA1 channels are also present. Co-immunoprecipitation experiments indicated association of TRPA1 and 4-HNE in cerebral arteries (Figure 3.6B)

To test our hypothesis that lipid peroxide metabolites activate TRPA1 channels in the endothelium, we examined the effects of endogenous administration of these substances on TRPA1 sparklet activity and cerebral artery diameter. Our findings show that exogenous administration of 4-HNE induced a concentration-dependent increase in TRPA1 sparklet frequency in cerebral artery endothelial cells (EC_{50} = 64.8 nM) (Figure 3.12C) that was blocked by the TRPA1 inhibitor HC-030031 (Figure 3.12D). 4-HNE also dilated intact, pressurized cerebral arteries (Figure 3.12E). 4-HNE-induced vasodilation was concentration-dependent and was blocked by HC-030031 (Figure 3.12 F and G). 4-HNE stimulated TRPA1 sparklet activity at a much lower concentration than that required to cause vasodilation, possibly because the compound reacts with other cells in the isolated vessel preparation, reducing availability to the endothelium. Our findings indicate that the lipid peroxidation product 4-HNE can stimulate TRPA1 sparklets in the endothelium and dilate cerebral arteries.

ROS-derived lipid peroxidation products fail to dilate cerebral arteries from endothelial cell-specific TRPA1-knockout mice

We used endothelial cell-specific TRPA1 knockout (*eTRPA1*$^{-/-}$) mice to further investigate the involvement of TRPA1 channels in ROS-induced dilation in the cerebral circulation. TRPA1 immunolabeling was detected in the endothelium of cerebral arteries

from mice but not in the coronary, renal, or mesenteric artery beds (Figure 3.3). TRPA1 was not detected in Western blots of whole cerebral arteries from *eTRPA1*$^{-/-}$ mice (Figure 3.13A) and immunolabeling studies demonstrated that TRPA1 was present in DRG neurons but not in the endothelium of cerebral arteries of *eTRPA1*$^{-/-}$ mice (Figure 3.13B). AITC failed to increase the frequency of TRPA1 sparklets in cerebral artery endothelial cells from *eTRPA1*$^{-/-}$ mice (Figure 3.13C). No differences in basal vascular characteristics were observed between arteries from *eTRPA1*$^{-/-}$ compared to control mice (Table 3.2). However, administration of 4-HNE or NADPH failed to dilate intact pressurized cerebral arteries from *eTRPA1*$^{-/-}$ mice (Figure 3.13 D and E), demonstrating the critical involvement of TRPA1 channels in this response.

DISCUSSION

The brain requires continuous perfusion to provide a constant supply of oxygen and nutrients but the enclosing skull tightly limits vascular distension, presenting unique challenges to the cerebral circulation. Among other factors, endothelial control of arterial diameter is critical for precise regulation of global blood flow to the brain and for matching regional flow to metabolic demand. The ability of the endothelium to rapidly detect changes in local oxidant and redox status and effect appropriate vasomotor responses is centrally important for this function but is poorly understood. The results of the current study provide strong evidence that TRPA1 channels in the endothelium sense ROS generated by NOX. The resulting increase in Ca^{2+} influx through TRPA1 channels causes vasodilation. This pathway appears to be present only in cerebral

arteries, identifying a fundamental distinction in function between blood vessels in the brain and those in the periphery.

Our results show that elementary Ca^{2+} signals arising from the influx of Ca^{2+} through single TRPA1 channels (TRPA1 sparklets) cause endothelium-dependent dilation of cerebral vessels in response to ROS generation. Our data indicate that TRPA1 sparklets are very large Ca^{2+} influx events, with a unitary amplitude approximately twice that of a TRPV4 sparklet (*1*) ($\Delta F/F_o$ = 0.13 vs. 0.06), consistent with the larger single-channel conductance and greater Ca^{2+} permeability of TRPA1 (*46, 54, 106, 160, 161*). The signal mass of a TRPV4 sparklet was estimated to be ~100-times that of an L-type Ca^{2+} channel sparklet (*162*), suggesting that TRPA1 sparklets are at least ~200-times greater than L-type Ca^{2+} channel sparklets. We also showed that the most frequently occurring TRPA1 sparklets recorded from endothelial cells have amplitudes consistent with the simultaneous opening of two TRPA1 channels, doubling the amount of Ca^{2+} entering during a typical event. This coupled gating arrangement supports the concept that TRPA1 channels are present in a tight binary structure in the endothelial cell plasma membrane and that the opening of one of the channels in this pair triggers the adjacent channel, perhaps through binding of incoming Ca^{2+} to a Ca^{2+}-sensing EF hand domain on the N terminus (*51*). Coupled gating of TRPA1 has not been previously described, and we show that it occurs less frequently in HEK cells expressing TRPA1, suggesting that formation of binary structures is not an inherent property of the channel but may be mediated by adaptor or scaffolding proteins selectively expressed by the endothelium. It is possible that TRPA1 channels could also couple with Ca^{2+}-sensitive channels, such as TRPV4, but we see no evidence of such

an arrangement in cerebral artery endothelial cells in our TRPA1 sparklet data. Our data also showed that only a few (~4–8) TRPA1 sparklet sites are active per cell under conditions sufficient to induce maximal dilation of cerebral arteries. These findings support a scheme in which large amounts of Ca^{2+} entering the cell during individual TRPA1 sparklet events is sufficient to allow these few active sites to generate very high local Ca^{2+} concentration in subcellular domains, particularly within the confined space of myoendothelial projections where TRPA1 and IK channels are present (*6*). We propose that local elevations in Ca^{2+} created by TRPA1 sparklets activate nearby IK channels in myoendothelial projections, either directly or indirectly through Ca^{2+}-induced Ca^{2+} release from inositol trisphosphate receptors (*28*). The resulting efflux of K^+ hyperpolarizes the endothelial cell membrane, and the electrotonic spread of this influence through myoendothelial gap junctions subsequently hyperpolarizes the underlying smooth muscle to cause vasodilation (Figure 3.13F) (*20, 163*).

ROS are involved in the control of cerebral endothelial cell function, vascular reactivity, and blood flow. NOX is a major ROS generator in the cerebral circulation (*164, 165*), and NOX expression and basal O_2^- production are up to 120-fold higher in cerebral arteries relative to the aorta and carotid, mesenteric, and renal arteries (*142*). Our data demonstrated that ROS generated by NOX stimulates TRPA1 activity in the cerebral endothelium. We also showed that NOX2 co-localizes with TRPA1 and that NOX-induced TRPA1 activation and vasodilation are blocked by the gp91ds-tat peptide, thought to be a specific inhibitor of NOX2 (*158*). These data provide evidence that generation of ROS by NOX2 increases TRPA1 activity in the cerebral artery endothelium. Our findings also indicate that NOX-derived O_2^- does not directly activate

TRPA1 in the endothelium, but requires the generation of H_2O_2 and OH• intermediates. Immunolabeling studies presented here indicated that NOX2, TRPA1, and that 4-HNE-modified proteins are abundant within IEL fenestrations. This arrangement suggests that localized generation of lipid peroxidation products within myoendothelial projections activates TRPA1 sparklets to elicit vasodilation, a concept supported by our data showing that 4-HNE increased TRPA1 sparklet activity in endothelial cells and dilated cerebral arteries. Taken together, these findings provide support for a signaling cascade in which O_2^- generated by NOX2 is converted to H_2O_2 and then to OH•, leading to peroxidation of membrane lipids. The resulting metabolites activate TRPA1 channels in the endothelium. Ca^{2+} influx through TRPA1 channels activates IK channels to hyperpolarize the endothelial and smooth muscle cell plasma membrane, resulting in arterial dilation (Figure 3.13F).

Collectively, our data demonstrate that TRPA1 channels are central to a ROS-sensing signaling pathway unique to the cerebral circulation that causes endothelium-dependent vasodilation. The effects of NOX-derived ROS were investigated here, but it is also possible that other source of ROS, such as mitochondrial respiration could influence TRPA1 activity. NOX activity and ROS production are increased in cerebral arteries during hypertension and other pathological conditions (*166*), suggesting that TRPA1 channels and the pathway we described here may provide some protection against cerebrovascular disease.

Table 3.1: TRPA1 Sparklet Properties. Mode, mean, and range for amplitude, duration, attack time, decay time, and spatial spread of TRPA1 sparklets recorded from HEK 293 cells overexpressing TRPA1-GFP (n = 792 events) or rat primary cerebral artery endothelial cells (n = 762 events).

	HEK + TRPA1-GFP			Endothelial Cells		
	Mode	**Mean ± SE**	**Range**	**Mode**	**Mean ± SE**	**Range**
Amplitude (F/F_0)	1.14	1.21 ± 0.004	1.06 – 1.77	1.26	1.25 ± 0.004	1.06 – 2.06
Duration (s)	0.05	0.46 ± 0.02	0.05 – 5.51	0.06	0.96 ± 0.04	0.04 – 5.05
Attack Time (ms)	0.03	0.22 ± 0.01	0.02 – 3.78	0.03	0.46 ± 0.02	0.02 – 3.56
Decay Time (ms)	0.03	0.24 ± 0.01	0.02 – 3.30	0.03	0.50 ± 0.02	0.02 – 3.84
Spatial Spread (μm^2)	0.72	2.44 ± 0.14	0.72 – 34.51	0.72	5.02 ± 0.60	0.72 – 290.0

Table 3.2: Vascular Characteristics of Control and eTRPA1$^{-/-}$ Mouse Cerebral Arteries. Maximum constriction to superfusion of 60 mM KCl physiological saline solution, % myogenic tone at 60 mmHg intraluminal pressure, and the maximum diameter at 60 mmHg intraluminal pressure for control (n = 6) and eTRPA1$^{-/-}$ (n = 5) mouse cerebral arteries.

	Peak Constriction	**Myogenic Tone**	**Maximum Diameter**
Control	59.3 ± 7.0 %	18.3 ± 2.2 %	103.0 ± 5.4 μm
eTRPA1$^{-/-}$	68.6 ± 3.5 %	17.2± 1.4 %	100.0 ± 3.3 μm

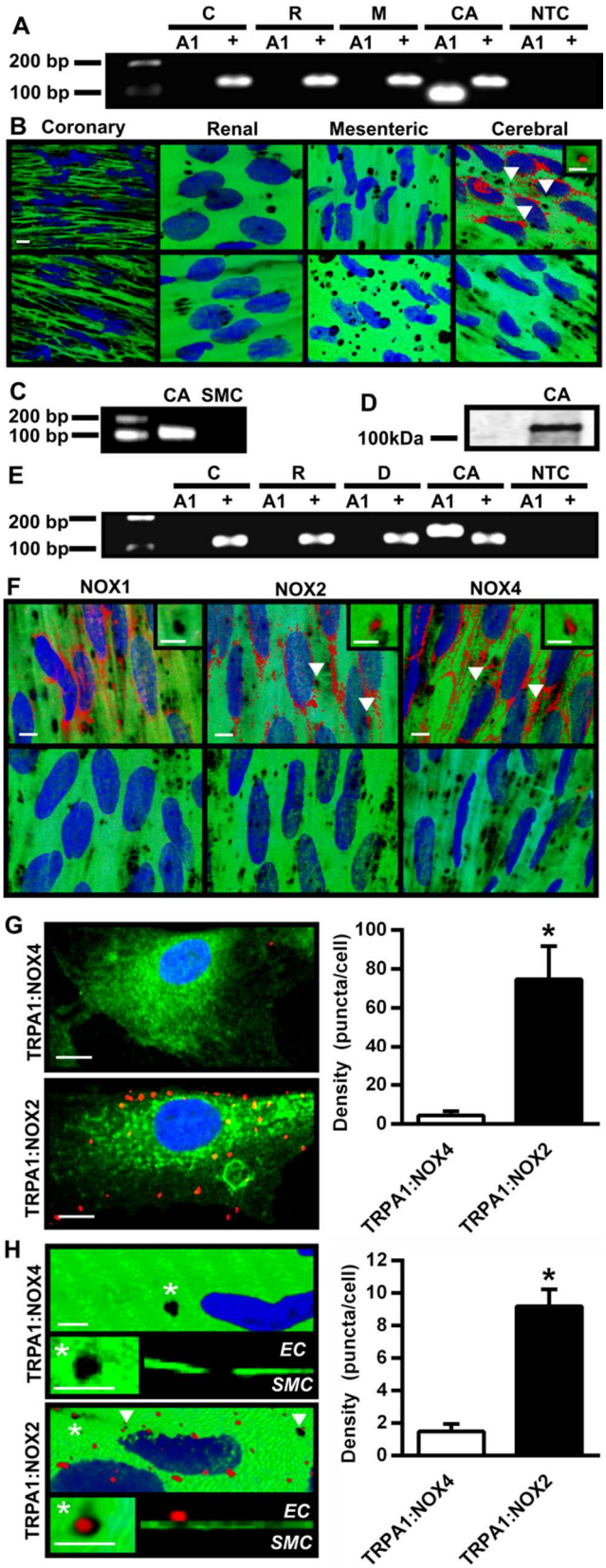
A
C
R
M
CA
NTC
A1
+
200 bp
100 bp
B
Coronary
Renal
Mesenteric
Cerebral
C
CA SMC
200 bp
100 bp
D
CA
100kDa
E
C
R
D
CA
NTC
A1
+
200 bp
100 bp
F
NOX1
NOX2
NOX4
G
TRPA1:NOX4
TRPA1:NOX2
Density (puncta/cell)
100
80
60
40
20
0
*
TRPA1:NOX4
TRPA1:NOX2
H
TRPA1:NOX4
TRPA1:NOX2
EC
SMC
Density (puncta/cell)
12
10
8
6
4
2
0
*
TRPA1:NOX4
TRPA1:NOX2

Figure 3.1: TRPA1 co-localizes with NOX2 in the endothelium of cerebral arteries but not in other vascular beds. (A) RT-PCR for TRPA1 (A1) and eNOS (+) in rat coronary (C), renal (R), mesenteric (M), and cerebral (CA) arteries. NTC = No cDNA template control (n = 2). **(B)** *Top:* Immunolabeling for TRPA1 in coronary, renal, mesenteric, and cerebral arteries; scale bar = 10 μm. Autofluorescence of the IEL is green. TRPA1 protein (red) was detected in within myoendothelial projections (arrows, inset; scale bar = 5 μm). *Bottom:* No primary antibody control (n = 3). **(C)** RT-PCR for TRPA1 in whole human cerebral arteries (CA) and smooth muscle cells isolated from human cerebral arteries (SMC) (n = 3). **(D)** Western blot for TRPA1 in human cerebral arteries (CA) (n = 2). **(E)** RT-PCR detection of human TRPA1 (A1) and eNOS (+) in primary coronary (C), renal (R), dermal (D), and cerebral artery (CA) endothelial cells (n = 3). NTC = No cDNA template control. **(F)** *Top:* Cerebral arteries immunolabeled for NOX1 (left), NOX2 (middle), or NOX4 (right) (red); scale bar = 10 μm. Insets: Magnified myoendothelial projections (arrows, bar = 5 μm). Endothelial cell nuclei (blue) and the IEL (green) are shown. *Bottom:* No primary antibody control (n = 3). **(G)** PLA for TRPA1:NOX4 (top) and TRPA1:NOX2 (bottom) in cerebral artery endothelial cells. Puncta corresponding to a positive PLA results are red, autofluorescence is green, and nuclei are blue. Puncta density is summarized at the right (n = 4 cells/group); *P ≤ 0.05 versus TRPA1:NOX4. **(H)** PLA for TRPA1:NOX4 (top) and TRPA1:NOX2 (bottom). TRPA1:NOX2 puncta within IEL fenestrations are indicated by arrows. (*) is an example magnified and shown in cross-section in the insets. Puncta density is summarized at the right (n = 8-14 vessels/group); *P ≤ 0.05 versus TRPA1:NOX4.

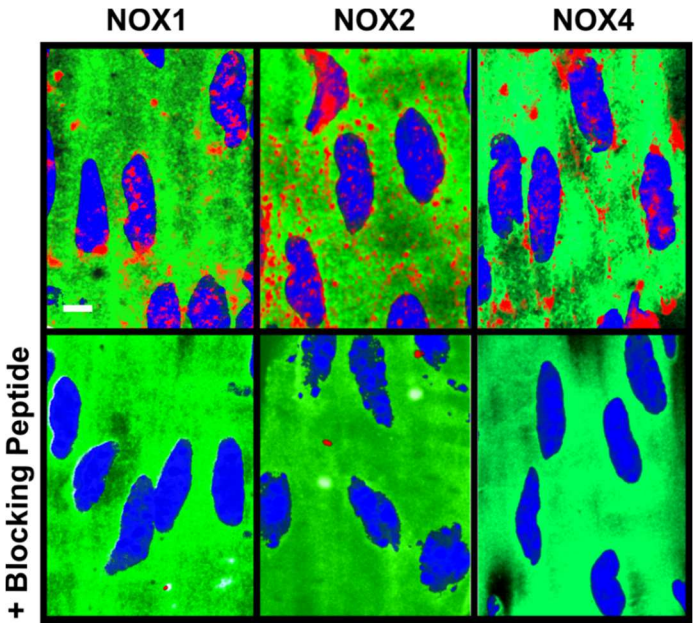

Figure 3.2: NOX Antibody Specificity. Top: Intact endothelium immunolabeled for NOX1, NOX2, or NOX4 (red). Autofluorescence of the internal elastic lamina is green and DAPI-stained endothelial cell nuclei are shown in blue. Bottom: Antibodies were pre-incubated with their respective antigenic blocking peptides before use in immunohistochemistry (n = 3 animals/group). Scale bar = 10 μm.

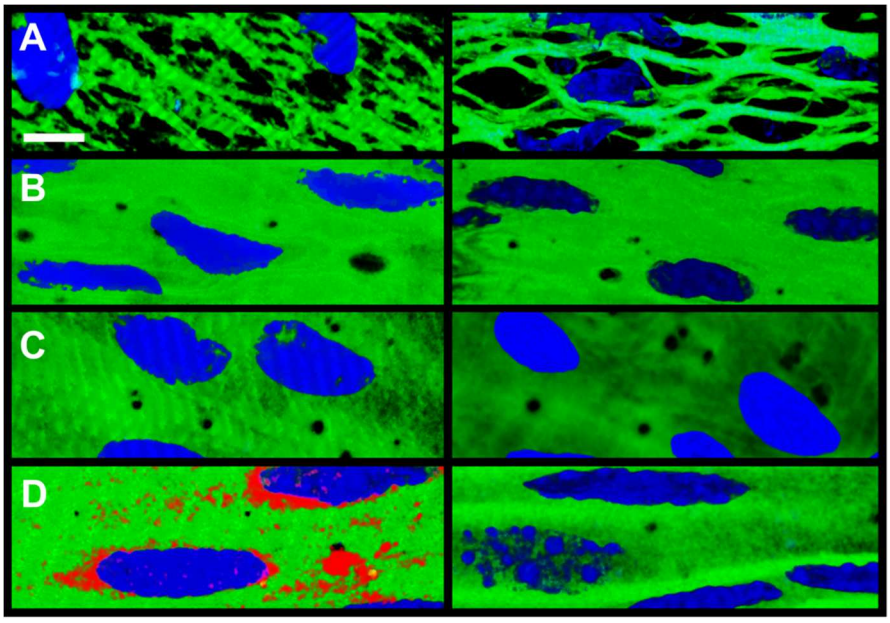

Figure 3.3: TRPA1 in Mouse Arteries. A-D: TRPA1 immunolabeling (red) in intact endothelial cells of *en face* mouse coronary septal (A), renal interlobar (B), 3rd order mesenteric (C), and cerebral (D) arteries. Internal elastic lamina autofluorescence (green) and endothelial cell nuclei (blue) are shown; scale bar = 10 μm (n = 3 mice).

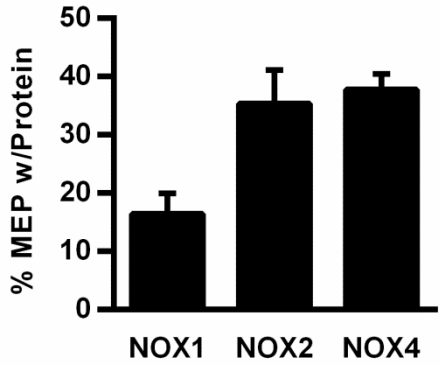

Figure 3.4: NADPH Oxidase Proteins Are Present in Myoendothelial Projections. Summary graph indication the percentage of myoendothelial projections (MEP) that contain NADPH oxidase (NOX) isoforms 1, 2, or 4. NOX1 immunolabeling was present in 16.4 ± 3.5% of internal elastic lamina fenestrations. NOX2 and NOX4 were detected within 35.4 ± 5.7% and 37.8 ± 2.6% of projections, respectively (n = 6-18 vessels/group, 3 rats).

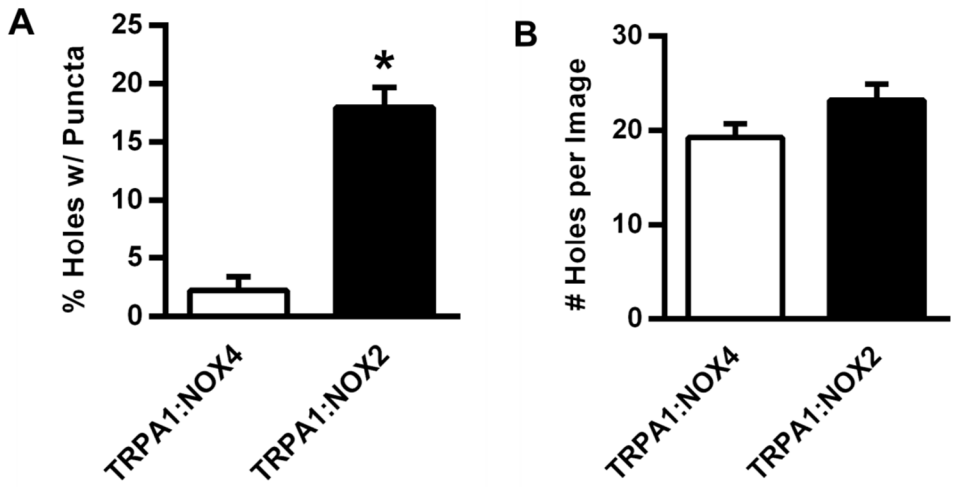

Figure 3.5: TRPA1 and NOX2 Co-Localize Near IEL Fenestrations. A: There are a greater number of PLA co-localization puncta for TRPA1:NOX2 than TRPA1:NOX4 that are within or near IEL fenestrations (holes) (n = 8-14 vessels/group, 3 rats); *P ≤ 0.05 vs. TRPA1:NOX4. B: The total number of IEL fenestrations per each image analyzed did not differ between PLA experiments for TRPA1:NOX4 and TRPA1:NOX2 (n = 8-14 vessels/group, 3 rats).

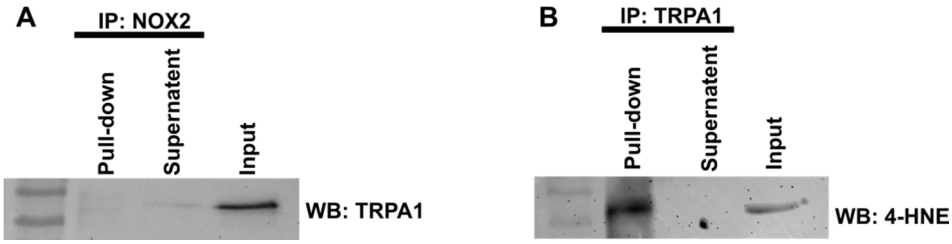

Figure 3.6: TRPA1 is 4-HNE-modified but Does Not Physically Interact with NOX2. A: Co-immunoprecipitation for NOX2 and TRPA1. The pull-down product and supernatant are indicated. The input sample was used as a positive control (n = 3 mice, 3 independent experiments). B: Immunoprecipitation for TRPA1 immunoblotted for 4-HNE-modified proteins. The pull-down product and supernatant are indicated. The input sample was used as a positive control (n = 3 mice, 3 independent experiments).

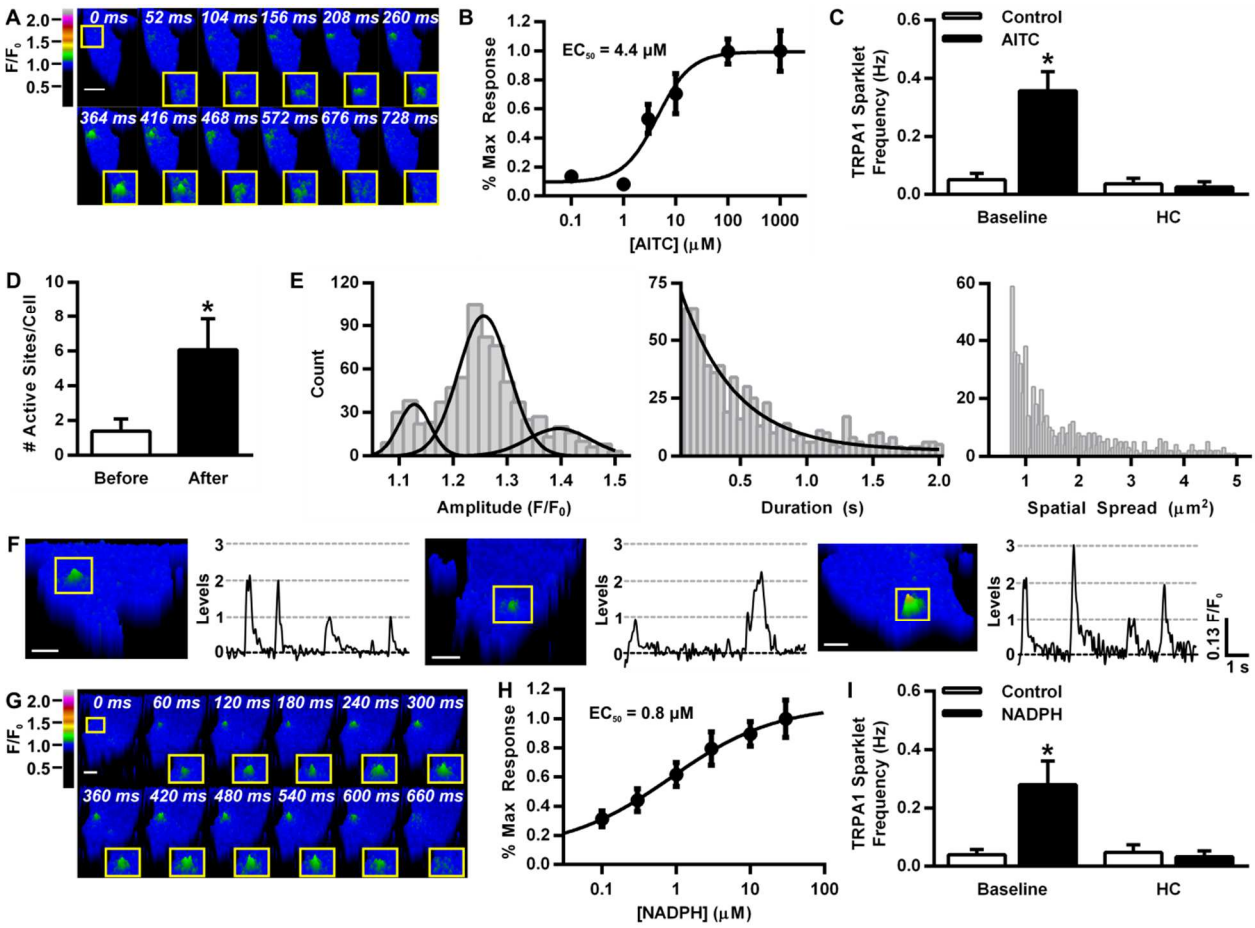

Figure 3.7: ROS stimulate TRPA1 sparklets in cerebral artery endothelial cells. (A) Time-lapse image of an AITC-induced TRPA1 sparklet recorded from a cerebral artery endothelial cell; scale bar = 8 μm. (B) AITC induces a concentration-dependent increase in TRPA1 sparklet frequency in cerebral artery endothelial cells (n = 5–52 cells/concentration, 4 independent cell isolations). (C) Summary data showing that HC-030031 inhibits AITC-induced increases in TRPA1 sparklet frequency in cerebral artery endothelial cells (n = 10–24 cells, 3 independent cell isolations); *P ≤ 0.05 versus control at baseline. (D) Active TRPA1 sparklet sites per cell before and after administration of AITC (n = 10 cells, 5 rats). (E) Amplitude (left), duration (middle), and spatial spread (right) histograms for TRPA1 sparklets (n = 762 total events, 43 independent experiments). (F) Representative recordings of change in fluorescence (F/F_0) within a region of interest on primary cerebral artery endothelial cells stimulated by AITC. Dotted lines indicate the opening of 1, 2, or 3 TRPA1 channels. (G) Time-lapse image of a TRPA1 sparklet stimulated by NADPH; scale bar = 8 μm. (H) The NOX substrate NADPH induced a concentration-dependent increase in TRPA1 sparklet frequency (n = 9–22 cells/concentration, 4 independent cell isolations). (I) Summary data indicating that HC-030031 inhibits NADPH-induced increases in TRPA1 sparklet frequency (n = 12–28 cells/group, 3 independent cell isolations); *P ≤ 0.05 versus baseline, control.

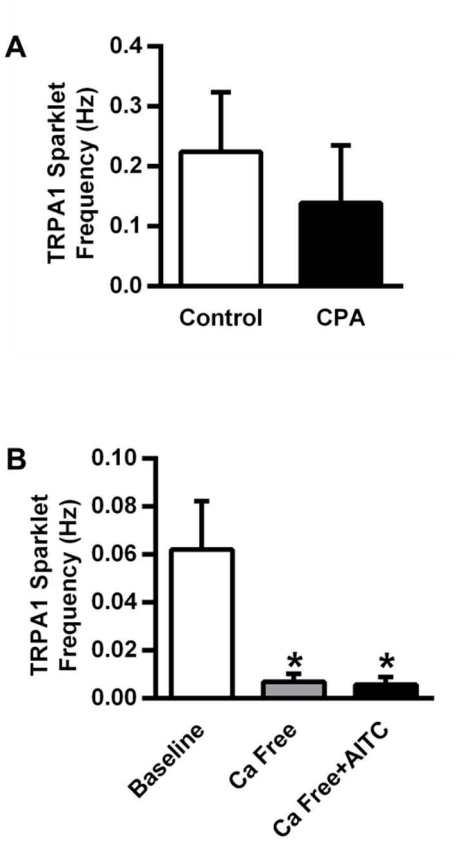

Figure 3.8: AITC Stimulates Ca^{2+} Influx in Endothelial Cells. A: Depletion of intracellular stores with cyclopiazonic acid (CPA, 10 μM) treatment has no effect on basal TRPA1 sparklets in primary cerebral artery endothelial cells (n = 20-21 cells/group, 3 independent cell isolations). B: Summary data indicating abolished basal and AITC (100 μM)-induced endothelial cell TRPA1 sparklets in the absence of extracellular Ca^{2+} (n = 19 cells/group, 4 independent cell isolations); *P ≤ 0.05 vs. control.

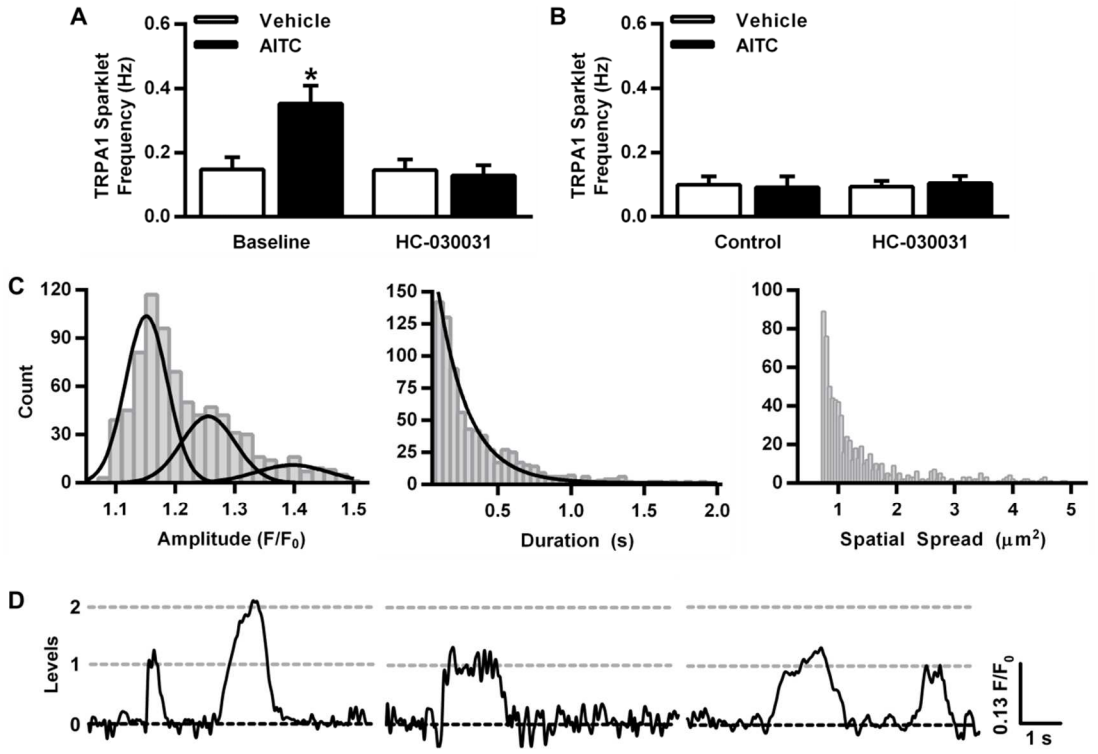

Figure 3.9: TRPA1 Sparklets in TRPA1-GFP-transfected HEK 293 Cells. A: Summary data indicating an increase in HEK + TRPA1-GFP + RFP cell TRPA1 sparklet frequency in the presence of AITC (100 μM) that is inhibited by HC-030031 (10 μM) (n = 19-43 cells/group, 4 independent experiments); *P ≤ 0.05 vs. control, baseline. B: Summary data demonstrating that AITC (100 μM) has no effect on basal Ca^{2+} channel activity of HEK cells transfected with only RFP (n = 24-28 cells/group, 4 independent experiments). C: Histograms of TRPA1 sparklet amplitude (left), duration (middle), and spatial spread (right) recorded from HEK 293 + TRPA1-GFP + RFP cells. The amplitude histogram displays one prominent peak (F/F_0 = 0.13). D:

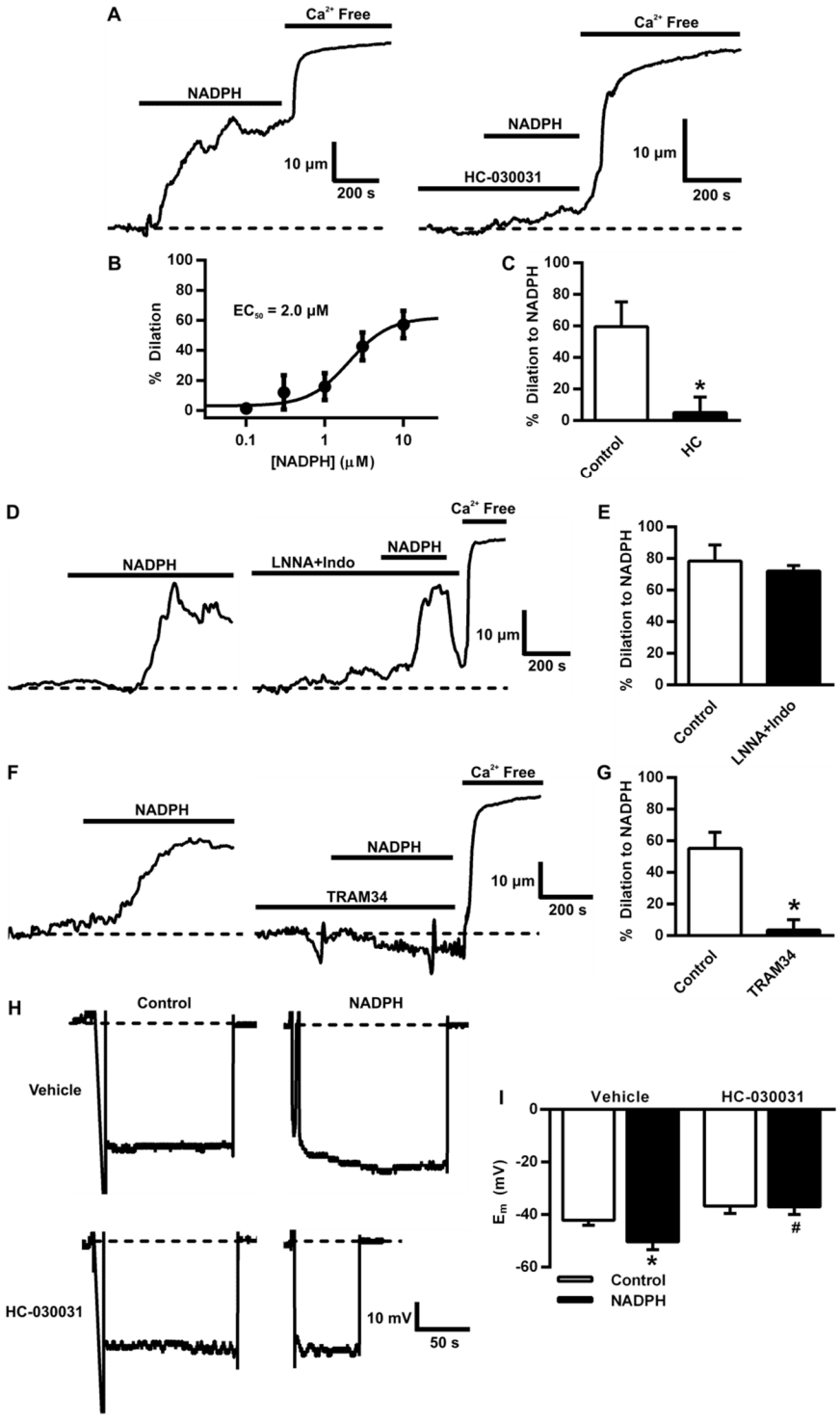
A
Ca2+ Free
NADPH
10 µm
200 s
HC-030031
B
EC50 = 2.0 µM
% Dilation
[NADPH] (µM)
C
% Dilation to NADPH
Control
HC
D
LNNA+Indo
E
F
TRAM34
G
H
Control
NADPH
Vehicle
HC-030031
10 mV
50 s
I
Vehicle
HC-030031
Em (mV)
Control
NADPH

Figure 3.10: ROS generated by NOX dilate cerebral arteries by activating TRPA1. (A) Representative recordings of the intraluminal diameter of an intact, pressurized cerebral artery over time. Introduction of NADPH to the bathing solution induced vasodilation that was nearly abolished by the TRPA1 blocker HC-030031. (B) NADPH-induced vasodilation is concentration-dependent (n = 3 vessels/concentration, 3 rats). (C) Summary data indicating NADPH-induced dilation is attenuated by HC-030031 (n = 5 vessels, 3 rats); *P ≤ 0.05 versus control. (D) Representative recordings and summary data (E) indicating that the nitric oxide synthase inhibitor L-NNA and the cyclooxygenase inhibitor indomethacin have no effect on NADPH-induced vasodilation (n = 3 vessels, 3 rats). (F) Representative recordings and summary data (G) showing that NADPH-induced vasodilation (left) is inhibited when the intermediate conductance Ca^{2+}-activated K^+ channel blocker TRAM34 is present in the lumen (right) (n = 5 vessels, 3 rats); *P ≤ 0.05 versus control. (H) Representative recordings of smooth muscle cell membrane potential (E_m) in a pressurized cerebral artery. Smooth muscle cells were hyperpolarized by NADPH. NADPH-induced hyperpolarization was blocked by HC-030031. (I) Summary data (n = 4 vessels, 4 rats); *P ≤ 0.05 versus vehicle, control; #P ≤ 0.05 versus vehicle, NADPH.

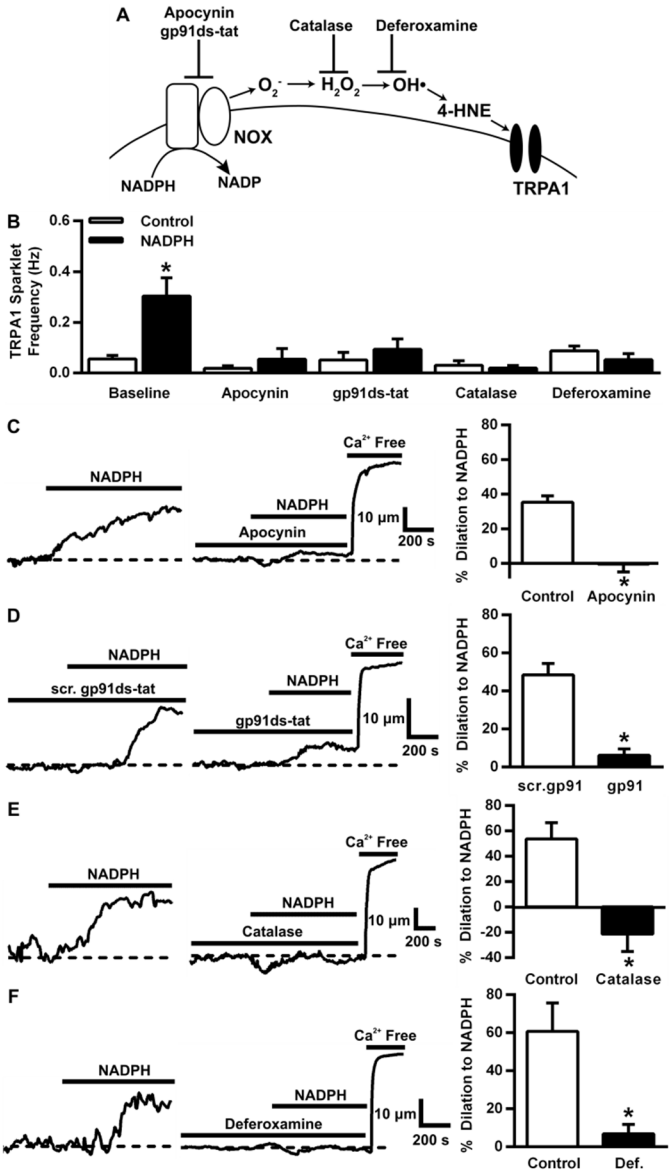

Figure 3.11: ROS-derived lipid peroxidation metabolites stimulate TRPA1 sparklets and dilate cerebral arteries. (A) Proposed pathway and pharmacological interventions for activation of TRPA1 by NOX-generated ROS metabolites. (B) NADPH-induced increases in TRPA1 sparklet frequency in endothelial cells at baseline (n = 27-60 cells/group, 5 independent cell isolations) were attenuated by inhibition of NOX with apocynin (n = 8–10 cells/group, 3 independent cell isolations) and gp91ds-tat (n = 7–9 cells/group, 3 independent cell isolations) compared to vehicle and a scrambled peptide (scr. gp91ds-tat), respectively, H_2O_2 degradation with extracellular catalase (n = 9–11 cells/group, 3 independent cell isolations), and iron chelation with deferoxamine (n = 8–12 cells/group, 3 independent cell isolations); *P ≤ 0.05 versus baseline, control. Representative traces and summary data indicating inhibition of NADPH-induced vasodilation by apocynin (n = 5 vessels, 3 rats) (C), gp91ds-tat (n = 5 vessels, 3 rats) (D), catalase (n = 5 vessels, 3 rats) (E), and deferoxamine (n = 5 vessels, 3 rats) (F); *P ≤ 0.05 versus vehicle control or scr. gp91ds-tat.

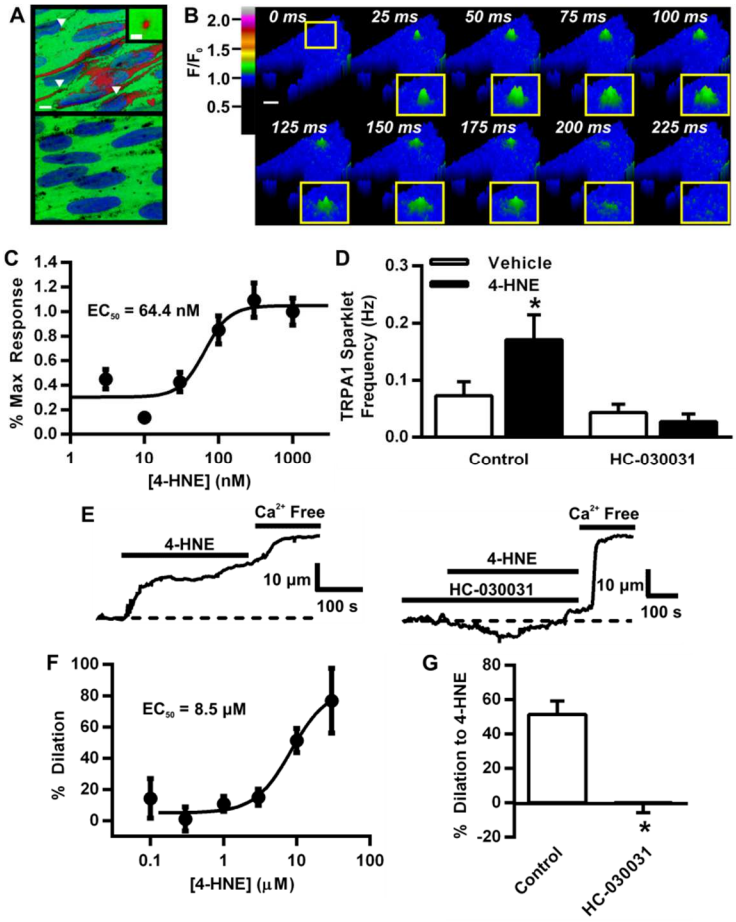

Figure 3.12: Lipid peroxidation products activate TRPA1 sparklets in endothelial cells and dilate cerebral arteries. A) Cerebral artery mounted *en face* and immunolabeled for 4-HNE-modified proteins (red, top). 4-HNE labeling was present in perinuclear regions and within IEL fenestrations (arrows, inset; scale bar = 5 µm). Immunolabeling was not detected in the absence of primary antibody (bottom); scale bar = 10 µm. Endothelial cell nuclei are stained with DAPI (blue) and autofluorescence of the IEL is green (n = 3 rats). (B) Time-lapse image of a 4-HNE-induced TRPA1 sparklet; scale bar = 8 µm. (C) 4-HNE-induced increases in TRPA1 sparklet frequency are concentration-dependent (n = 9-11 cells/concentration, 3 rats). (D) 4-HNE-induced increases in TRPA1 sparklet frequency are abolished by the TRPA1 blocker HC-030031 (n = 19–31 cells, 4 rats); *P ≤ 0.05 versus baseline, control. (E) Representative recording of 4-HNE-induced vasodilation of a pressurized cerebral artery. 4-HNE-induced dilation (left) was inhibited by HC-030031 (right). (F) Concentration response curve for 4-HNE-induced dilation in cerebral arteries (n = 3–5 vessels/group, 5 rats). (G) Summary data indicating that 4-HNE-induced dilation is abolished by HC-030031 (n = 5 vessels, 4 rats); *P ≤ 0.05 versus control.

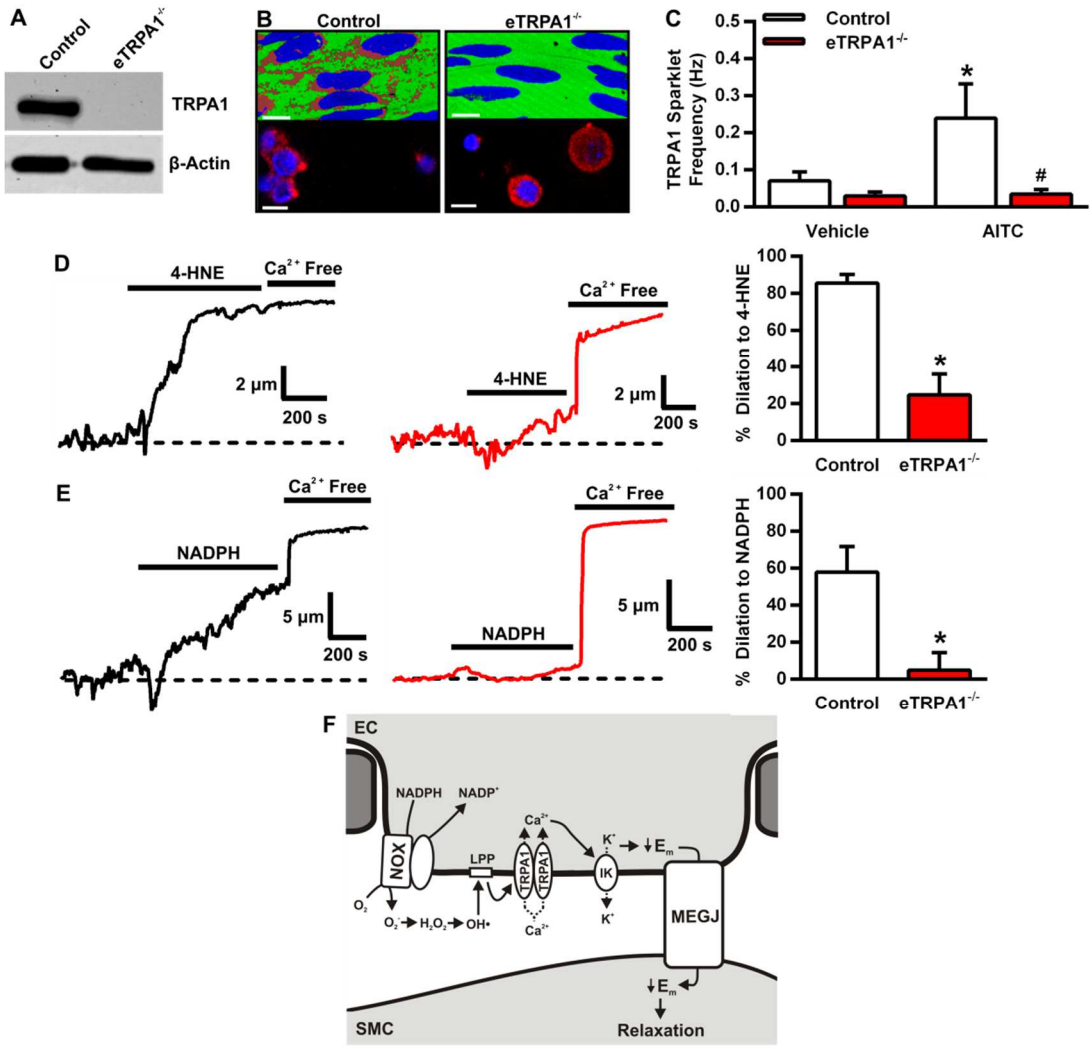

Figure 3.13: ROS-derived lipid peroxidation products fail to dilate cerebral arteries from endothelial cell-specific TRPA1-knockout mice. (A) Western blot for TRPA1 protein (138 kDa) in cerebral arteries from control and eTRPA1$^{-/-}$ mice (n = 3 mice per group). (B) TRPA1 immunolabeling in the cerebral endothelium (top) and DRG neurons (bottom) from control and eTRPA1$^{-/-}$ mice (n = 3 mice/group). (C) Summary data indicating the effect of AITC on the frequency of sparklets recorded from endothelial cells isolated from control compared with eTRPA1$^{-/-}$ mice (n = 20 cells/group, 3 independent cell isolations/group). (D) 4-HNE and NADPH (D) dilate cerebral arteries from control but not eTRPA1$^{-/-}$ mice (n = 5 vessels/group, 3 mice/group); *P ≤ 0.05 versus control. (F) Proposed signaling pathway: In endothelial cells (EC), NOX generates O_2^-, which is rapidly dismutated to H_2O_2. In the presence of iron, H_2O_2 undergoes the Fenton reaction to yield OH•. Oxidation of membrane lipids by OH• generates lipid peroxidation products (LPP), which activate TRPA1 sparklets through binary-coupled TRPA1 channels. Ca^{2+} domains created by TRPA1 sparklets stimulate outward K^+ currents through IK channels to hyperpolarize the EC plasma membrane (E_m). Electrotonic spread of EC hyperpolarization through myoendothelial gap junctions (MEGJ) causes smooth muscle cell (SMC) hyperpolarization and vasodilation.

CHAPTER 4

Significance of TRPA1 Channels in the Cerebral Artery Endothelium during the Onset of Hypertension-Associated Spontaneous Hemorrhagic Stroke

INTRODUCTION

Hypertension is a major risk factor contributing to the development of severe cerebrovascular injury such as stroke. There are two main types of stroke, which include ischemic and hemorrhagic. The blockage of a cerebral vessel that reduces blood flow to downstream tissue is known as an ischemic stroke, while a hemorrhagic stroke is the bursting of a cerebral vessel and bleeding into the brain. A transient blockage of blood flow is referred to as a transient ischemic attack, or TIA, which is often called a “mini-stroke”, as blood flow is not completely blocked. Stroke is the fourth leading cause of death in the U.S. and is responsible for ~10% of deaths worldwide (*167, 168*). Most strokes (>87%), including ischemic and hemorrhagic, occur within arteries due to localized disruption of cerebral blood flow (*168*). During hypertension, vascular production of reactive oxygen species (ROS) and oxidative degradation of membrane lipids within the vascular wall are elevated (*148, 164*). Sources of ROS in endothelial cells include mitochondria, cyclooxygenase, uncoupled nitric oxide synthase (NOS), and NADPH-oxidase (NOX). Prior work indicates that NOX expression and activity are up to 120-fold higher in cerebral vs. systemic arteries, and activation of NOX induces vasodilation (*142*).

Our previous work indicates that NOX-dependent vasodilation of cerebral arteries is mediated by transient receptor potential ankyrin 1 (TRPA1) channels (Sullivan MN, et

al. 2014, in review). TRPA1 expression in endothelial cells is restricted to cerebral arteries, suggesting a specialized, yet unknown function for the cation channel in this tissue (Sullivan MN et al. 2014, in review). TRPA1 channels are sensitive to oxidized membrane lipids produced by ROS generation (*145, 148*) (Sullivan MN et al. 2014, in review), hallmarks of cerebrovascular disease. However, a pathological significance for TRPA1 in the cerebral vasculature has never been explored.

In this study we examine the involvement of TRPA1 channels in the endothelium of cerebral arteries during hypertension and hypertension-associated cerebrovascular disease. In addition, we describe a new model of hypertension-associated spontaneous hemorrhagic stroke in mice. We find that although TRPA1 mRNA and protein are unchanged, TRPA1 activity is increased following hypertension induction. Furthermore, using our endothelial cell-specific TRPA1 knockout (eTRPA1$^{-/-}$) mice, we provide the first evidence that lack of endothelial cell TRPA1 channels decreases the latency to clinical signs of stroke and increases the number of intracerebral hemorrhage lesions in the brain compared with control mice. While, the size of intracerebral hemorrhage lesions was smaller. Together these findings suggest that endothelial TRPA1 channel activity protects the cerebral vasculature during vascular disease and functions to delay the onset of stroke.

MATERIALS AND METHODS

Mice

Male and female mice homozygous for loxP sequences flanking the S5/S6 transmembrane domains of TRPA1 ("floxed TRPA1," B6.129S-TRPA1^{tm2KyKw}/J) were

used as control mice. Male and female floxed mice with hemizygous expression of *cre recombinase* (*cre*) driven by the promoter for the endothelial cell-specific receptor tyrosine kinase *TEK* (B6.Cg-Tg(*TEK-cre*)1Ywa/J) are endothelial cell-specific TRPA1 knockout (eTRPA1$^{-/-}$) mice. Mice homozygous for floxed TRPA1 and positive for *cre* were bred with homozygous floxed TRPA1 mice to generate control (homozygous floxed TRPA1) and eTRPA1$^{-/-}$ (homozygous floxed TRPA1, *cre* positive) littermates. Mice were kept on a 12 hr light/dark cycle with temperature and humidity control. Mice were fed standard chow and regular water *ad libitum* until initiation of experimental diet.

Radiotelemetry Transmitter Probe Implantation

At 12 weeks of age, mice underwent telemetry probe implantation as previously described (*169, 170*). Briefly, anesthesia is induced by 3% isofluorane and maintained by 1.5% isofluorane. A 1 cm incision is made between the chin and the sternum. A subcutaneous pocket under the right forelimb was made to implant the body of telemetry probe. The left common carotid artery is isolated and a distal ligature is placed. A loop is made to suspend the proximal portion of the carotid artery in order to stop the flow of blood. A small incision in the artery is made, and the catheter of the radiotelemetry probe is then inserted into the carotid artery. The artery containing the catheter is secured, and the transmitter body is inserted into the pocket made under the right forelimb and pushed down to the abdominal area under the skin. Mice were given post-operative analgesia (buprenorphine 0.1 mg/kg) and allowed two weeks of recovery. Baseline recordings are taken for one week after the mouse is fully recovered (14 weeks old).

Hypertension-associated spontaneous stroke model

At 15 wks of age, mice were implanted with a mini osmotic pump filled with Angiotensin II (Ang II, 1200 ng/kg/min). Mice were also given an 8% NaCl (High salt, HS) chow *ad libitum*. After two weeks of Ang II/HS treatment, mice were given L-NAME-supplemented water (120 mg/kg/day) to induce spontaneous hemorrhagic stroke in mice.

Real-Time RT-PCR

Cerebral and cerebellar arteries from 3 animals were isolated and pooled together for each control untreated and Ang II/HS/L-NAME treated mice. RNA was extracted and purified using an RNeasy mini kit (Qiagen). A reverse transcriptase reaction was performed using 200 ng RNA per group with a QuantiTect RT kit (Qiagen) to generate complimentary DNA (cDNA) samples. Quantitative PCR was performed using a QuantiTect SYBR Green kit (Qiagen), mouse TRPA1 primers (Qiagen), and mouse GAPDH primers (IDT) to determine TRPA1 mRNA levels in untreated and Ang II/HS/L-NAME treated mouse cerebral artery samples relative to GAPDH levels. The relative expression levels were calculated using the Pfaffl method (*171*) as previously described (*172*).

Western Blotting

Cerebral and cerebellar arteries from each mouse were isolated and snap frozen in liquid nitrogen. 50 µL RIPA lysis buffer (Pierce) containing a protease inhibitor

cocktail (Calbiochem) was added to each artery sample and homogenized by sonication (20 x 2 sec pulses) and mechanical disruption by a Fisher Scientific Tissuemiser (10 sec) on ice. Samples were then centrifuged at 13,000 rpm for 10 min, and the supernatant was transferred to a new tube. Protein concentration for each sample was determined using a BCA Protein assay (Pierce). 10 ng of each protein sample was added to SDS sample buffer and heated at 70°C for 10 min. Immediately following denaturation, proteins were separated by SDS-PAGE and then transferred to a nitrocellulose membrane. Membranes were blocked with 5% milk, 1% BSA in PBS containing 0.1% Tween and 0.02% sodium azide (PBS-TA) for 30 min at room temperature on a rocker and then exposed to a rabbit anti-TRPA1 antibody (1:500, Alomone Labs) in 5% milk, 1% BSA (PBS-TA) overnight at room temperature on a rocker. The membrane was then washed with PBS-T 3 x 5 min and exposed to a goat anti-rabbit secondary antibody (1:10,000, Invitrogen) in 5% milk, 1% BSA (PBS-T) for 2 hours at room temperature on a rocker. The membrane was then washed 5 x 5 min with PBS-T, incubated in Supersignal ECL substrate (Pierce) for 1-3 min, and imaged. Protein amount was quantified using ImageJ software.

Isolated Vessel Experiments

Isolated vessel experiments with mouse cerebral arteries were performed as previously described (Sullivan et al 2014, in review). Briefly, mouse cerebral and cerebellar arteries were isolated and placed in ice cold MOPS-buffered saline. Arterial segments were then cannulated between two glass micropipets in a chamber (Living Systems Instrumentation) and secured with single-filament silk. Arteries were

superfused with a physiological saline solution (PSS) warmed to 37°C and bubbled with 21% O_2, 6% CO_2, and balanced N_2. Vessels were pressurized to 60 mmHg, gently stretched to simulate physiological conditions, and brought back down to 20 mmHg intraluminal pressure to equilibrate for 15 min. Arterial viability was tested by superfusing a high K^+ PSS and then was allowed to equilibrate for an additional 15 min. The intraluminal pressure was increased to 60 mmHg and the artery was allowed to develop spontaneous myogenic tone. AITC or NADPH were then added to the bathing solution. At the end of each experiment, vessels were superfused with a Ca^{2+}-free PSS to obtain the passive diameter of each artery. The % dilation to each agonist was calculated as the % change in myogenic tone before and after addition of the agonist.

Histology

Brains were removed from the mouse and drop-fixed in 7% formaldehyde (PBS) at 4°C for 5 days. Brains were then dehydrated in 20% sucrose (PBS) overnight at 4°C and frozen in OCT at -80°C. The tissue was then sectioned with a cryostat, generating 25 µm thick sections collected every 100 µm. Sections were fixed to slides with 4% formaldehyde (PBS) for 10 min, rinsed in PBS, and then stained with diaminobenzidine for 5 min using a DAB substrate kit (Vector Laboratories). Slides were then rinsed in PBS and submersed in filtered Harris Hematoxylin for 30 sec, rinsed with tap water, and submersed in 2% eosin for 30 sec. After rinsing in tap water, sections were then dehydrated with a series of alcohol solutions for 1 min each (30%, 50%, 70%, 80%, 90% (x2), 100% (x2)) and then placed in xylene for 2 x 1 min. Mounting medium and a coverslip were then added to each slide and the mounting medium was allowed to dry

for at least one day. Sections were imaged using a light microscope with an attached camera.

Intracerebral Hemorrhage Lesion Count and Volume Quantification

Intracerebral hemorrhage (ICH) lesions were identified as an abnormal appearance of blood within the brain tissue. The number of ICH lesions was quantified per each generalized brain region: cerebral cortex (CC), basal ganglia (BG), midbrain (MB), brainstem (BS), or cerebellum (CB). ICH lesion area (μm^2) was determined using ImageJ software. The area of each lesion was then multiplied by 25 μm^2 to estimate lesion volume. The total lesion volume was calculated by summing the volume of a lesion per section that the same lesion appeared. Lesion count and volume per each brain region were determined for each experimental group: control mice untreated, control mice treated with Ang II/HS-L-NAME, eTRPA1$^{-/-}$ mice untreated, and eTRPA1$^{-/-}$ mice treated with Ang II/HS-L-NAME.

RESULTS

Cardiovascular Parameters: Control Mice

Baseline mean arterial pressure (MAP) (102.3 ± 1.2 mmHg) and heart rate (498.1 ± 6.7 bpm) were recorded for control mice (n = 8 mice) (Figure 4.1 A and B). One day following initiation of treatment with angiotensin II (Ang II) and a high salt (8%) chow, blood pressure increased and was sustained throughout the two week treatment (mean MAP = 126.0 ± 2.0 mmHg) (Figure 4.1 A and B). After two weeks, L-NAME was

introduced into the drinking water, which led to a further increase in MAP to 152.7 ± 2.5 mmHg that was maintained for the rest of the experiment (Figure 4.1 A and B).

The heart to body mass ratio increased following treatment with Ang II/HS/L-NAME (0.004 ± 0.0001 (untreated) vs. 0.007 ± 0.0004 (treated); n = 18 per group), indicating that the treatment induced cardiac hypertrophy relative to normotensive controls (Figure 4.1C). The left ventricle to whole heart mass ratio also increased following treatment with Ang II/HS/L-NAME (0.391 ± 0.012 (untreated) vs. 0.465 ± 0.010 (treated); n = 18 per group) (Figure 4.1D) which indicates that the hypertensive challenge induced left ventricular hypertrophy, a hallmark of systemic hypertension.

Cerebral Artery TRPA1 mRNA and Protein

qPCR was used to quantify TRPA1 mRNA in cerebral arteries from control untreated compared to Ang II/HS/L-NAME treated mice. No differences were observed between the normotensive and hypertensive animals (expression ratio = 0.97 ± 0.23 vs. untreated; n = 3 per group) (Figure 4.2A). TRPA1 protein in cerebral arteries was also assessed by Western blot. No differences were observed between untreated and Ang II/HS/L-NAME-treated mouse cerebral arteries (1.0 ± 0.1 (untreated) vs. 0.9 ± 0.1 (treated); n = 3 per group) (Figure 4.2B).

Cerebral Artery TRPA1 Activity

NADPH-induced dilation was examined in cerebral arteries from untreated and Ang II/HS/L-NAME-treated mice. NADPH-induced dilation was enhanced following

hypertensive treatment (24.4 ± 5.3% dilation (untreated) vs. 54.7 ± 14.4% dilation (Ang II/HS/L-NAME; n = 3-5 per group). Interestingly, this response was nearly abolished when arteries were pretreated with the TRPA1 blocker HC-030031 (-5.5 ± 5.3% dilation (untreated), -1.5 ± 4.0% dilation (Ang II/HS/L-NAME); n = 3 per group) (Figure 4.2C).

Cardiovascular Parameters: eTRPA1$^{-/-}$ Mice

Baseline mean arterial pressure (102.9 ± 1.1 mmHg, n = 6) and heart rate (464.6 ± 3.8 bpm) of eTRPA1$^{-/-}$ animals were similar to that of control mice (Figure 4.1 A and B). Implementation of Ang II/HS and L-NAME increased the blood pressure in eTRPA1$^{-/-}$ mice (130.0 ± 1.3 mmHg for Ang II/HS, 146.0 ± 2.2 mmHg) to the same extent as the control mice (Figure 4.1 A and B). Other cardiovascular parameters were also recorded and compared, however, no statistical differences were observed between eTRPA1$^{-/-}$ and control mice (Table 4.1). Cardiac (0.004 ± 0.0001 (untreated) vs. 0.007 ± 0.0004 (treated); n = 7-17) and left ventricular (0.380 ± 0.014 (untreated) vs. 0.500 ± 0.007 (treated); n = 7-17) hypertrophy was also observed in the eTRPA1$^{-/-}$ mice treated with Ang II/HS/L-NAME, however the extent of the remodeling was not different from the hypertensive control animals (Figure 4.1 C and D).

Survival

The survival of mice following initiation of L-NAME treatment was tracked for control and eTRPA1$^{-/-}$ mice. When mice developed neurological signs of stroke, mice were sacrificed. Control mice treated with Ang II/HS/L-NAME develop clinical signs of

stroke within 8 weeks following initiation of L-NAME treatment (n = 23) (Figure 4.3A). In contrast, eTRPA1$^{-/-}$ mice all experience clinical signs of stroke within 3 weeks after the start of L-NAME treatment (n = 24) (Figure 4.3A).

Histopathology of the Brain

Brains from control and eTRPA1$^{-/-}$ mice that were untreated or treated with Ang II/HS/L-NAME were removed and subjected to diaminobenzidine staining in addition to Hematoxylin and eosin staining. Both stains were used to highlight the presence of diffuse patches of blood within neuronal tissue, identifying intracerebral hemorrhage (ICH) lesions (Figure 4.3 B). ICH lesions in untreated control and eTRPA1$^{-/-}$ mice were rarely observed (Table 4.2). On the contrary, control animals treated with Ang II/HS/L-NAME developed numerous ICH lesions (50 ± 9.3; n = 3 mice), most of them occurring in the brainstem (Figure 4.3C). On average, ICH lesions in control, treated mice were 0.124 ± 0.044 mm^3 (n = 3 mice) (Figure 4.3D). Interestingly, hypertensive eTRPA1$^{-/-}$ mice displayed more ICH lesions compared to control mice (75 ± 0.9; n = 3 mice), however, the average size of lesions present in these animals were much smaller (0.028 ± 0.007 mm^3; n = 3 mice) (Figure 4.3 C and D).

DISCUSSION

The data presented here provide the first evidence that TRPA1 channels present in the endothelium of cerebral arteries are critical in delaying the onset of hypertension-

associated hemorrhagic stroke. In addition, we also describe a new model for hypertension-associated spontaneous hemorrhagic stroke in mice.

Ang II/HS/L-NAME Compared to Other Hypertension-Associated Stroke Models

All mice undergoing infusion of Ang II in conjunction with a high salt chow and NOS inhibitor L-NAME (Ang II/HS/L-NAME) develop intracerebral hemorrhage (ICH) and die within 2 months of treatment. ICH lesions were apparent within all regions of the brain but the largest lesions were predominantly present in the midbrain and brainstem. The size and distribution of ICH lesions in this model is similar to that of the model used in Wakisaka et al., Ang II infusion (1000 ng/kg/min) and L-NAME water (100 mg/kg/day) for 1 week, then addition of Ang II (0.5 μg/g) subcutaneous injections twice daily (chronic/acute Ang II) (*173*). In this model, 73% of mice developed neurological signs within 3 weeks of treatment. Both this model and the model presented in the current study are easily applied to transgenic mice, as no additional breeding schemes need to be implemented. In contrast, mice treated with Ang II/HS/L-NAME do not require twice daily injections of Ang II, making this model less labor intensive. On the contrary, the chronic/acute Ang II model develops signs of stroke within 3 weeks of treatment initiation, whereas the Ang II/HS/L-NAME model develops clinical signs within 4-8 weeks following treatment. In this way, the Ang II/HS/L-NAME model may mimic more chronic hypertension-associated stroke compared to the chronic/acute Ang II model which develops stroke relatively quickly following initiation of hypertension.

Results using the Ang II/HS/L-NAME model described here are quite different from another model of hypertension-associated hemorrhagic stroke, double transgenic mice over expressing human renin and angiotensinogen (R^+/A^+) treated with high salt chow and L-NAME (120 mg/kg) drinking water, described by Iida et al. (*174*). R^+/A^+ mice are genetically hypertensive, with a mean arterial pressure of ~149 mmHg at baseline (*174*). Within 3 weeks of treatment with high salt chow and L-NAME water, MAP increases to approximately 200 mmHg (*174*). In the R^+/A^+-HS/L-NAME model, fewer ICH lesions (2-8) were observed in only the brainstem, cerebellum, and basal ganglia. In addition, the size of the lesions observed in the R^+/A^+-HS/L-NAME model were much smaller than those observed in the chronic/acute Ang II and Ang II/HS/L-NAME models. One disadvantage of the R^+/A^+-HS/L-NAME model is that it is not easily applied to use with transgenic mouse lines. The R^+ and A^+ transgenes need to be crossed onto the transgenic mouse to be studied which can be time consuming and costly. This is in contrast to the Ang II/HS/L-NAME model described here and the chronic/acute Ang II model that can be easily applied to transgenic lines. However, the R^+/A^+-HS/L-NAME model may serve as a better model for genetic, chronic hypertension, as animals are hypertensive from birth. Although these three models of hypertension-associated spontaneous hemorrhagic stroke involve similar mechanisms (manipulation of the renin-angiotensin system and decreased nitric oxide generation), the experimental outcomes of each are slightly different. Therefore, the model chosen for experiments should be considered carefully.

TRPA1 Channels in Cerebral Arteries during Hypertension

TRPA1 channels are present in cerebral artery endothelial cells but are absent from the endothelium of other vascular beds (Sullivan MN, et al. 2014, in review). In this tissue, TRPA1 is activated by lipid peroxidation products formed by oxidative degradation of membrane lipids by reactive oxygen species (ROS) (Sullivan MN, et al. 2014, in review). Increased ROS production and lipid peroxidation occur in the vascular wall during hypertension (*148, 175*), and this increase in vascular ROS has been shown to potentiate increased contractility of smooth muscle cells (*176*). It is likely that increased membrane lipid oxidation leads to augmented TRPA1-mediated vasodilation, thus opposing increased smooth muscle cell contractility. Therefore, we tested the hypothesis that TRPA1 channel transcription, translation, or activity were augmented following a hypertensive challenge. We found that TRPA1 channel mRNA and protein in cerebral arteries are not altered following a hypertensive challenge. However, TRPA1 channel activity is enhanced following hypertensive treatment. Previous reports have shown that NOX activity is increased following hypertension (*177*) and our prior work indicates that NOX stimulation influences TRPA1 channel activity in the cerebral vasculature. Therefore, it is likely that increased activity of NOX, and therefore augmented ROS production, during hypertension contributes to augmented TRPA1 activity in this tissue. Interestingly, inhibition of TRPA1 channels with HC-030031 completely abolished NADPH-induced dilation. It's possible that other ROS-sensitive TRP channels present in endothelial cells, such as TRPM2 (*178*) and TRPC5 (*179*), could contribute to this response. However, blockade of TRPA1 completely inhibited the dilation to NADPH, suggesting the unlikely contribution of these channels to this

response. Further, a lack of specific pharmacology for TRPM2 and TRPC5 creates difficulty in confirming involvement of the channels in NADPH-induced dilation.

Lack of Endothelial TRPA1 Channels during Hypertension-Associated Stroke

Basal MAP and change in MAP with each of the hypertensive treatments did not vary between control and eTRPA1$^{-/-}$ mice. This is to be expected, as endothelial TRPA1 expression appears to be restricted to the cerebral circulation which does not contribute to overall MAP determination. Cardiac hypertrophy, and more specifically left ventricular hypertrophy, was also observed to the same degree in the eTRPA1$^{-/-}$ as the control animals. However, eTRPA1$^{-/-}$ mice appeared to develop hemorrhagic stroke much earlier than the control animals, suggesting that endothelial TRPA1 channels have a function in protecting the delicate cerebral arteries and delaying the onset of cerebrovascular insults, like stroke.

Interestingly, eTRPA1$^{-/-}$ mice treated with Ang II/HS/L-NAME developed more ICH lesions but overall lesions were significantly smaller compared with the ICH lesions observed in hypertensive control animals. This increase in microbleeds as opposed to larger cerebrovascular insults suggests that TRPA1 may have an important function in the deep, smaller arteries of the brain in addition to the superficial, larger pial arteries. In addition, eTRPA1$^{-/-}$ mice treated with Ang II/HS/L-NAME could serve as a model for cerebral small vessel disease, a contributor to Alzheimer's disease, dementia, and additional ischemic or hemorrhagic stroke in human patients (*180*).

TRPA1, NOX, and Stroke

One hallmark of cerebrovascular disease that is often highlighted is oxidative stress, the imbalance between ROS production and ROS scavenging. Although ROS generation is often referred to as a detrimental occurrence, ROS are critical for normal cellular and physiological function. Therefore, over-scavenging of ROS could have just as many negative outcomes as over-production of ROS. The major source of ROS in the cerebral vasculature is NADPH oxidase, where the complex has greater activity and expression than other systemic vascular beds (*142*). NOX isoforms are present in many different cell types, including endothelial cells, smooth muscle cells, neurons, and inflammatory cells, where they function in oxidizing NADPH intracellularly while reducing oxygen to O_2^- extracellularly.

There are many studies that target NADPH oxidase in the treatment or prevention of stroke. Several studies examining ischemic stroke show improvement of neuronal damage following treatment with a NOX inhibitor such as apocynin (*181*). Interestingly, one study by Tang XN et al. reported that while moderate concentrations of apocynin (2.5 mg/kg) reduced cerebral infarct following experimental ischemic stroke, higher concentrations of apocynin (5.0 mg/kg) actually increased the damage and resulted in intracerebral hemorrhage in both contralateral and ipsilateral hemispheres of the brain (*182*). One possible explanation for this outcome is that partial inhibition of NOX decreased excess ROS production, thereby simulating “normal” levels of ROS, while more complete blockade of NOX removed too much ROS generation and prevented physiological mechanisms of vascular control such as TRPA1 activity. Similarly, mice lacking TRPA1 in the cerebral vascular endothelium developed more

severe cerebrovascular disease relative to mice with functional TRPA1 channels. In addition, systemic NOX blockade would have effects on NOX in all different cell types. As endothelial expression of TRPA1 channels appears to be selective for the cerebral circulation, TRPA1 may be a better therapeutic target for stroke treatment.

SUMMARY AND CONCLUSIONS

In the present study, we characterize a novel model of hypertension-associated spontaneous hemorrhagic stroke: Ang II infusion and high salt chow for two weeks followed by addition of L-NAME-treated drinking water. Mice on this protocol develop clinical signs of stroke within 8 weeks and develop intracerebral hemorrhage throughout all brain regions. In addition, we find that mice lacking endothelial TRPA1 channels develop clinical signs of stroke earlier and have more intracerebral hemorrhage lesions compared with control mice. This work highlights the importance of TRPA1 channels in the cerebral vascular circulation, where it seems to have a protective function in delaying the onset of cerebrovascular disease. Furthermore, the function and unique expression pattern of TRPA1 make it a promising potential target for stroke prevention. Current preventative therapies for stroke are broadly targeted to reduce risk factors and are limited to antihypertensive medication and invasive surgical procedures (removal of intravascular plaques or stent placements). Advanced preventative therapies targeting primary causes of stroke would have significant economical and overall health benefits.

Table 4.1: Cardiovascular Parameters for Control and eTRPA1$^{-/-}$ Mice. Mean ± SE measurements for mean arterial pressure (MAP), heart rate (HR), systolic blood pressure (SBP), diastolic blood pressure (DBP), and pulse pressure of control (n = 8) and eTRPA1$^{-/-}$ (n = 6) mice under basal conditions and following initiation of each hypertensive treatment. Measurements were recorded using radiotelemetry.

	Condition	MAP (mmHg)	HR (bpm)	SBP (mmHg)	DBP (mmHg)	Pulse Pressure (mmHg)
Control	Baseline	102.3 ± 1.2	498.1 ± 6.7	113.0 ± 1.5	90.0 ± 1.7	23.0 ± 1.2
	Ang II/HS	126.0 ± 2.0	495.9 ± 5.5	139.2 ± 2.1	114.8 ± 2.1	24.6 ± 0.9
	+L-NAME	152.7 ± 2.5	424.2 ± 11.7	181.0 ± 4.0	131.5 ± 2.1	49.4 ± 3.1
eTRPA1$^{-/-}$	Baseline	102.9 ± 1.1	464.6 ± 3.8	115.0 ± 1.1	90.5 ± 1.3	24.4 ± 0.9
	Ang II/HS	130.0 ± 1.3	470.1 ± 6.1	147.0 ± 1.9	116.7 ± 1.3	30.3 ± 1.7
	+L-NAME	145.9 ± 2.2	431.5 ± 11.5	174.6 ± 3.4	126.4 ± 2.3	48.2 ± 3.8

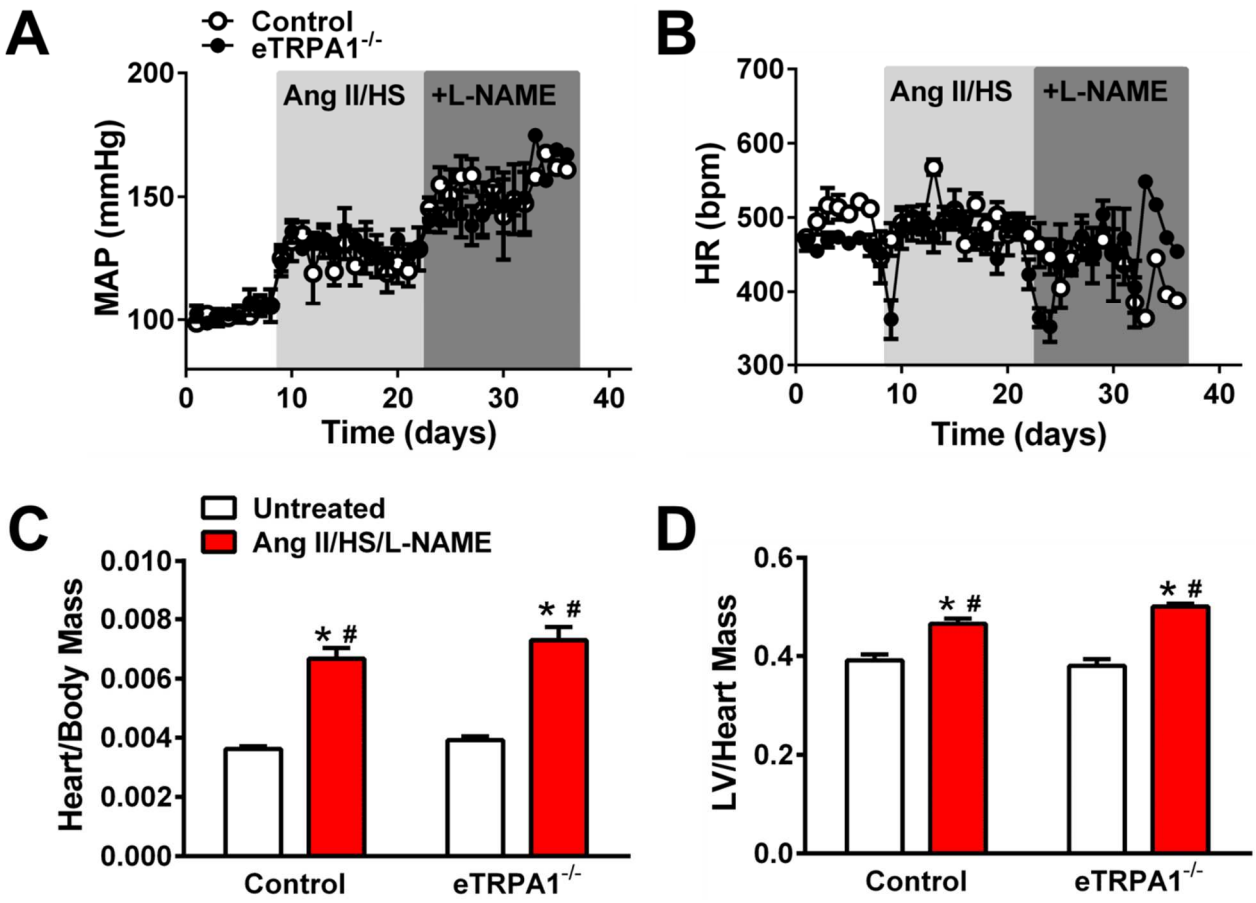

Figure 4.1: Blood pressure, heart rate, and cardiac hypertrophy indexes for mice. A and B: Graph of mean arterial pressure (MAP) and heart rate (HR) for control (n = 8) and eTRPA1$^{-/-}$ (n = 6) mice before and after implementation of hypertensive treatment as measured by radiotelemetry. C and D: Ratios of heart to body mass and left ventricle to whole heart mass for untreated mice (n = 7-18 per group) or mice treated with Ang II/HS/L-NAME (n = 17-18 per group). *P ≤ 0.05 vs. Control, untreated. #P ≤ 0.05 vs. eTRPA1$^{-/-}$, untreated.

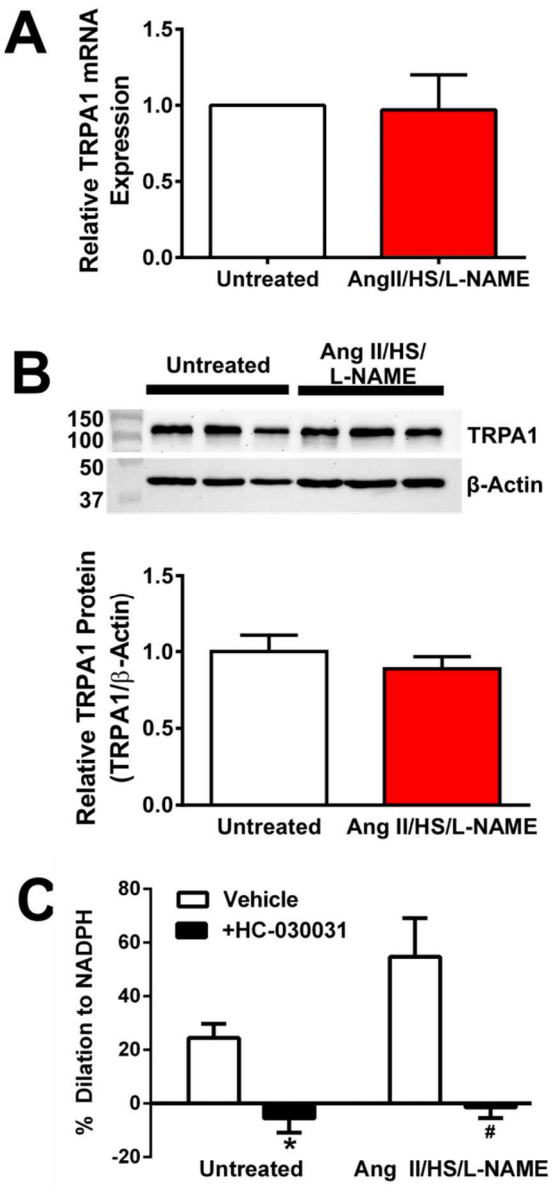

Figure 4.2. TRPA1 activity in cerebral arteries increases during hypertension. A: Relative TRPA1 mRNA Expression in cerebral arteries from untreated vs. Ang II/HS/L-NAME-treated control mice as compared to β-Actin levels (n = 3 per group). B: Representative Western blot and summary for the relative TRPA1 protein (138 kDa) in cerebral arteries from untreated vs. Ang II/HS/L-NAME-treated control mice as compared to β-Actin (42 kDa) levels (n = 3 per group). C: NADPH-induced dilation in cerebral arteries from untreated vs. Ang II/HS/L-NAME-treated mice with and without pre-treatment with HC-030031 (n = 3-5 per group). *P≤0.05 vs. Untreated, vehicle; #P≤0.05 vs. Ang II/HS/L-NAME, vehicle.

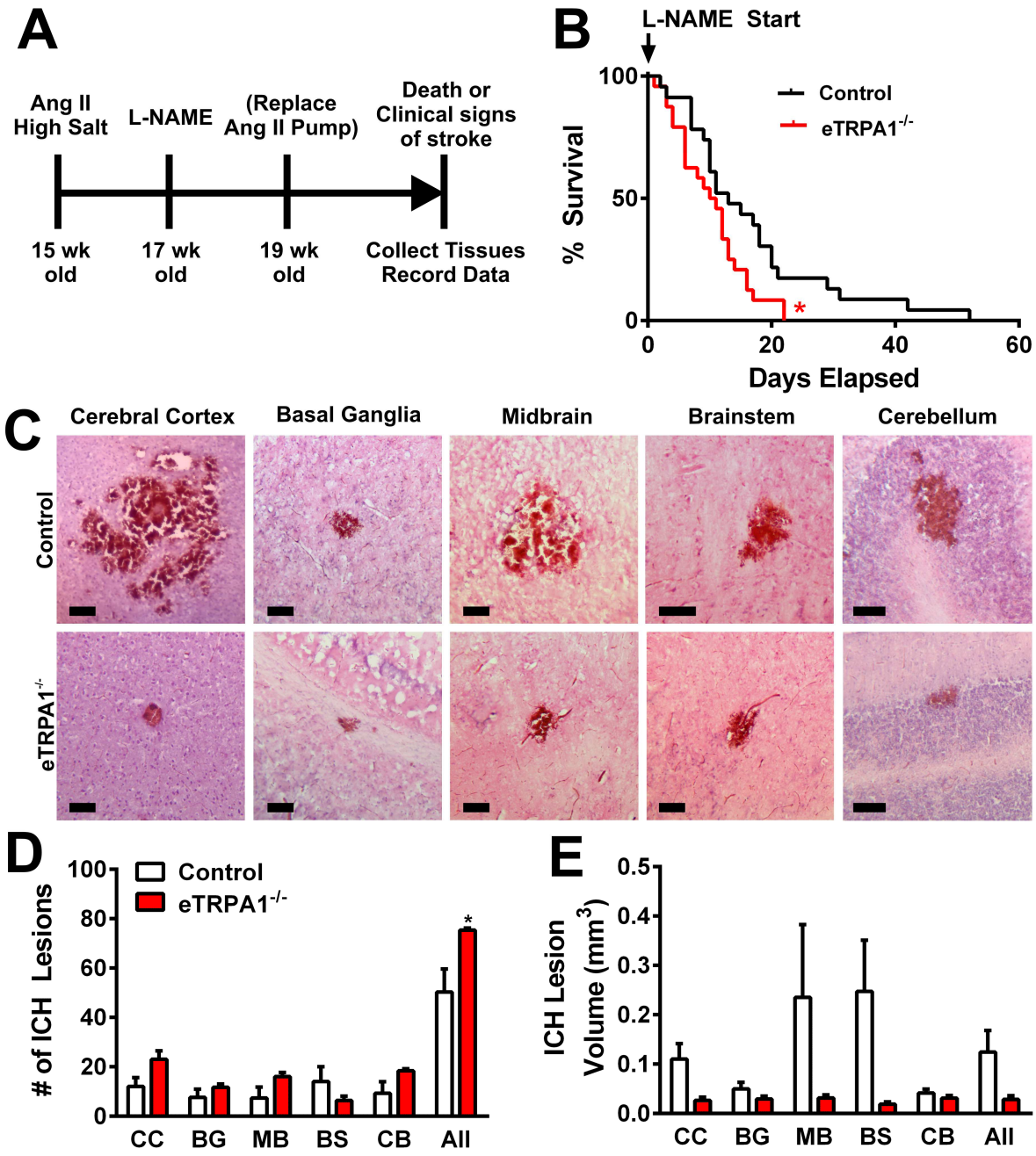

Figure 4.3: Hypertensive eTRPA1$^{-/-}$ develop spontaneous hemorrhagic stroke earlier than control mice. A: Experimental timeline indicating treatment times for mice. Mice undergo treatment until they experience death or clinical signs of stroke. B: Kaplan-Meier plot of mouse survival following initiation of L-NAME (n = 23 mice for Control and 24 mice for eTRPA1$^{-/-}$). *P ≤ 0.05 vs. Control. C: Representative images of intracerebral hemorrhage (ICH) lesions found in control and eTRPA1$^{-/-}$ mouse brain sections; scale bar = 100 μm. D and E: ICH lesion count and volume in the cerebral cortex (CC), basal ganglia (BG), midbrain (MB), brain stem (BS), or cerebellum (CB) for control mice compared to eTRPA1$^{-/-}$ mice following treatment with Ang II/HS/L-NAME

CHAPTER 5

Summary and Perspectives

TRP SPARKLETS IN THE CEREBRAL VASCULAR ENDOTHELIUM

Endothelial cell-mediated vasoregulatory pathways are highly dependent on changes in intracellular [Ca^{2+}], establishing an essential function for endothelial cell Ca^{2+} dynamics in the regulation of arterial tone. Increases in endothelial cell cytosolic [Ca^{2+}] trigger the generation of endothelium-derived vasodilatory factors, such as NO, EETs, and PGI_2, and also stimulate K_{Ca} channels (*10, 13, 20, 21*). K^+ efflux through activated K_{Ca} channels hyperpolarizes the endothelial cell membrane, and this electrical signal is conducted to the underlying smooth muscle cells to evoke relaxation (*10, 21, 22*). This is known as endothelium-dependent hyperpolarization (*20*). The principal consequence of increased endothelial cell [Ca^{2+}] is vasodilation. However, vasoconstricting factors can also be released from endothelial cells as a result of increased cytosolic [Ca^{2+}] (*183*). In these ways, endothelial cell Ca^{2+} dynamics strongly influence smooth muscle cell contractility. Changes in endothelial cell cytosolic [Ca^{2+}] are primarily achieved by Ca^{2+} entry from the extracellular space, emphasizing the significance of endothelial cell Ca^{2+} channels in vascular tone regulation.

Several TRP channels are involved in endothelial cell Ca^{2+} influx and modulation of vascular tone, including TRPV4, TRPV3, TRPC3, and TRPA1 (*5, 6, 8, 9, 114*). In rat cerebral arteries, Ca^{2+} influx through TRPA1 and TRPV3 channels induces vasodilation through endothelium-dependent hyperpolarization of the smooth muscle (*5, 6*). TRPV3 Ca^{2+} influx in the endothelium of rat mesenteric arteries evokes vasodilation through a

similar mechanism, requiring the activity of K_{Ca} channels (*8*). Endothelial cell TRPV4 Ca^{2+} influx triggers an NO-dependent dilation in rat carotid arteries but facilitates an endothelium-dependent hyperpolarizing pathway of dilation in rat skeletal muscle arteries (*114*) and cerebral arteries (*115*). These TRP channels have a high Ca^{2+} permeability and a sizeable single channel conductance, hence their substantial influence on arterial tone.

Recent efforts have employed the use of high speed, high resolution fluorescence microscopy techniques to visualize unitary TRP channel Ca^{2+} influx events, termed "TRP sparklets," in endothelial cells (*1, 9*). Isolated or intact endothelial cells containing a fluorescent Ca^{2+} indicator are subject to high speed confocal or total internal reflection fluorescence (TIRF) microscopy (*1, 9*). Endothelial cell Ca^{2+} influx is recorded as transient increases in fluorescence relative to basal fluorescence at the cell surface, and TRP channel activity is examined using selective pharmacology. TRP sparklet biophysical properties, including amplitude, duration, and spatial spread, are then analyzed and used to determine the identity of the specific TRP channel generating the Ca^{2+} influx signal.

Unitary amplitude appears to be a defining characteristic of a TRP sparklet. Sparklet unitary amplitude represents Ca^{2+} influx through a single channel and therefore depends on the unique biophysical properties of the specific channel. TRPV4 sparklets have a unitary amplitude of $\Delta F/F_0$ = 0.06 and are the smallest of the TRP sparklets recorded to date while TRPV3 sparklets are the largest ($\Delta F/F_0$ = 0.20) (Table 5.1). TRPA1 sparklet unitary amplitude is $\Delta F/F_0$ = 0.13, about halfway between the size of the other two. A similar pattern is observed with unitary conductance and relative

permeability to Ca^{2+} vs. Na^{+} ($P_{Ca2+:Na+}$) of the channels. TRPV3 channels have a unitary conductance of ~150-200 pS (*184*), which is about twice that of TRPA1 channels (98 pS) (*160*) and approximately four times greater than TRPV4 channels (~30-60 pS) (*61*). In addition, TRPV3 channel $P_{Ca2+:Na+}$ is also the greatest ($P_{Ca2+:Na+}$ = 12) (*104*) relative to TRPA1 ($P_{Ca2+:Na+}$ ~ 8) (*46*) and TRPV4 ($P_{Ca2+:Na+}$ = 6) (*106*). Therefore, TRP sparklet unitary amplitude defines the TRP sparklet because it reflects unitary channel conductance and correlates with relative Ca^{2+} permeability.

The spatial spread of TRP sparklets is determined by several factors. Sparklet spatial spread is heavily influenced by the specific subcellular arrangement of the channels within localized signaling microdomains. This includes the association of channels with each other, as is seen for TRPV4 and TRPA1 (*9*) (Figure 3.7), as well as interaction with scaffolding proteins such as AKAP150 (*82, 162*). Further, the close-association with downstream Ca^{2+} channels can amplify TRP channel Ca^{2+} influx signals via a Ca^{2+}-induced Ca^{2+} release mechanism and increase the spread of the signal (*9, 28*). Spatial spread is also affected by cytosolic Ca^{2+} sequestering mechanisms. Increased cytosolic Ca^{2+} buffering by Ca^{2+}-binding proteins increases the ratio of bound-to-unbound Ca^{2+} in the cytosol and limits the range of diffusion following initiation of a single Ca^{2+} influx signal (*185*). Moreover, variations in the activity of the sarcoendoplasmic reticulum Ca^{2+} ATPase (SERCA) pump and the plasma membrane Ca^{2+} ATPase (PMCA) will alter the removal of the Ca^{2+} from the cytosol and affect the spatial distribution of the fluorescent signal (*186, 187*). Since many factors affect the spatial spread measured for a TRP sparklet, this biophysical parameter cannot accurately be used to identify TRP channels.

TRP sparklet recordings have revealed that the activity of a few channels per endothelial cell is sufficient to evoke maximal arterial dilation. 4-8 TRPV4 channels are active when stimulated with a maximal concentration of the TRPV4-selective agonist GSK1016790A (*9*). Maximal concentrations of AITC stimulate 3-4 TRPA1 channels per cell (Sullivan, MN et al. 2014, in review), and 3-4 TRPV3 channels per cell are active when stimulated with carvacrol (Sullivan MN et al, in preparation). Interestingly, the half-maximal concentration (EC_{50}) for AITC-induced TRPA1 sparklets in endothelial cells is similar to the half-maximal concentration for AITC-induced vasodilation (Sullivan, MN et al. 2014, in review) (*6*). Similarly, Qian et al. demonstrated that the concentrations of AITC required to induce vasodilation of cerebral arteries were much lower than the doses necessary to evoke global changes in endothelial cell [Ca^{2+}] (*28*). Instead, they found that the concentration dependence of AITC to induce dilation mirrored that of AITC-induced localized Ca^{2+} signals (TRPA1 sparklets) in the endothelial cells (*28*). The maximal vasodilatory response observed following TRP sparklet activation results from two levels of amplification. First, channel clustering is observed at the membrane of endothelial cells and functions to produce a more substantial Ca^{2+} influx signal following stimulation with an agonist. TRPA1 channels exhibit binary coupling in rat cerebral artery endothelial cells and TRPV4 channels exhibit quaternary coupling, forming a four channel cluster, in mouse mesenteric artery endothelial cells (Sullivan MN, et al. 2014, in review) (*9*). Interestingly, TRPA1 channel clustering is not observed when the channel is heterologously expressed in HEK 293 cells (Sullivan MN, et al. 2014, in review). This finding highlights the importance of TRPA1 channel coupling in cerebral artery endothelial cell function and suggests that there is an anchoring mechanism

endogenous to endothelial cells that keeps two TRPA1 channels in close proximity. TRPV3 channels, on the contrary, are active predominantly as single channels (Sullivan, MN, et al 2014, in preparation). Since TRPV3 channels have a large unitary conductance and Ca^{2+} permeability, these channels may not need additional amplification by clustering. The second mode of TRP sparklet amplification occurs through downstream activation of additional Ca^{2+} release events from the endoplasmic reticulum (*27*). TRPA1 and TRPV4 sparklets in endothelial cells of rat cerebral and mouse mesenteric arteries, respectively, are sensitive to depletion of Ca^{2+} stores (*9, 28*), suggesting that the initial Ca^{2+} influx event by way of TRP sparklets activates Ca^{2+}-induced Ca^{2+} release from the endoplasmic reticulum and further intensifies the signal. Together, these mechanisms explain why only a few TRP channels per cell are required for evoking vasodilation – the signal produced by a small number of TRP sparklets in endothelial cells is amplified through channel clustering at the membrane and by additional Ca^{2+}-induced Ca^{2+} release events in order to elicit a robust vascular response.

TRP sparklets have also been recorded from smooth muscle cells. Zhao et al. reported that TRPV4 sparklets underlie proliferation of airway smooth muscle cells (*188*). In this study, we found that TRPV4 sparklets activate the Ca^{2+}/calmodulin-dependent protein phosphatase calcineurin, which de-phosphorylates nuclear factor of activated T-cells (NFAT) (*188*). When NFAT is activated, it translocates to the nucleus to mediate transcription of genes involved in cell proliferation. Interestingly, TRPV4 agonists induce translocation of NFATc3 in airway smooth muscle cells (*188*), suggesting that TRPV4 sparklets stimulate airway smooth muscle proliferation, a

hallmark of chronic asthma. These studies suggest that TRPV4 channels could be targeted in the development of treatments to reduce asthma-induced airway remodeling. An elegant study from the Santana laboratory examined the regulation of TRPV4 sparklets in vascular myocytes by PKC and the scaffolding protein AKAP150 during angiotensin II signaling (*162*). Similar to what we found in endothelial cells, basal TRPV4 sparklet activity was low in smooth muscle cells. An increase in TRPV4 sparklet frequency could be stimulated with a TRPV4 agonist (GSK1016790A) or angiotensin II that was sensitive to blockade of PKC and or genetic knockout of AKAP150 (*162*). In addition, they found that the interaction between AKAP150 and TRPV4 channels was dynamic and that each component was mobile at the cell membrane (*162*). This study highlights the importance of anchoring proteins in ion channel activity and regulation. It is likely that scaffolding proteins regulate the activity of TRP channel sparklets in the endothelium as well. TRPV4 channels exist in four channel clusters in endothelial cells (*9*) that may be formed by interaction with AKAP150. In addition, TRPA1 channels preferentially exhibit dual channel coupling in endothelial cells whereas they seem to act primarily as single channels when expressed in HEK 293 cells. These data suggest that a scaffolding mechanism for TRPA1 channels is endogenous to endothelial cells but absent from HEK 293 cells.

Endothelial cell Ca^{2+} dynamics are fundamental to endothelial cell function which is critical for maintaining vascular health (*189*). Based on these few initial studies, it is clear that endothelial cell TRP channel sparklets mediate pathways that are important for vascular function. TRP sparklets in endothelial cells target broader Ca^{2+} signals within distinct microdomains in order to elicit a vascular response (*9, 28*). Although only

3 types of TRP channel sparklets have been recorded and characterized in endothelial cells (Table 5.1), these reports have paved the way for examination of other TRP sparklets in the endothelium and other cell types. TRP channels that have a high conductance and Ca^{2+} permeability would be easily detected using these fluorescent methods. This, of course, excludes the Ca^{2+} impermeable channels TRPM4 and TRPM5 (*95, 190*). Furthermore, the availability of selective pharmacology is a principal determinant in the ability to record and isolate the activity of specific channels. Elucidating the pathways regulating TRP sparklets in the vasculature will advance our knowledge of physiological vascular function and allow us to better understand and identify pathological vascular conditions.

PHYSIOLOGICAL REGULATION OF TRPA1 IN CEREBRAL ARTERY ENDOTHELIAL CELLS

Endogenous regulation of TRPA1 channels in the endothelium of cerebral arteries has not previously been explored. TRPA1 channel activation has been studied using compounds derived from mustard oil and garlic (*6, 67*), but it's unlikely that the principal function of TRPA1 in the endothelium is to elicit vasodilation in response to dietary substances. Studies examining neuronal TRPA1 channels indicate that the channel is primarily activated by covalent modification of cysteine residues C621, C641, and C665 located on the N terminus of the protein (*48, 191, 192*). Cysteine-reactive molecules, such as reactive oxygen species (ROS), reactive nitrogen species, and products of lipid peroxidation, can modify TRPA1 channel activity in sensory and dorsal

root ganglionic neurons (*193, 194*). In addition, TRPA1 channels are sensitive to both hypoxia and hyperoxia through a combination of cysteine and proline residue modifications (*48*). It is much more likely that TRPA1 serves as a sensor of oxidative stress and oxygen concentration in the vasculature. However, no prior studies have investigated the interaction of TRPA1 channels with ROS-generating enzymes in cerebral artery endothelial cells.

Here we find that TRPA1 channels are functionally coupled to the ROS-generating enzyme complex NADPH oxidase 2 (NOX2) in cerebral artery endothelial cells. There are several sources of ROS in vascular cells, including xanthine oxidase, cyclooxygenase, and mitochondria, but the major source of ROS in the cerebral vasculature is NOX (*142*). Three different isoforms of NOX are present in cerebral artery endothelial cells: NOX1, NOX2, and NOX4 (*142, 154, 195*) (Figures 3.1 and 3.2). Interestingly, TRPA1 co-localizes with NOX2 in this tissue but does not associate with other isoforms, such as NOX4 (Figure 3.1). We tested the hypothesis that NOX stimulation could influence the activity of TRPA1 in endothelial cells. Indeed, activation of NOX with its substrate NADPH increases the frequency of TRPA1 sparklets in isolated endothelial cells (Figure 3.7). In addition, NOX stimulation induces TRPA1-mediated vasodilation of cerebral arteries (Figure 3.10). These responses were attenuated by the small inhibitory peptide gp91ds-tat, generated to specifically inhibit NOX2-containing complexes, providing functional evidence that ROS generated by NOX2 influence TRPA1-dependent vasodilation (Figure 3.11). Although NOX2 and TRPA1 channels are located within 40 nm of each other, they do not physically interact (Figure 3.6). It's possible that other sources of ROS present in endothelial cells

contribute to TRPA1 activation. However, several reports have noted the limited contribution of these enzymes to ROS generation relative to NOX in the endothelium (*142, 196*). Together our data and previous reports support a role for NOX2 activity in the stimulation of TRPA1 channels within highly localized signaling microdomains in the endothelium of cerebral arteries.

Endothelial cell TRPA1 channels are activated by NOX-dependent generation of oxidized membrane lipids. Although previous reports have also demonstrated a dilatory effect of NADPH in cerebral arteries, the underlying mechanism was unknown (*142, 166, 197, 198*). Data presented here reveal that TRPA1 channels are the targets that mediate NOX-dependent vasodilation. NOX activity affects TRPA1 Ca^{2+} influx through the generation of multiple ROS. O_2^- production by NOX is dismutated to H_2O_2 and broken down into OH• by Fenton's reaction (*149*). OH• are unstable radicals generated endogenously, and they frequently react with nearby membrane lipids to form lipid peroxidation products (*149*). These oxidized membrane lipids form Michael addition adducts with N-terminal cysteine residues of TRPA1 channels (*145, 194*). In support of this pathway, NADPH-induced cerebral vasodilation and increased TRPA1 activity is sensitive to breakdown of H_2O_2 with catalase (Figure 3.11), and inhibition of Fenton's reaction with deferoxamine, which prevents OH• generation, also attenuates NADPH-induced TRPA1 sparklets and TRPA1-mediated vasodilation (Figure 3.11). These data suggest that the formation of oxidized membrane lipid byproducts is required for NOX-dependent TRPA1 activation. Furthermore, oxidized membrane lipids, such as 4-HNE, activate TRPA1 channel activity in endothelial cells and induce TRPA1-mediated vasodilation of cerebral arteries (Figure 3.12). Together, these data describe a novel

pathway of endogenous regulation of TRPA1 channel activity in cerebrovascular endothelial cells. Data presented here provide the first evidence that TRPA1 channels function as sensors of NOX-dependent oxidative membrane degradation in the cerebral artery endothelium.

PATHOPHYSIOLOGICAL SIGNIFICANCE OF TRPA1 CHANNELS IN THE CEREBRAL ARTERY ENDOTHELIUM

Hypertension is the greatest risk factor that contributes to the development of cerebrovascular disease (*199*). During hypertension, the endothelium becomes damaged and reduces the vasodilatory capacity of arterioles (*200*). In addition, smooth muscle cell contractility is enhanced in cerebral vessels (*201-204*). Endothelial dysfunction and augmented vasoconstriction significantly increase the risk of severe cerebrovascular insults, like stroke. Stroke is the fourth leading cause of death in the United States and is responsible for 10% of deaths worldwide (*167, 168*). There is a linear relationship between blood pressure and stroke mortality (*205*), therefore, blood pressure control is a critical component in reducing the risk of stroke occurrence.

A strong association between oxidative stress and the progression of hypertension has been well established (*206, 207*). Oxidative stress is defined as an imbalance between ROS generation and ROS detoxification by antioxidants (*208*) and generally manifests as an overproduction of ROS within a cell. Increased ROS levels are observed in several models of hypertension, including angiotensin II or endothelin-1 infusion, spontaneously hypertensive rats, renin-angiotensin system transgenic mice,

and the deoxycorticosterone acetate (DOCA)-salt model (*195, 209-211*). Altered ROS balance in the vasculature can have several effects that potentiate the development of hypertension. Increased superoxide production leads to reduced NO bioavailability by the reaction of O_2^- with NO to generate peroxynitrite (*2*). This causes impaired vasodilation and NOS uncoupling (*212*) as well as increases the potential for ROS-induced vasoconstriction (*176, 213-215*). In addition, chronically elevated ROS levels contribute to vascular remodeling (*216-218*), which exacerbate the hypertensive condition. Variations in ROS production within brain regions involved in blood pressure control also contribute to neurohumoral changes that potentiate hypertension (*219*). Moreover, increased oxidative membrane lipid damage has been observed following increased ROS during hypertension (*148, 164*). Thus, augmented ROS generation during hypertension has a significant impact on vascular biology and function.

Elevated NOX-derived ROS and lipid peroxidation augment TRPA1 activity in cerebral artery endothelial cells during hypertension. NOX expression increases in the vascular wall of cerebral and systemic arteries during hypertension (*166, 220-222*), and this is associated with an elevation in NOX-dependent superoxide production in several different models of hypertension (*166, 177, 195, 220, 222-224*). Enhanced NADPH-induced cerebral vasodilation is observed in SHR animals (*166*) and Ang II/HS/L-NAME mice (Figure 4.2). Interestingly, NADPH-induced dilation of hypertensive mouse cerebral arteries is nearly abolished following TRPA1 inhibition (Figure 4.2). Furthermore, lipid peroxidation in the vascular wall is increased during hypertension (*148, 164*) due to increased ROS and decreased activity of glutathione peroxidases (*225*), the enzymes responsible for reducing lipid hydroperoxide accumulation. Since

TRPA1 channels are highly sensitive to lipid peroxidation products (*145, 194*) (Figure 3.12), increased TRPA1-mediated dilation is likely due to increased oxidative degradation of lipids in the plasma membrane. Together, these findings strongly suggest that TRPA1 channel activity is augmented in cerebral arteries during hypertension as a result of enhanced NOX-dependent ROS-mediated oxidative membrane degradation.

TRPA1 activity functions to protect the cerebral vasculature from severe insults, like stroke, during hypertension. TRPA1 channel expression in the endothelium appears to be restricted to certain vascular beds, including cerebral arteries (*6*) (Figures 3.1 and 3.3). The ability of TRPA1 channels to mediate vasodilation (*6*) (Figure 3.10) along with its unique expression pattern (Figure 3.1) strongly suggest an important function for the channel in this tissue. Hypertensive mice lacking TRPA1 channels in the cerebral artery endothelium develop clinical signs of stroke earlier than mice with functional TRPA1 (Figure 4.3), supporting the concept that TRPA1 activity is protective during vascular disease. During hypertension, increased arterial pressure causes cerebral vessels to constrict in order to protect downstream arterioles (*226*). This occurs from myogenic constriction and normal autoregulation of blood flow, first described by *Bayliss et al.* in 1902 (*227*). In addition to autoregulatory constriction, hypertension increases smooth muscle cell contractility (*201-204*) from chronically elevated ROS generation and greater levels of circulating vasoconstrictors (*228*). This increases cerebrovascular resistance and, thus, augments cerebral perfusion pressure and tangential stress on the vascular wall (*229*), damaging the endothelium over time. Downstream, cerebral blood flow to deep regions of the brain becomes reduced. It is conceivable that enhanced

vascular NOX activity augments TRPA1-mediated vasodilation to counterbalance increased vasoconstriction and maintain cerebral blood flow in the brain. Without functional TRPA1 channels, the luminal diameter of the vessel would remain reduced and lead to a deregulation of blood flow. Consequently, the vessel wall continues to weaken to the point of hemorrhage, resulting in hemorrhagic stroke (*230, 231*). This hypothesis is supported by a study by Tang et al. demonstrated that inhibition of NOX activity increases the severity of hemorrhagic stroke in mice (*182*), likely due to an attenuation of TRPA1 activity upon NOX blockade. In addition, NOX activation in non-cerebral arteries is associated with endothelial dysfunction and increased vascular tone (*232*), possibly from the absence of TRPA1 channels in these vascular beds. More interestingly, humans with a specific mutation (C242T) in the p22phox subunit of NOX, which results in decreased NOX activity (*233*), were found to be at an increased risk of stroke (*234*). Together these data and previous reports support a protective function of endothelial cell TRPA1 channels in the cerebral vasculature during vascular disease.

eTRPA1$^{-/-}$ mice treated with Ang II/HS/L-NAME may be a novel mouse model of cerebral small vessel disease. Cerebral small vessel disease accounts for 25-30% of strokes and is the primary cause of hypertension-related cognitive decline (*235*). It results from damage to the penetrating and parenchymal arterioles in the brain (*236*). A decrease in the density of functional arterioles and capillaries is also associated with this disease and leads to a reduction in cerebral blood flow and hypoperfusion of the brain (*237*). Chronic hypoperfusion underlies vascular cognitive impairment and vascular dementia that is observed in some hypertensive patients (*238*). Patients with sporatic cerebral small vessel disease often exhibit cerebral microbleeds in deep

regions of the brain, such as the midbrain and basal ganglia, as well as within the cortex (*239-242*). Lack of TRPA1 channels in cerebral artery endothelial cells during hypertensive treatment increased the number of intracerebral hemorrhage lesions; however, the lesions tended to be smaller compared to those observed in control animals (Figure 4.3). These data suggest that hypertensive eTRPA1$^{-/-}$ mice experienced cerebral microbleeds, and these mice may be a useful model for studying cerebral small vessel disease.

CONCLUSIONS

Maintaining endothelial cell function is critical in delaying the development of cardiovascular and cerebrovascular disease. TRP channel Ca^{2+} influx, manifested as TRP sparklets, underlies endothelial cell signaling crucial for eliciting vascular responses. Examining TRP sparklet properties and mechanisms of regulation has revealed important aspects of vascular biology and function. Understanding these regulatory pathways for TRP channels by extensive study of TRP sparklets may give insight into preserving endothelial cell function and delaying the onset of cardiovascular disease.

TRPA1 sparklets, in particular, have a substantial function in the endothelium of cerebral arteries. The cerebral circulation requires unique mechanisms of vascular regulation in order to meet the metabolic demands of the brain despite other changes occurring in the body. The presence of TRPA1 channels in the endothelium are an exclusive feature of this vascular bed. Elevated activity of TRPA1 during vascular

disease is likely a mechanism that evolved to counter the detrimental effects of increased ROS generation in cerebral arteries during hypertension. Further, TRPA1 channel sparklets underlie the paradoxical effects of NOX activity in cerebral vessels, another feature of this vascular bed that is unlike any other. TRPA1 channels function to protect the brain from hemorrhagic stroke by mediating vasodilation and reducing wall tension to prevent arteriole rupture. Interestingly, a dilatory response is often observed downstream of a vessel blockage. Since TRPA1 channels are sensitive to hypoxia and products of oxidative stress, it is likely that the channel also plays a role in protecting against ischemic stroke. Further studies examining the involvement of TRPA1 channels in other cerebrovascular disorders are warranted.

Absence of endothelial cell TRPA1 channels during severe hypertension results in a decreased latency to signs of hemorrhagic stroke, demonstrating a protective function for the channel during vascular disease. Systemic inhibition of TRPA1 is often considered as a treatment for chronic pain (*243*). Based on the work presented here, physicians should be cautious to prescribe drugs that chronically antagonize TRPA1 channels as it could be detrimental to a person's cerebrovascular health if he or she is at risk for stroke. Furthermore, analysis of human TRPA1 single nucleotide polymorphisms (SNPs) that result in decreased or inactivity of the channel may be useful in determining if an individual is at an increased risk of stroke.

Table 5.1: Characteristics of TRP Sparklets Recorded from Endothelial Cells Mode biophysical properties of TRPV3, TRPV4 and TRPA1 sparklets recorded from endothelial cells. *Data from (*1*). †Data from Sullivan, M.N., et al. (in review).

	TRPV3 Sparklets	**TRPV4 Sparklets***	**TRPA1 Sparklets†**
Unitary Amplitude ($\Delta F/F_0$)	0.20	0.06	0.13
Mode Amplitude (F/F_0)	1.20	1.12	1.26
Mode Duration (ms)	70	60	60
Mode Attack Time (ms)	30	30	30
Mode Decay Time (ms)	30	30	30
Mode Spatial Spread (μm^2)	0.74	0.72	0.72

References

1. M. N. Sullivan, M. Francis, N. L. Pitts, M. S. Taylor, S. Earley, Optical recording reveals novel properties of GSK1016790A-induced vanilloid transient receptor potential channel TRPV4 activity in primary human endothelial cells. *Mol Pharmacol* **82**, 464-472 (2012).
2. G. M. Rubanyi, J. C. Romero, P. M. Vanhoutte, Flow-induced release of endothelium-derived relaxing factor. *Am J Physiol* **250**, H1145-1149 (1986).
3. L. J. Ignarro, G. M. Buga, K. S. Wood, R. E. Byrns, G. Chaudhuri, Endothelium-derived relaxing factor produced and released from artery and vein is nitric oxide. *Proc Natl Acad Sci U S A* **84**, 9265-9269 (1987).
4. A. Demuro, I. Parker, "Optical patch-clamping": single-channel recording by imaging Ca2+ flux through individual muscle acetylcholine receptor channels. *J Gen Physiol* **126**, 179-192 (2005).
5. S. Earley, A. L. Gonzales, Z. I. Garcia, A dietary agonist of transient receptor potential cation channel V3 elicits endothelium-dependent vasodilation. *Mol Pharmacol* **77**, 612-620 (2010).
6. S. Earley, A. L. Gonzales, R. Crnich, Endothelium-dependent cerebral artery dilation mediated by TRPA1 and Ca2+-Activated K+ channels. *Circ Res* **104**, 987-994 (2009).
7. D. X. Zhang, S. A. Mendoza, A. H. Bubolz, A. Mizuno, Z. D. Ge, R. Li, D. C. Warltier, M. Suzuki, D. D. Gutterman, Transient receptor potential vanilloid type

4-deficient mice exhibit impaired endothelium-dependent relaxation induced by acetylcholine in vitro and in vivo. *Hypertension* **53**, 532-538 (2009).

8. S. Senadheera, Y. Kim, T. H. Grayson, S. Toemoe, M. Y. Kochukov, J. Abramowitz, G. D. Housley, R. L. Bertrand, P. S. Chadha, P. P. Bertrand, T. V. Murphy, M. Tare, L. Birnbaumer, S. P. Marrelli, S. L. Sandow, Transient receptor potential canonical type 3 channels facilitate endothelium-derived hyperpolarization-mediated resistance artery vasodilator activity. *Cardiovasc Res* **95**, 439-447 (2012).
9. S. K. Sonkusare, A. D. Bonev, J. Ledoux, W. Liedtke, M. I. Kotlikoff, T. J. Heppner, D. C. Hill-Eubanks, M. T. Nelson, Elementary Ca2+ signals through endothelial TRPV4 channels regulate vascular function. *Science* **336**, 597-601 (2012).
10. G. Edwards, M. Feletou, A. H. Weston, Endothelium-derived hyperpolarising factors and associated pathways: a synopsis. *Pflugers Arch* **459**, 863-879 (2010).
11. T. B. Bolton, R. J. Lang, T. Takewaki, Mechanisms of action of noradrenaline and carbachol on smooth muscle of guinea-pig anterior mesenteric artery. *J Physiol* **351**, 549-572 (1984).
12. C. J. Garland, F. Plane, B. K. Kemp, T. M. Cocks, Endothelium-dependent hyperpolarization: a role in the control of vascular tone. *Trends Pharmacol Sci* **16**, 23-30 (1995).
13. W. B. Campbell, D. Gebremedhin, P. F. Pratt, D. R. Harder, Identification of epoxyeicosatrienoic acids as endothelium-derived hyperpolarizing factors. *Circ Res* **78**, 415-423 (1996).

14. G. Edwards, K. A. Dora, M. J. Gardener, C. J. Garland, A. H. Weston, K+ is an endothelium-derived hyperpolarizing factor in rat arteries. *Nature* **396**, 269-272 (1998).

15. S. D. Chauhan, H. Nilsson, A. Ahluwalia, A. J. Hobbs, Release of C-type natriuretic peptide accounts for the biological activity of endothelium-derived hyperpolarizing factor. *Proc Natl Acad Sci U S A* **100**, 1426-1431 (2003).

16. C. M. Wei, S. Hu, V. M. Miller, J. C. Burnett, Jr., Vascular actions of C-type natriuretic peptide in isolated porcine coronary arteries and coronary vascular smooth muscle cells. *Biochem Biophys Res Commun* **205**, 765-771 (1994).

17. R. Hosoki, N. Matsuki, H. Kimura, The possible role of hydrogen sulfide as an endogenous smooth muscle relaxant in synergy with nitric oxide. *Biochem Biophys Res Commun* **237**, 527-531 (1997).

18. W. Zhao, J. Zhang, Y. Lu, R. Wang, The vasorelaxant effect of H(2)S as a novel endogenous gaseous K(ATP) channel opener. *EMBO J* **20**, 6008-6016 (2001).

19. J. L. Beny, P. Y. von der Weid, Hydrogen peroxide: an endogenous smooth muscle cell hyperpolarizing factor. *Biochem Biophys Res Commun* **176**, 378-384 (1991).

20. H. A. Coleman, M. Tare, H. C. Parkington, EDHF is not K+ but may be due to spread of current from the endothelium in guinea pig arterioles. *Am J Physiol Heart Circ Physiol* **280**, H2478-2483 (2001).

21. M. S. Taylor, A. D. Bonev, T. P. Gross, D. M. Eckman, J. E. Brayden, C. T. Bond, J. P. Adelman, M. T. Nelson, Altered expression of small-conductance Ca2+-

activated K+ (SK3) channels modulates arterial tone and blood pressure. *Circ Res* **93**, 124-131 (2003).

22. H. A. Coleman, M. Tare, H. C. Parkington, Endothelial potassium channels, endothelium-dependent hyperpolarization and the regulation of vascular tone in health and disease. *Clin Exp Pharmacol Physiol* **31**, 641-649 (2004).
23. P. D. Smith, S. E. Brett, K. D. Luykenaar, S. L. Sandow, S. P. Marrelli, E. J. Vigmond, D. G. Welsh, KIR channels function as electrical amplifiers in rat vascular smooth muscle. *J Physiol* **586**, 1147-1160 (2008).
24. H. K. Surks, cGMP-dependent protein kinase I and smooth muscle relaxation: a tale of two isoforms. *Circ Res* **101**, 1078-1080 (2007).
25. A. F. Brotherton, J. C. Hoak, Role of Ca2+ and cyclic AMP in the regulation of the production of prostacyclin by the vascular endothelium. *Proc Natl Acad Sci U S A* **79**, 495-499 (1982).
26. G. J. Dusting, S. Moncada, J. R. Vane, Prostacyclin (PGX) is the endogenous metabolite responsible for relaxation of coronary arteries induced by arachindonic acid. *Prostaglandins* **13**, 3-15 (1977).
27. J. Ledoux, M. S. Taylor, A. D. Bonev, R. M. Hannah, V. Solodushko, B. Shui, Y. Tallini, M. I. Kotlikoff, M. T. Nelson, Functional architecture of inositol 1,4,5-trisphosphate signaling in restricted spaces of myoendothelial projections. *Proc Natl Acad Sci U S A* **105**, 9627-9632 (2008).
28. X. Qian, M. Francis, V. Solodushko, S. Earley, M. S. Taylor, Recruitment of dynamic endothelial Ca2+ signals by the TRPA1 channel activator AITC in rat cerebral arteries. *Microcirculation* **20**, 138-148 (2013).

29. J. Metz, E. Weihe, Intercellular junctions in the full term human placenta. II. Cytotrophoblast cells, intravillous stroma cells and blood vessels. *Anat Embryol (Berl)* **158**, 167-178 (1980).

30. S. L. Sandow, C. E. Hill, Incidence of myoendothelial gap junctions in the proximal and distal mesenteric arteries of the rat is suggestive of a role in endothelium-derived hyperpolarizing factor-mediated responses. *Circ Res* **86**, 341-346 (2000).

31. S. L. Sandow, K. Goto, N. M. Rummery, C. E. Hill, Developmental changes in myoendothelial gap junction mediated vasodilator activity in the rat saphenous artery. *J Physiol* **556**, 875-886 (2004).

32. S. L. Sandow, C. B. Neylon, M. X. Chen, C. J. Garland, Spatial separation of endothelial small- and intermediate-conductance calcium-activated potassium channels (K(Ca)) and connexins: possible relationship to vasodilator function? *J Anat* **209**, 689-698 (2006).

33. B. S. Kirby, A. Bruhl, M. N. Sullivan, M. Francis, F. A. Dinenno, S. Earley, Robust internal elastic lamina fenestration in skeletal muscle arteries. *PLoS One* **8**, e54849 (2013).

34. S. Wu, T. M. Moore, G. H. Brough, S. R. Whitt, M. Chinkers, M. Li, T. Stevens, Cyclic nucleotide-gated channels mediate membrane depolarization following activation of store-operated calcium entry in endothelial cells. *J Biol Chem* **275**, 18887-18896 (2000).

35. X. Yao, P. S. Leung, H. Y. Kwan, T. P. Wong, M. W. Fong, Rod-type cyclic nucleotide-gated cation channel is expressed in vascular endothelium and vascular smooth muscle cells. *Cardiovasc Res* **41**, 282-290 (1999).

36. K. Yamamoto, R. Korenaga, A. Kamiya, Z. Qi, M. Sokabe, J. Ando, P2X(4) receptors mediate ATP-induced calcium influx in human vascular endothelial cells. *Am J Physiol Heart Circ Physiol* **279**, H285-292 (2000).

37. A. S. Chang, S. M. Chang, R. L. Garcia, W. P. Schilling, Concomitant and hormonally regulated expression of trp genes in bovine aortic endothelial cells. *FEBS Lett* **415**, 335-340 (1997).

38. M. Freichel, S. H. Suh, A. Pfeifer, U. Schweig, C. Trost, P. Weissgerber, M. Biel, S. Philipp, D. Freise, G. Droogmans, F. Hofmann, V. Flockerzi, B. Nilius, Lack of an endothelial store-operated Ca2+ current impairs agonist-dependent vasorelaxation in TRP4-/- mice. *Nat Cell Biol* **3**, 121-127 (2001).

39. T. Voets, J. Prenen, J. Vriens, H. Watanabe, A. Janssens, U. Wissenbach, M. Bodding, G. Droogmans, B. Nilius, Molecular determinants of permeation through the cation channel TRPV4. *J Biol Chem* **277**, 33704-33710 (2002).

40. K. Yamamoto, R. Korenaga, A. Kamiya, J. Ando, Fluid shear stress activates Ca(2+) influx into human endothelial cells via P2X4 purinoceptors. *Circ Res* **87**, 385-391 (2000).

41. M. Suzuki, A. Mizuno, K. Kodaira, M. Imai, Impaired pressure sensation in mice lacking TRPV4. *J Biol Chem* **278**, 22664-22668 (2003).

42. W. Liedtke, Y. Choe, M. A. Marti-Renom, A. M. Bell, C. S. Denis, A. Sali, A. J. Hudspeth, J. M. Friedman, S. Heller, Vanilloid receptor-related osmotically

activated channel (VR-OAC), a candidate vertebrate osmoreceptor. *Cell* **103**, 525-535 (2000).

43. M. J. Caterina, M. A. Schumacher, M. Tominaga, T. A. Rosen, J. D. Levine, D. Julius, The capsaicin receptor: a heat-activated ion channel in the pain pathway. *Nature* **389**, 816-824 (1997).

44. D. D. McKemy, W. M. Neuhausser, D. Julius, Identification of a cold receptor reveals a general role for TRP channels in thermosensation. *Nature* **416**, 52-58 (2002).

45. A. M. Peier, A. J. Reeve, D. A. Andersson, A. Moqrich, T. J. Earley, A. C. Hergarden, G. M. Story, S. Colley, J. B. Hogenesch, P. McIntyre, S. Bevan, A. Patapoutian, A heat-sensitive TRP channel expressed in keratinocytes. *Science* **296**, 2046-2049 (2002).

46. G. M. Story, A. M. Peier, A. J. Reeve, S. R. Eid, J. Mosbacher, T. R. Hricik, T. J. Earley, A. C. Hergarden, D. A. Andersson, S. W. Hwang, P. McIntyre, T. Jegla, S. Bevan, A. Patapoutian, ANKTM1, a TRP-like channel expressed in nociceptive neurons, is activated by cold temperatures. *Cell* **112**, 819-829 (2003).

47. G. D. Smith, M. J. Gunthorpe, R. E. Kelsell, P. D. Hayes, P. Reilly, P. Facer, J. E. Wright, J. C. Jerman, J. P. Walhin, L. Ooi, J. Egerton, K. J. Charles, D. Smart, A. D. Randall, P. Anand, J. B. Davis, TRPV3 is a temperature-sensitive vanilloid receptor-like protein. *Nature* **418**, 186-190 (2002).

48. N. Takahashi, T. Kuwaki, S. Kiyonaka, T. Numata, D. Kozai, Y. Mizuno, S. Yamamoto, S. Naito, E. Knevels, P. Carmeliet, T. Oga, S. Kaneko, S. Suga, T.

Nokami, J. Yoshida, Y. Mori, TRPA1 underlies a sensing mechanism for O2. *Nature chemical biology* **7**, 701-711 (2011).

49. N. Weissmann, N. Sommer, R. T. Schermuly, H. A. Ghofrani, W. Seeger, F. Grimminger, Oxygen sensors in hypoxic pulmonary vasoconstriction. *Cardiovasc Res* **71**, 620-629 (2006).

50. M. Aarts, K. Iihara, W. L. Wei, Z. G. Xiong, M. Arundine, W. Cerwinski, J. F. MacDonald, M. Tymianski, A key role for TRPM7 channels in anoxic neuronal death. *Cell* **115**, 863-877 (2003).

51. S. E. Jordt, D. M. Bautista, H. H. Chuang, D. D. McKemy, P. M. Zygmunt, E. D. Hogestatt, I. D. Meng, D. Julius, Mustard oils and cannabinoids excite sensory nerve fibres through the TRP channel ANKTM1. *Nature* **427**, 260-265 (2004).

52. H. Xu, M. Delling, J. C. Jun, D. E. Clapham, Oregano, thyme and clove-derived flavors and skin sensitizers activate specific TRP channels. *Nat Neurosci* **9**, 628-635 (2006).

53. R. L. Garcia, W. P. Schilling, Differential expression of mammalian TRP homologues across tissues and cell lines. *Biochem Biophys Res Commun* **239**, 279-283 (1997).

54. H. Watanabe, J. B. Davis, D. Smart, J. C. Jerman, G. D. Smith, P. Hayes, J. Vriens, W. Cairns, U. Wissenbach, J. Prenen, V. Flockerzi, G. Droogmans, C. D. Benham, B. Nilius, Activation of TRPV4 channels (hVRL-2/mTRP12) by phorbol derivatives. *J Biol Chem* **277**, 13569-13577 (2002).

55. H. Watanabe, J. Vriens, J. Prenen, G. Droogmans, T. Voets, B. Nilius, Anandamide and arachidonic acid use epoxyeicosatrienoic acids to activate TRPV4 channels. *Nature* **424**, 434-438 (2003).

56. A. Karara, E. Dishman, J. R. Falck, J. H. Capdevila, Endogenous epoxyeicosatrienoyl-phospholipids. A novel class of cellular glycerolipids containing epoxidized arachidonate moieties. *J Biol Chem* **266**, 7561-7569 (1991).

57. J. K. Chen, J. Capdevila, R. C. Harris, Cytochrome p450 epoxygenase metabolism of arachidonic acid inhibits apoptosis. *Mol Cell Biol* **21**, 6322-6331 (2001).

58. S. A. Mendoza, J. Fang, D. D. Gutterman, D. A. Wilcox, A. H. Bubolz, R. Li, M. Suzuki, D. X. Zhang, TRPV4-mediated endothelial Ca2+ influx and vasodilation in response to shear stress. *Am J Physiol Heart Circ Physiol* **298**, H466-476 (2010).

59. V. Hartmannsgruber, W. T. Heyken, M. Kacik, A. Kaistha, I. Grgic, C. Harteneck, W. Liedtke, J. Hoyer, R. Kohler, Arterial response to shear stress critically depends on endothelial TRPV4 expression. *PLoS One* **2**, e827 (2007).

60. A. E. Loot, R. Popp, B. Fisslthaler, J. Vriens, B. Nilius, I. Fleming, Role of cytochrome P450-dependent transient receptor potential V4 activation in flow-induced vasodilatation. *Cardiovasc Res* **80**, 445-452 (2008).

61. R. Strotmann, C. Harteneck, K. Nunnenmacher, G. Schultz, T. D. Plant, OTRPC4, a nonselective cation channel that confers sensitivity to extracellular osmolarity. *Nat Cell Biol* **2**, 695-702 (2000).

62. C. Liu, D. X. Zhang, H. J. Zhang, [Development of photothermal microactuator based on spectral analysis of photothermal expansion material]. *Guang Pu Xue Yu Guang Pu Fen Xi* **29**, 3047-3051 (2009).

63. S. Earley, T. Pauyo, R. Drapp, M. J. Tavares, W. Liedtke, J. E. Brayden, TRPV4-dependent dilation of peripheral resistance arteries influences arterial pressure. *Am J Physiol Heart Circ Physiol* **297**, H1096-1102 (2009).

64. J. Saliez, C. Bouzin, G. Rath, P. Ghisdal, F. Desjardins, R. Rezzani, L. F. Rodella, J. Vriens, B. Nilius, O. Feron, J. L. Balligand, C. Dessy, Role of caveolar compartmentation in endothelium-derived hyperpolarizing factor-mediated relaxation: Ca2+ signals and gap junction function are regulated by caveolin in endothelial cells. *Circulation* **117**, 1065-1074 (2008).

65. G. Gao, X. Y. Bai, C. Xuan, X. C. Liu, W. B. Jing, A. Novakovic, Q. Yang, G. W. He, Role of TRPC3 channel in human internal mammary artery. *Arch Med Res* **43**, 431-437 (2012).

66. M. Y. Kochukov, A. Balasubramanian, R. C. Noel, S. P. Marrelli, Role of TRPC1 and TRPC3 channels in contraction and relaxation of mouse thoracic aorta. *J Vasc Res* **50**, 11-20 (2013).

67. D. M. Bautista, P. Movahed, A. Hinman, H. E. Axelsson, O. Sterner, E. D. Hogestatt, D. Julius, S. E. Jordt, P. M. Zygmunt, Pungent products from garlic activate the sensory ion channel TRPA1. *Proc Natl Acad Sci U S A* **102**, 12248-12252 (2005).

68. A. Demuro, I. Parker, Imaging single-channel calcium microdomains by total internal reflection microscopy. *Biol Res* **37**, 675-679 (2004).

69. A. Demuro, I. Parker, Optical single-channel recording: imaging Ca2+ flux through individual N-type voltage-gated channels expressed in Xenopus oocytes. *Cell Calcium* **34**, 499-509 (2003).

70. A. Minta, J. P. Kao, R. Y. Tsien, Fluorescent indicators for cytosolic calcium based on rhodamine and fluorescein chromophores. *J Biol Chem* **264**, 8171-8178 (1989).

71. K. R. Gee, K. A. Brown, W. N. Chen, J. Bishop-Stewart, D. Gray, I. Johnson, Chemical and physiological characterization of fluo-4 Ca(2+)-indicator dyes. *Cell Calcium* **27**, 97-106 (2000).

72. T. Nagai, A. Sawano, E. S. Park, A. Miyawaki, Circularly permuted green fluorescent proteins engineered to sense Ca2+. *Proc Natl Acad Sci U S A* **98**, 3197-3202 (2001).

73. Y. N. Tallini, M. Ohkura, B. R. Choi, G. Ji, K. Imoto, R. Doran, J. Lee, P. Plan, J. Wilson, H. B. Xin, A. Sanbe, J. Gulick, J. Mathai, J. Robbins, G. Salama, J. Nakai, M. I. Kotlikoff, Imaging cellular signals in the heart in vivo: Cardiac expression of the high-signal Ca2+ indicator GCaMP2. *Proc Natl Acad Sci U S A* **103**, 4753-4758 (2006).

74. Y. N. Tallini, J. F. Brekke, B. Shui, R. Doran, S. M. Hwang, J. Nakai, G. Salama, S. S. Segal, M. I. Kotlikoff, Propagated endothelial Ca2+ waves and arteriolar dilation in vivo: measurements in Cx40BAC GCaMP2 transgenic mice. *Circ Res* **101**, 1300-1309 (2007).

75. A. Miyawaki, J. Llopis, R. Heim, J. M. McCaffery, J. A. Adams, M. Ikura, R. Y. Tsien, Fluorescent indicators for Ca2+ based on green fluorescent proteins and calmodulin. *Nature* **388**, 882-887 (1997).

76. S. Q. Wang, L. S. Song, E. G. Lakatta, H. Cheng, Ca2+ signalling between single L-type Ca2+ channels and ryanodine receptors in heart cells. *Nature* **410**, 592-596 (2001).

77. M. T. Nelson, H. Cheng, M. Rubart, L. F. Santana, A. D. Bonev, H. J. Knot, W. J. Lederer, Relaxation of arterial smooth muscle by calcium sparks. *Science* **270**, 633-637 (1995).

78. M. F. Navedo, G. C. Amberg, V. S. Votaw, L. F. Santana, Constitutively active L-type Ca2+ channels. *Proc Natl Acad Sci U S A* **102**, 11112-11117 (2005).

79. M. F. Navedo, G. C. Amberg, M. Nieves, J. D. Molkentin, L. F. Santana, Mechanisms underlying heterogeneous Ca2+ sparklet activity in arterial smooth muscle. *J Gen Physiol* **127**, 611-622 (2006).

80. M. F. Navedo, Y. Takeda, M. Nieves-Cintron, J. D. Molkentin, L. F. Santana, Elevated Ca2+ sparklet activity during acute hyperglycemia and diabetes in cerebral arterial smooth muscle cells. *Am J Physiol Cell Physiol* **298**, C211-220 (2010).

81. M. F. Navedo, E. P. Cheng, C. Yuan, S. Votaw, J. D. Molkentin, J. D. Scott, L. F. Santana, Increased coupled gating of L-type Ca2+ channels during hypertension and Timothy syndrome. *Circ Res* **106**, 748-756 (2010).

82. M. F. Navedo, M. Nieves-Cintron, G. C. Amberg, C. Yuan, V. S. Votaw, W. J. Lederer, G. S. McKnight, L. F. Santana, AKAP150 is required for stuttering

persistent Ca2+ sparklets and angiotensin II-induced hypertension. *Circ Res* **102**, e1-e11 (2008).

83. J. Zhong, J. R. Hume, K. D. Keef, Anchoring protein is required for cAMP-dependent stimulation of L-type Ca(2+) channels in rabbit portal vein. *Am J Physiol* **277**, C840-844 (1999).

84. M. Francis, X. Qian, C. Charbel, J. Ledoux, J. C. Parker, M. S. Taylor, Automated region of interest analysis of dynamic Ca2+ signals in image sequences. *Am J Physiol Cell Physiol*, (2012).

85. C. O. Wong, X. Yao, TRP channels in vascular endothelial cells. *Adv Exp Med Biol* **704**, 759-780 (2011).

86. C. Zitt, A. Zobel, A. G. Obukhov, C. Harteneck, F. Kalkbrenner, A. Luckhoff, G. Schultz, Cloning and functional expression of a human Ca2+-permeable cation channel activated by calcium store depletion. *Neuron* **16**, 1189-1196 (1996).

87. P. Lucas, K. Ukhanov, T. Leinders-Zufall, F. Zufall, A diacylglycerol-gated cation channel in vomeronasal neuron dendrites is impaired in TRPC2 mutant mice: mechanism of pheromone transduction. *Neuron* **40**, 551-561 (2003).

88. K. Groschner, S. Hingel, B. Lintschinger, M. Balzer, C. Romanin, X. Zhu, W. Schreibmayer, Trp proteins form store-operated cation channels in human vascular endothelial cells. *FEBS Lett* **437**, 101-106 (1998).

89. T. Hofmann, A. G. Obukhov, M. Schaefer, C. Harteneck, T. Gudermann, G. Schultz, Direct activation of human TRPC6 and TRPC3 channels by diacylglycerol. *Nature* **397**, 259-263 (1999).

90. S. Philipp, A. Cavalie, M. Freichel, U. Wissenbach, S. Zimmer, C. Trost, A. Marquart, M. Murakami, V. Flockerzi, A mammalian capacitative calcium entry channel homologous to Drosophila TRP and TRPL. *EMBO J* **15**, 6166-6171 (1996).

91. T. Okada, R. Inoue, K. Yamazaki, A. Maeda, T. Kurosaki, T. Yamakuni, I. Tanaka, S. Shimizu, K. Ikenaka, K. Imoto, Y. Mori, Molecular and functional characterization of a novel mouse transient receptor potential protein homologue TRP7. Ca(2+)-permeable cation channel that is constitutively activated and enhanced by stimulation of G protein-coupled receptor. *J Biol Chem* **274**, 27359-27370 (1999).

92. E. Oancea, J. Vriens, S. Brauchi, J. Jun, I. Splawski, D. E. Clapham, TRPM1 forms ion channels associated with melanin content in melanocytes. *Sci Signal* **2**, ra21 (2009).

93. A. L. Perraud, A. Fleig, C. A. Dunn, L. A. Bagley, P. Launay, C. Schmitz, A. J. Stokes, Q. Zhu, M. J. Bessman, R. Penner, J. P. Kinet, A. M. Scharenberg, ADP-ribose gating of the calcium-permeable LTRPC2 channel revealed by Nudix motif homology. *Nature* **411**, 595-599 (2001).

94. C. Grimm, R. Kraft, S. Sauerbruch, G. Schultz, C. Harteneck, Molecular and functional characterization of the melastatin-related cation channel TRPM3. *J Biol Chem* **278**, 21493-21501 (2003).

95. P. Launay, A. Fleig, A. L. Perraud, A. M. Scharenberg, R. Penner, J. P. Kinet, TRPM4 is a Ca2+-activated nonselective cation channel mediating cell membrane depolarization. *Cell* **109**, 397-407 (2002).

96. T. Hofmann, V. Chubanov, T. Gudermann, C. Montell, TRPM5 is a voltage-modulated and Ca(2+)-activated monovalent selective cation channel. *Curr Biol* **13**, 1153-1158 (2003).

97. T. Voets, B. Nilius, S. Hoefs, A. W. van der Kemp, G. Droogmans, R. J. Bindels, J. G. Hoenderop, TRPM6 forms the Mg2+ influx channel involved in intestinal and renal Mg2+ absorption. *J Biol Chem* **279**, 19-25 (2004).

98. L. W. Runnels, L. Yue, D. E. Clapham, TRP-PLIK, a bifunctional protein with kinase and ion channel activities. *Science* **291**, 1043-1047 (2001).

99. J. M. LaPlante, J. Falardeau, M. Sun, M. Kanazirska, E. M. Brown, S. A. Slaugenhaupt, P. M. Vassilev, Identification and characterization of the single channel function of human mucolipin-1 implicated in mucolipidosis type IV, a disorder affecting the lysosomal pathway. *FEBS Lett* **532**, 183-187 (2002).

100. P. Koulen, Y. Cai, L. Geng, Y. Maeda, S. Nishimura, R. Witzgall, B. E. Ehrlich, S. Somlo, Polycystin-2 is an intracellular calcium release channel. *Nat Cell Biol* **4**, 191-197 (2002).

101. X. Z. Chen, P. M. Vassilev, N. Basora, J. B. Peng, H. Nomura, Y. Segal, E. M. Brown, S. T. Reeders, M. A. Hediger, J. Zhou, Polycystin-L is a calcium-regulated cation channel permeable to calcium ions. *Nature* **401**, 383-386 (1999).

102. T. Volk, A. P. Schwoerer, S. Thiessen, J. H. Schultz, H. Ehmke, A polycystin-2-like large conductance cation channel in rat left ventricular myocytes. *Cardiovasc Res* **58**, 76-88 (2003).

103. M. Kanzaki, M. Nagasawa, I. Kojima, C. Sato, K. Naruse, M. Sokabe, H. Iida, Molecular identification of a eukaryotic, stretch-activated nonselective cation channel. *Science* **285**, 882-886 (1999).

104. H. Xu, I. S. Ramsey, S. A. Kotecha, M. M. Moran, J. A. Chong, D. Lawson, P. Ge, J. Lilly, I. Silos-Santiago, Y. Xie, P. S. DiStefano, R. Curtis, D. E. Clapham, TRPV3 is a calcium-permeable temperature-sensitive cation channel. *Nature* **418**, 181-186 (2002).

105. S. Mergler, M. Valtink, V. J. Coulson-Thomas, D. Lindemann, P. S. Reinach, K. Engelmann, U. Pleyer, TRPV channels mediate temperature-sensing in human corneal endothelial cells. *Exp Eye Res* **90**, 758-770 (2010).

106. R. Strotmann, G. Schultz, T. D. Plant, Ca2+-dependent potentiation of the nonselective cation channel TRPV4 is mediated by a C-terminal calmodulin binding site. *J Biol Chem* **278**, 26541-26549 (2003).

107. L. Yue, J. B. Peng, M. A. Hediger, D. E. Clapham, CaT1 manifests the pore properties of the calcium-release-activated calcium channel. *Nature* **410**, 705-709 (2001).

108. G. J. Perez, A. D. Bonev, J. B. Patlak, M. T. Nelson, Functional coupling of ryanodine receptors to KCa channels in smooth muscle cells from rat cerebral arteries. *J Gen Physiol* **113**, 229-238 (1999).

109. X. P. Sun, N. Callamaras, J. S. Marchant, I. Parker, A continuum of InsP3-mediated elementary Ca2+ signalling events in Xenopus oocytes. *J Physiol* **509 (Pt 1)**, 67-80 (1998).

110. P. M. Vanhoutte, Endothelium-dependent hyperpolarizations: the history. *Pharmacol Res* **49**, 503-508 (2004).

111. A. R. Whorton, C. E. Willis, R. S. Kent, S. L. Young, The role of calcium in the regulation of prostacyclin synthesis by porcine aortic endothelial cells. *Lipids* **19**, 17-24 (1984).

112. R. Kohler, J. Hoyer, The endothelium-derived hyperpolarizing factor: insights from genetic animal models. *Kidney Int* **72**, 145-150 (2007).

113. L. Birnbaumer, X. Zhu, M. Jiang, G. Boulay, M. Peyton, B. Vannier, D. Brown, D. Platano, H. Sadeghi, E. Stefani, M. Birnbaumer, On the molecular basis and regulation of cellular capacitative calcium entry: roles for Trp proteins. *Proc Natl Acad Sci U S A* **93**, 15195-15202 (1996).

114. R. Kohler, W. T. Heyken, P. Heinau, R. Schubert, H. Si, M. Kacik, C. Busch, I. Grgic, T. Maier, J. Hoyer, Evidence for a functional role of endothelial transient receptor potential V4 in shear stress-induced vasodilatation. *Arterioscler Thromb Vasc Biol* **26**, 1495-1502 (2006).

115. S. P. Marrelli, G. O'Neil R, R. C. Brown, R. M. Bryan, Jr., PLA2 and TRPV4 channels regulate endothelial calcium in cerebral arteries. *Am J Physiol Heart Circ Physiol* **292**, H1390-1397 (2007).

116. J. Vriens, G. Owsianik, B. Fisslthaler, M. Suzuki, A. Janssens, T. Voets, C. Morisseau, B. D. Hammock, I. Fleming, R. Busse, B. Nilius, Modulation of the Ca2 permeable cation channel TRPV4 by cytochrome P450 epoxygenases in vascular endothelium. *Circ Res* **97**, 908-915 (2005).

117. A. Demuro, I. Parker, Imaging single-channel calcium microdomains. *Cell Calcium* **40**, 413-422 (2006).

118. I. Parker, I. F. Smith, Recording single-channel activity of inositol trisphosphate receptors in intact cells with a microscope, not a patch clamp. *J Gen Physiol* **136**, 119-127 (2010).

119. H. Cheng, W. J. Lederer, M. B. Cannell, Calcium sparks: elementary events underlying excitation-contraction coupling in heart muscle. *Science* **262**, 740-744 (1993).

120. J. X. Shen, T. Z. Han, H. P. Cheng, [Microscopic mechanism of excitation-contraction coupling in cardiac myocytes]. *Sheng Li Ke Xue Jin Zhan* **35**, 294-298 (2004).

121. S. M. Brierley, A. J. Page, P. A. Hughes, B. Adam, T. Liebregts, N. J. Cooper, G. Holtmann, W. Liedtke, L. A. Blackshaw, Selective role for TRPV4 ion channels in visceral sensory pathways. *Gastroenterology* **134**, 2059-2069 (2008).

122. X. R. Yang, M. J. Lin, L. S. McIntosh, J. S. Sham, Functional expression of transient receptor potential melastatin- and vanilloid-related channels in pulmonary arterial and aortic smooth muscle. *Am J Physiol Lung Cell Mol Physiol* **290**, L1267-1276 (2006).

123. W. Everaerts, X. Zhen, D. Ghosh, J. Vriens, T. Gevaert, J. P. Gilbert, N. J. Hayward, C. R. McNamara, F. Xue, M. M. Moran, T. Strassmaier, E. Uykal, G. Owsianik, R. Vennekens, D. De Ridder, B. Nilius, C. M. Fanger, T. Voets, Inhibition of the cation channel TRPV4 improves bladder function in mice and

rats with cyclophosphamide-induced cystitis. *Proc Natl Acad Sci U S A* **107**, 19084-19089 (2010).

124. K. S. Thorneloe, A. C. Sulpizio, Z. Lin, D. J. Figueroa, A. K. Clouse, G. P. McCafferty, T. P. Chendrimada, E. S. Lashinger, E. Gordon, L. Evans, B. A. Misajet, D. J. Demarini, J. H. Nation, L. N. Casillas, R. W. Marquis, B. J. Votta, S. A. Sheardown, X. Xu, D. P. Brooks, N. J. Laping, T. D. Westfall, N-((1S)-1-{[4-((2S)-2-{[(2,4-dichlorophenyl)sulfonyl]amino}-3-hydroxypropa noyl)-1-piperazinyl]carbonyl}-3-methylbutyl)-1-benzothiophene-2-carboxamid e (GSK1016790A), a novel and potent transient receptor potential vanilloid 4 channel agonist induces urinary bladder contraction and hyperactivity: Part I. *J Pharmacol Exp Ther* **326**, 432-442 (2008).

125. S. Earley, A. Pastuszyn, B. R. Walker, Cytochrome p-450 epoxygenase products contribute to attenuated vasoconstriction after chronic hypoxia. *Am J Physiol Heart Circ Physiol* **285**, H127-136 (2003).

126. A. Demuro, I. Parker, Optical single-channel recording: imaging Ca2+ flux through individual ion channels with high temporal and spatial resolution. *J Biomed Opt* **10**, 11002 (2005).

127. P. C. Colombo, A. W. Ashton, S. Celaj, A. Talreja, J. E. Banchs, N. B. Dubois, M. Marinaccio, S. Malla, J. Lachmann, J. A. Ware, T. H. Le Jemtel, Biopsy coupled to quantitative immunofluorescence: a new method to study the human vascular endothelium. *J Appl Physiol* **92**, 1331-1338 (2002).

128. M. Jin, Z. Wu, L. Chen, J. Jaimes, D. Collins, E. T. Walters, R. G. O'Neil, Determinants of TRPV4 activity following selective activation by small molecule agonist GSK1016790A. *PLoS One* **6**, e16713 (2011).

129. X. Xu, E. Gordon, Z. Lin, I. M. Lozinskaya, Y. Chen, K. S. Thorneloe, Functional TRPV4 channels and an absence of capsaicin-evoked currents in freshly-isolated, guinea-pig urothelial cells. *Channels (Austin)* **3**, 156-160 (2009).

130. S. A. Gradilone, T. V. Masyuk, B. Q. Huang, J. M. Banales, G. L. Lehmann, B. N. Radtke, A. Stroope, A. I. Masyuk, P. L. Splinter, N. F. LaRusso, Activation of Trpv4 reduces the hyperproliferative phenotype of cystic cholangiocytes from an animal model of ARPKD. *Gastroenterology* **139**, 304-314 e302 (2010).

131. H. Mihara, A. Boudaka, T. Sugiyama, Y. Moriyama, M. Tominaga, Transient receptor potential vanilloid 4 (TRPV4)-dependent calcium influx and ATP release in mouse oesophageal keratinocytes. *J Physiol* **589**, 3471-3482 (2011).

132. D. A. Ryskamp, P. Witkovsky, P. Barabas, W. Huang, C. Koehler, N. P. Akimov, S. H. Lee, S. Chauhan, W. Xing, R. C. Renteria, W. Liedtke, D. Krizaj, The polymodal ion channel transient receptor potential vanilloid 4 modulates calcium flux, spiking rate, and apoptosis of mouse retinal ganglion cells. *J Neurosci* **31**, 7089-7101 (2011).

133. L. M. Duncan, J. Deeds, J. Hunter, J. Shao, L. M. Holmgren, E. A. Woolf, R. I. Tepper, A. W. Shyjan, Down-regulation of the novel gene melastatin correlates with potential for melanoma metastasis. *Cancer Res* **58**, 1515-1520 (1998).

134. D. H. Grimm, A. Karihaloo, Y. Cai, S. Somlo, L. G. Cantley, M. J. Caplan, Polycystin-2 regulates proliferation and branching morphogenesis in kidney epithelial cells. *J Biol Chem* **281**, 137-144 (2006).

135. C. L. Huang, The transient receptor potential superfamily of ion channels. *J Am Soc Nephrol* **15**, 1690-1699 (2004).

136. L. A. Pardo, Voltage-gated potassium channels in cell proliferation. *Physiology (Bethesda)* **19**, 285-292 (2004).

137. K. P. Schlingmann, S. Weber, M. Peters, L. Niemann Nejsum, H. Vitzthum, K. Klingel, M. Kratz, E. Haddad, E. Ristoff, D. Dinour, M. Syrrou, S. Nielsen, M. Sassen, S. Waldegger, H. W. Seyberth, M. Konrad, Hypomagnesemia with secondary hypocalcemia is caused by mutations in TRPM6, a new member of the TRPM gene family. *Nat Genet* **31**, 166-170 (2002).

138. N. Zhong, V. Beaumont, R. S. Zucker, Calcium influx through HCN channels does not contribute to cAMP-enhanced transmission. *J Neurophysiol* **92**, 644-647 (2004).

139. T. M. Paravicini, C. G. Sobey, Cerebral vascular effects of reactive oxygen species: recent evidence for a role of NADPH-oxidase. *Clin Exp Pharmacol Physiol* **30**, 855-859 (2003).

140. B. M. Babior, R. S. Kipnes, J. T. Curnutte, Biological defense mechanisms. The production by leukocytes of superoxide, a potential bactericidal agent. *J Clin Invest* **52**, 741-744 (1973).

141. A. A. Miller, G. R. Drummond, C. G. Sobey, Reactive oxygen species in the cerebral circulation: are they all bad? *Antioxid Redox Signal* **8**, 1113-1120 (2006).

142. A. A. Miller, G. R. Drummond, H. H. Schmidt, C. G. Sobey, NADPH oxidase activity and function are profoundly greater in cerebral versus systemic arteries. *Circ Res* **97**, 1055-1062 (2005).

143. N. Weissmann, A. Sydykov, H. Kalwa, U. Storch, B. Fuchs, M. Mederos y Schnitzler, R. P. Brandes, F. Grimminger, M. Meissner, M. Freichel, S. Offermanns, F. Veit, O. Pak, K. H. Krause, R. T. Schermuly, A. C. Brewer, H. H. Schmidt, W. Seeger, A. M. Shah, T. Gudermann, H. A. Ghofrani, A. Dietrich, Activation of TRPC6 channels is essential for lung ischaemia-reperfusion induced oedema in mice. *Nature communications* **3**, 649 (2012).

144. L. Zhang, P. Papadopoulos, E. Hamel, Endothelial TRPV4 channels mediate dilation of cerebral arteries: impairment and recovery in cerebrovascular pathologies related to Alzheimer's disease. *Br J Pharmacol* **170**, 661-670 (2013).

145. D. A. Andersson, C. Gentry, S. Moss, S. Bevan, Transient receptor potential A1 is a sensory receptor for multiple products of oxidative stress. *J Neurosci* **28**, 2485-2494 (2008).

146. N. Takahashi, D. Kozai, R. Kobayashi, M. Ebert, Y. Mori, Roles of TRPM2 in oxidative stress. *Cell Calcium* **50**, 279-287 (2011).

147. Y. Sawada, H. Hosokawa, K. Matsumura, S. Kobayashi, Activation of transient receptor potential ankyrin 1 by hydrogen peroxide. *Eur J Neurosci* **27**, 1131-1142 (2008).

148. K. Uchida, 4-Hydroxy-2-nonenal: a product and mediator of oxidative stress. *Prog Lipid Res* **42**, 318-343 (2003).

149. J. M. Gutteridge, R. Richmond, B. Halliwell, Inhibition of the iron-catalysed formation of hydroxyl radicals from superoxide and of lipid peroxidation by desferrioxamine. *Biochem J* **184**, 469-472 (1979).

150. S. Fredriksson, M. Gullberg, J. Jarvius, C. Olsson, K. Pietras, S. M. Gustafsdottir, A. Ostman, U. Landegren, Protein detection using proximity-dependent DNA ligation assays. *Nat Biotechnol* **20**, 473-477 (2002).

151. A. L. Gonzales, Y. Yang, M. N. Sullivan, L. Sanders, F. Dabertrand, D. C. Hill-Eubanks, M. T. Nelson, S. Earley, A PLCgamma1-dependent, force-sensitive signaling network in the myogenic constriction of cerebral arteries. *Sci Signal* **7**, ra49 (2014).

152. D. Mukherjea, S. Jajoo, K. Sheehan, T. Kaur, S. Sheth, J. Bunch, C. Perro, L. P. Rybak, V. Ramkumar, NOX3 NADPH oxidase couples transient receptor potential vanilloid 1 to signal transducer and activator of transcription 1-mediated inflammation and hearing loss. *Antioxid Redox Signal* **14**, 999-1010 (2011).

153. A. Gorlach, R. P. Brandes, K. Nguyen, M. Amidi, F. Dehghani, R. Busse, A gp91phox containing NADPH oxidase selectively expressed in endothelial cells is a major source of oxygen radical generation in the arterial wall. *Circ Res* **87**, 26-32 (2000).

154. T. Ago, T. Kitazono, J. Kuroda, Y. Kumai, M. Kamouchi, H. Ooboshi, M. Wakisaka, T. Kawahara, K. Rokutan, S. Ibayashi, M. Iida, NAD(P)H oxidases in rat basilar arterial endothelial cells. *Stroke* **36**, 1040-1046 (2005).

155. C. R. McNamara, J. Mandel-Brehm, D. M. Bautista, J. Siemens, K. L. Deranian, M. Zhao, N. J. Hayward, J. A. Chong, D. Julius, M. M. Moran, C. M. Fanger, TRPA1 mediates formalin-induced pain. *Proc Natl Acad Sci U S A* **104**, 13525-13530 (2007).

156. S. P. Didion, F. M. Faraci, Effects of NADH and NADPH on superoxide levels and cerebral vascular tone. *Am J Physiol Heart Circ Physiol* **282**, H688-695 (2002).

157. R. M. Hannah, K. M. Dunn, A. D. Bonev, M. T. Nelson, Endothelial SK(Ca) and IK(Ca) channels regulate brain parenchymal arteriolar diameter and cortical cerebral blood flow. *J Cereb Blood Flow Metab* **31**, 1175-1186 (2011).

158. F. E. Rey, M. E. Cifuentes, A. Kiarash, M. T. Quinn, P. J. Pagano, Novel competitive inhibitor of NAD(P)H oxidase assembly attenuates vascular O(2)(-) and systolic blood pressure in mice. *Circ Res* **89**, 408-414 (2001).

159. K. Uchida, L. I. Szweda, H. Z. Chae, E. R. Stadtman, Immunochemical detection of 4-hydroxynonenal protein adducts in oxidized hepatocytes. *Proc Natl Acad Sci U S A* **90**, 8742-8746 (1993).

160. K. Nagata, A. Duggan, G. Kumar, J. Garcia-Anoveros, Nociceptor and hair cell transducer properties of TRPA1, a channel for pain and hearing. *J Neurosci* **25**, 4052-4061 (2005).

161. H. Watanabe, J. Vriens, S. H. Suh, C. D. Benham, G. Droogmans, B. Nilius, Heat-evoked activation of TRPV4 channels in a HEK293 cell expression system and in native mouse aorta endothelial cells. *J Biol Chem* **277**, 47044-47051 (2002).

162. J. Mercado, R. Baylie, M. F. Navedo, C. Yuan, J. D. Scott, M. T. Nelson, J. E. Brayden, L. F. Santana, Local control of TRPV4 channels by AKAP150-targeted PKC in arterial smooth muscle. *J Gen Physiol* **143**, 559-575 (2014).

163. H. A. Coleman, M. Tare, H. C. Parkington, K+ currents underlying the action of endothelium-derived hyperpolarizing factor in guinea-pig, rat and human blood vessels. *J Physiol* **531**, 359-373 (2001).

164. R. M. Touyz, A. M. Briones, Reactive oxygen species and vascular biology: implications in human hypertension. *Hypertens Res* **34**, 5-14 (2011).

165. K. Bedard, K. H. Krause, The NOX family of ROS-generating NADPH oxidases: physiology and pathophysiology. *Physiol Rev* **87**, 245-313 (2007).

166. T. M. Paravicini, S. Chrissobolis, G. R. Drummond, C. G. Sobey, Increased NADPH-oxidase activity and Nox4 expression during chronic hypertension is associated with enhanced cerebral vasodilatation to NADPH in vivo. *Stroke* **35**, 584-589 (2004).

167. D. Mukherjee, C. G. Patil, Epidemiology and the global burden of stroke. *World Neurosurg* **76**, S85-90 (2011).

168. A. S. Go, D. Mozaffarian, V. L. Roger, E. J. Benjamin, J. D. Berry, W. B. Borden, D. M. Bravata, S. Dai, E. S. Ford, C. S. Fox, S. Franco, H. J. Fullerton, C. Gillespie, S. M. Hailpern, J. A. Heit, V. J. Howard, M. D. Huffman, B. M. Kissela, S. J. Kittner, D. T. Lackland, J. H. Lichtman, L. D. Lisabeth, D. Magid, G. M. Marcus, A. Marelli, D. B. Matchar, D. K. McGuire, E. R. Mohler, C. S. Moy, M. E. Mussolino, G. Nichol, N. P. Paynter, P. J. Schreiner, P. D. Sorlie, J. Stein, T. N. Turan, S. S. Virani, N. D. Wong, D. Woo, M. B. Turner, Heart disease and stroke

statistics--2013 update: a report from the American Heart Association. *Circulation* **127**, e6-e245 (2013).

169. W. Li, H. Peng, E. P. Mehaffey, C. D. Kimball, J. L. Grobe, J. M. van Gool, M. N. Sullivan, S. Earley, A. H. Danser, A. Ichihara, Y. Feng, Neuron-specific (pro)renin receptor knockout prevents the development of salt-sensitive hypertension. *Hypertension* **63**, 316-323 (2014).

170. Y. Feng, H. Xia, Y. Cai, C. M. Halabi, L. K. Becker, R. A. Santos, R. C. Speth, C. D. Sigmund, E. Lazartigues, Brain-selective overexpression of human Angiotensin-converting enzyme type 2 attenuates neurogenic hypertension. *Circ Res* **106**, 373-382 (2010).

171. M. W. Pfaffl, A new mathematical model for relative quantification in real-time RT-PCR. *Nucleic Acids Res* **29**, e45 (2001).

172. R. Crnich, G. C. Amberg, M. D. Leo, A. L. Gonzales, M. M. Tamkun, J. H. Jaggar, S. Earley, Vasoconstriction resulting from dynamic membrane trafficking of TRPM4 in vascular smooth muscle cells. *Am J Physiol Cell Physiol* **299**, C682-694 (2010).

173. Y. Wakisaka, Y. Chu, J. D. Miller, G. A. Rosenberg, D. D. Heistad, Spontaneous intracerebral hemorrhage during acute and chronic hypertension in mice. *J Cereb Blood Flow Metab* **30**, 56-69 (2010).

174. S. Iida, G. L. Baumbach, J. L. Lavoie, F. M. Faraci, C. D. Sigmund, D. D. Heistad, Spontaneous stroke in a genetic model of hypertension in mice. *Stroke* **36**, 1253-1258 (2005).

175. R. M. Touyz, A. M. Briones, M. Sedeek, D. Burger, A. C. Montezano, NOX isoforms and reactive oxygen species in vascular health. *Mol Interv* **11**, 27-35 (2011).

176. W. Auch-Schwelk, Z. S. Katusic, P. M. Vanhoutte, Contractions to oxygen-derived free radicals are augmented in aorta of the spontaneously hypertensive rat. *Hypertension* **13**, 859-864 (1989).

177. S. Rajagopalan, S. Kurz, T. Munzel, M. Tarpey, B. A. Freeman, K. K. Griendling, D. G. Harrison, Angiotensin II-mediated hypertension in the rat increases vascular superoxide production via membrane NADH/NADPH oxidase activation. Contribution to alterations of vasomotor tone. *J Clin Invest* **97**, 1916-1923 (1996).

178. A. M. Hurne, C. L. Chai, K. Moerman, P. Waring, Influx of calcium through a redox-sensitive plasma membrane channel in thymocytes causes early necrotic cell death induced by the epipolythiodioxopiperazine toxins. *J Biol Chem* **277**, 31631-31638 (2002).

179. T. Yoshida, R. Inoue, T. Morii, N. Takahashi, S. Yamamoto, Y. Hara, M. Tominaga, S. Shimizu, Y. Sato, Y. Mori, Nitric oxide activates TRP channels by cysteine S-nitrosylation. *Nature chemical biology* **2**, 596-607 (2006).

180. J. Scharf, E. Brauherr, M. Forsting, K. Sartor, Significance of haemorrhagic lacunes on MRI in patients with hypertensive cerebrovascular disease and intracerebral haemorrhage. *Neuroradiology* **36**, 504-508 (1994).

181. H. Chen, Y. S. Song, P. H. Chan, Inhibition of NADPH oxidase is neuroprotective after ischemia-reperfusion. *J Cereb Blood Flow Metab* **29**, 1262-1272 (2009).

182. X. N. Tang, B. Cairns, N. Cairns, M. A. Yenari, Apocynin improves outcome in experimental stroke with a narrow dose range. *Neuroscience* **154**, 556-562 (2008).

183. T. A. Marsen, M. S. Simonson, M. J. Dunn, Roles of calcium and kinases in regulation of thrombin-stimulated preproendothelin-1 transcription. *Am J Physiol* **271**, H1918-1925 (1996).

184. M. K. Chung, H. Lee, A. Mizuno, M. Suzuki, M. J. Caterina, 2-aminoethoxydiphenyl borate activates and sensitizes the heat-gated ion channel TRPV3. *J Neurosci* **24**, 5177-5182 (2004).

185. A. P. Thomas, G. S. Bird, G. Hajnoczky, L. D. Robb-Gaspers, J. W. Putney, Jr., Spatial and temporal aspects of cellular calcium signaling. *FASEB J* **10**, 1505-1517 (1996).

186. K. D. Wu, W. S. Lee, J. Wey, D. Bungard, J. Lytton, Localization and quantification of endoplasmic reticulum Ca(2+)-ATPase isoform transcripts. *Am J Physiol* **269**, C775-784 (1995).

187. E. Carafoli, Biogenesis: plasma membrane calcium ATPase: 15 years of work on the purified enzyme. *FASEB J* **8**, 993-1002 (1994).

188. L. Zhao, M. N. Sullivan, M. Chase, A. L. Gonzales, S. Earley, Calcineurin/nuclear factor of activated T cells-coupled vanilliod transient receptor potential channel 4 ca2+ sparklets stimulate airway smooth muscle cell proliferation. *Am J Respir Cell Mol Biol* **50**, 1064-1075 (2014).

189. A. A. Quyyumi, Prognostic value of endothelial function. *Am J Cardiol* **91**, 19H-24H (2003).

190. D. Prawitt, M. K. Monteilh-Zoller, L. Brixel, C. Spangenberg, B. Zabel, A. Fleig, R. Penner, TRPM5 is a transient Ca2+-activated cation channel responding to rapid changes in [Ca2+]i. *Proc Natl Acad Sci U S A* **100**, 15166-15171 (2003).

191. A. Hinman, H. H. Chuang, D. M. Bautista, D. Julius, TRP channel activation by reversible covalent modification. *Proc Natl Acad Sci U S A* **103**, 19564-19568 (2006).

192. L. J. Macpherson, A. E. Dubin, M. J. Evans, F. Marr, P. G. Schultz, B. F. Cravatt, A. Patapoutian, Noxious compounds activate TRPA1 ion channels through covalent modification of cysteines. *Nature* **445**, 541-545 (2007).

193. L. J. Macpherson, B. Xiao, K. Y. Kwan, M. J. Petrus, A. E. Dubin, S. Hwang, B. Cravatt, D. P. Corey, A. Patapoutian, An ion channel essential for sensing chemical damage. *J Neurosci* **27**, 11412-11415 (2007).

194. M. Trevisani, J. Siemens, S. Materazzi, D. M. Bautista, R. Nassini, B. Campi, N. Imamachi, E. Andre, R. Patacchini, G. S. Cottrell, R. Gatti, A. I. Basbaum, N. W. Bunnett, D. Julius, P. Geppetti, 4-Hydroxynonenal, an endogenous aldehyde, causes pain and neurogenic inflammation through activation of the irritant receptor TRPA1. *Proc Natl Acad Sci U S A* **104**, 13519-13524 (2007).

195. K. Kazama, J. Anrather, P. Zhou, H. Girouard, K. Frys, T. A. Milner, C. Iadecola, Angiotensin II impairs neurovascular coupling in neocortex through NADPH oxidase-derived radicals. *Circ Res* **95**, 1019-1026 (2004).

196. K. K. Griendling, D. Sorescu, M. Ushio-Fukai, NAD(P)H oxidase: role in cardiovascular biology and disease. *Circ Res* **86**, 494-501 (2000).

197. S. P. Didion, M. J. Ryan, G. L. Baumbach, C. D. Sigmund, F. M. Faraci, Superoxide contributes to vascular dysfunction in mice that express human renin and angiotensinogen. *Am J Physiol Heart Circ Physiol* **283**, H1569-1576 (2002).

198. L. Park, J. Anrather, P. Zhou, K. Frys, G. Wang, C. Iadecola, Exogenous NADPH increases cerebral blood flow through NADPH oxidase-dependent and -independent mechanisms. *Arterioscler Thromb Vasc Biol* **24**, 1860-1865 (2004).

199. D. M. Lloyd-Jones, Cardiovascular risk prediction: basic concepts, current status, and future directions. *Circulation* **121**, 1768-1777 (2010).

200. K. Dharmashankar, M. E. Widlansky, Vascular endothelial function and hypertension: insights and directions. *Curr Hypertens Rep* **12**, 448-455 (2010).

201. D. R. Harder, J. Smeda, J. Lombard, Enhanced myogenic depolarization in hypertensive cerebral arterial muscle. *Circ Res* **57**, 319-322 (1985).

202. P. F. Pratt, S. Bonnet, L. M. Ludwig, P. Bonnet, N. J. Rusch, Upregulation of L-type Ca2+ channels in mesenteric and skeletal arteries of SHR. *Hypertension* **40**, 214-219 (2002).

203. G. C. Amberg, A. D. Bonev, C. F. Rossow, M. T. Nelson, L. F. Santana, Modulation of the molecular composition of large conductance, Ca(2+) activated K(+) channels in vascular smooth muscle during hypertension. *J Clin Invest* **112**, 717-724 (2003).

204. J. P. Bannister, S. Bulley, D. Narayanan, C. Thomas-Gatewood, P. Luzny, J. Pachuau, J. H. Jaggar, Transcriptional upregulation of alpha2delta-1 elevates arterial smooth muscle cell voltage-dependent Ca2+ channel surface expression

and cerebrovascular constriction in genetic hypertension. *Hypertension* **60**, 1006-1015 (2012).

205. A. J. Palmer, C. J. Bulpitt, A. E. Fletcher, D. G. Beevers, E. C. Coles, J. G. Ledingham, P. W. O'Riordan, J. C. Petrie, B. E. Rajagopalan, J. Webster, et al., Relation between blood pressure and stroke mortality. *Hypertension* **20**, 601-605 (1992).

206. R. M. Touyz, Reactive oxygen species, vascular oxidative stress, and redox signaling in hypertension: what is the clinical significance? *Hypertension* **44**, 248-252 (2004).

207. U. Forstermann, Oxidative stress in vascular disease: causes, defense mechanisms and potential therapies. *Nat Clin Pract Cardiovasc Med* **5**, 338-349 (2008).

208. H. Sies, E. Cadenas, Oxidative stress: damage to intact cells and organs. *Philos Trans R Soc Lond B Biol Sci* **311**, 617-631 (1985).

209. B. Lassegue, K. K. Griendling, Reactive oxygen species in hypertension; An update. *Am J Hypertens* **17**, 852-860 (2004).

210. S. P. Didion, D. A. Kinzenbaw, F. M. Faraci, Critical role for CuZn-superoxide dismutase in preventing angiotensin II-induced endothelial dysfunction. *Hypertension* **46**, 1147-1153 (2005).

211. H. Girouard, L. Park, J. Anrather, P. Zhou, C. Iadecola, Angiotensin II attenuates endothelium-dependent responses in the cerebral microcirculation through nox-2-derived radicals. *Arterioscler Thromb Vasc Biol* **26**, 826-832 (2006).

212. M. McIntyre, D. F. Bohr, A. F. Dominiczak, Endothelial function in hypertension: the role of superoxide anion. *Hypertension* **34**, 539-545 (1999).

213. F. Cosentino, J. C. Sill, Z. S. Katusic, Role of superoxide anions in the mediation of endothelium-dependent contractions. *Hypertension* **23**, 229-235 (1994).

214. H. Di Wang, S. Hope, Y. Du, M. T. Quinn, A. Cayatte, P. J. Pagano, R. A. Cohen, Paracrine role of adventitial superoxide anion in mediating spontaneous tone of the isolated rat aorta in angiotensin II-induced hypertension. *Hypertension* **33**, 1225-1232 (1999).

215. H. P. Souza, F. R. Laurindo, R. C. Ziegelstein, C. O. Berlowitz, J. L. Zweier, Vascular NAD(P)H oxidase is distinct from the phagocytic enzyme and modulates vascular reactivity control. *Am J Physiol Heart Circ Physiol* **280**, H658-667 (2001).

216. A. Fortuno, G. San Jose, M. U. Moreno, J. Diez, G. Zalba, Oxidative stress and vascular remodelling. *Exp Physiol* **90**, 457-462 (2005).

217. P. F. Li, R. Dietz, R. von Harsdorf, Differential effect of hydrogen peroxide and superoxide anion on apoptosis and proliferation of vascular smooth muscle cells. *Circulation* **96**, 3602-3609 (1997).

218. A. M. Zafari, M. Ushio-Fukai, M. Akers, Q. Yin, A. Shah, D. G. Harrison, W. R. Taylor, K. K. Griendling, Role of NADH/NADPH oxidase-derived H2O2 in angiotensin II-induced vascular hypertrophy. *Hypertension* **32**, 488-495 (1998).

219. J. R. Peterson, R. V. Sharma, R. L. Davisson, Reactive oxygen species in the neuropathogenesis of hypertension. *Curr Hypertens Rep* **8**, 232-241 (2006).

220. S. Adler, H. Huang, Oxidant stress in kidneys of spontaneously hypertensive rats involves both oxidase overexpression and loss of extracellular superoxide dismutase. *Am J Physiol Renal Physiol* **287**, F907-913 (2004).

221. S. Ulker, P. P. McKeown, U. Bayraktutan, Vitamins reverse endothelial dysfunction through regulation of eNOS and NAD(P)H oxidase activities. *Hypertension* **41**, 534-539 (2003).

222. K. Matsuno, H. Yamada, K. Iwata, D. Jin, M. Katsuyama, M. Matsuki, S. Takai, K. Yamanishi, M. Miyazaki, H. Matsubara, C. Yabe-Nishimura, Nox1 is involved in angiotensin II-mediated hypertension: a study in Nox1-deficient mice. *Circulation* **112**, 2677-2685 (2005).

223. U. Landmesser, S. Dikalov, S. R. Price, L. McCann, T. Fukai, S. M. Holland, W. E. Mitch, D. G. Harrison, Oxidation of tetrahydrobiopterin leads to uncoupling of endothelial cell nitric oxide synthase in hypertension. *J Clin Invest* **111**, 1201-1209 (2003).

224. G. Zalba, G. San Jose, M. U. Moreno, M. A. Fortuno, A. Fortuno, F. J. Beaumont, J. Diez, Oxidative stress in arterial hypertension: role of NAD(P)H oxidase. *Hypertension* **38**, 1395-1399 (2001).

225. J. Redon, M. R. Oliva, C. Tormos, V. Giner, J. Chaves, A. Iradi, G. T. Saez, Antioxidant activities and oxidative stress byproducts in human hypertension. *Hypertension* **41**, 1096-1101 (2003).

226. B. Folkow, M. Hallback, Y. Lundgren, R. Sivertsson, L. Weiss, Importance of adaptive changes in vascular design for establishment of primary hypertension,

studied in man and in spontaneously hypertensive rats. *Circ Res* **32**, Suppl 1:2-16 (1973).

227. W. M. Bayliss, On the local reactions of the arterial wall to changes of internal pressure. *J Physiol* **28**, 220-231 (1902).

228. M. J. Mulvany, C. Aalkjaer, J. Christensen, Changes in noradrenaline sensitivity and morphology of arterial resistance vessels during development of high blood pressure in spontaneously hypertensive rats. *Hypertension* **2**, 664-671 (1980).

229. K. Hayashi, T. Naiki, Adaptation and remodeling of vascular wall; biomechanical response to hypertension. *J Mech Behav Biomed Mater* **2**, 3-19 (2009).

230. C. De Ciuceis, E. Porteri, D. Rizzoni, N. Rizzardi, S. Paiardi, G. E. Boari, M. Miclini, F. Zani, M. L. Muiesan, F. Donato, M. Salvetti, M. Castellano, G. A. Tiberio, S. M. Giulini, E. Agabiti Rosei, Structural alterations of subcutaneous small-resistance arteries may predict major cardiovascular events in patients with hypertension. *Am J Hypertens* **20**, 846-852 (2007).

231. A. S. Izzard, D. Rizzoni, E. Agabiti-Rosei, A. M. Heagerty, Small artery structure and hypertension: adaptive changes and target organ damage. *J Hypertens* **23**, 247-250 (2005).

232. H. Cai, D. G. Harrison, Endothelial dysfunction in cardiovascular diseases: the role of oxidant stress. *Circ Res* **87**, 840-844 (2000).

233. T. J. Guzik, N. E. West, E. Black, D. McDonald, C. Ratnatunga, R. Pillai, K. M. Channon, Functional effect of the C242T polymorphism in the NAD(P)H oxidase p22phox gene on vascular superoxide production in atherosclerosis. *Circulation* **102**, 1744-1747 (2000).

234. D. Ito, M. Murata, K. Watanabe, T. Yoshida, I. Saito, N. Tanahashi, Y. Fukuuchi, C242T polymorphism of NADPH oxidase p22 PHOX gene and ischemic cerebrovascular disease in the Japanese population. *Stroke* **31**, 936-939 (2000).

235. L. Pantoni, Cerebral small vessel disease: from pathogenesis and clinical characteristics to therapeutic challenges. *Lancet Neurol* **9**, 689-701 (2010).

236. W. H. Xu, Large artery: an important target for cerebral small vessel diseases. *Ann Transl Med* **2**, 78 (2014).

237. A. Joutel, M. Monet-Lepretre, C. Gosele, C. Baron-Menguy, A. Hammes, S. Schmidt, B. Lemaire-Carrette, V. Domenga, A. Schedl, P. Lacombe, N. Hubner, Cerebrovascular dysfunction and microcirculation rarefaction precede white matter lesions in a mouse genetic model of cerebral ischemic small vessel disease. *J Clin Invest* **120**, 433-445 (2010).

238. J. C. de la Torre, Cardiovascular risk factors promote brain hypoperfusion leading to cognitive decline and dementia. *Cardiovasc Psychiatry Neurol* **2012**, 367516 (2012).

239. M. W. Vernooij, A. van der Lugt, M. A. Ikram, P. A. Wielopolski, W. J. Niessen, A. Hofman, G. P. Krestin, M. M. Breteler, Prevalence and risk factors of cerebral microbleeds: the Rotterdam Scan Study. *Neurology* **70**, 1208-1214 (2008).

240. M. Kim, H. J. Bae, J. Lee, L. Kang, S. Lee, S. Kim, J. E. Lee, K. M. Lee, B. W. Yoon, O. Kwon, J. S. Koo, B. K. Kim, APOE epsilon2/epsilon4 polymorphism and cerebral microbleeds on gradient-echo MRI. *Neurology* **65**, 1474-1475 (2005).

241. P. Kakar, A. Charidimou, D. J. Werring, Cerebral microbleeds: a new dilemma in stroke medicine. *JRSM Cardiovasc Dis* **1**, 2048004012474754 (2012).

242. F. Fazekas, R. Kleinert, G. Roob, G. Kleinert, P. Kapeller, R. Schmidt, H. P. Hartung, Histopathologic analysis of foci of signal loss on gradient-echo T2*-weighted MR images in patients with spontaneous intracerebral hemorrhage: evidence of microangiopathy-related microbleeds. *AJNR Am J Neuroradiol* **20**, 637-642 (1999).

243. D. M. Bautista, S. E. Jordt, T. Nikai, P. R. Tsuruda, A. J. Read, J. Poblete, E. N. Yamoah, A. I. Basbaum, D. Julius, TRPA1 mediates the inflammatory actions of environmental irritants and proalgesic agents. *Cell* **124**, 1269-1282 (2006).